Characterization of Bone-Conduction Mechanisms in Chinchilla Using in Vivo Measurements and Impedance Models

Characterization of bone-conduction mechanisms in chinchilla using in vivo measurements and impedance models

A dissertation presented

by

Peter N. Bowers

to

The Division of Medical Sciences

in partial fulfillment of the requirements

for the degree of

Doctor of Philosophy

in the subject of

Speech and Hearing Bioscience and Technology

Harvard University

Cambridge, Massachusetts

October 2019

Dissertation Advisor: John J. Rosowski Peter N. Bowers

Characterization of bone-conduction mechanisms in chinchilla using in vivo measurements and impedance models

Abstract

The mechanisms of bone-conduction hearing in chinchilla that result from vibration of the skull, include ear-canal compression, relative motion between the middle-ear bones and the inner ear, compression of the cochlear bone, and the transmission of intracranial sound pressures into the inner ear via fluid-filled connecting pathways. This work aims to characterize these mechanisms in terms of the magnitude and phase of vibration-driven sound pressure and volume-velocity sources within the auditory periphery. A lumped-element circuit model of air-conduction hearing in chinchilla is developed, which serves as the basis for our bone-conduction model. The air-conduction model is adapted from a model of hearing in humans, developed by Zwislocki (Zwislocki, 1962). The chinchilla model is extended by the addition of an ear canal that both contains multiple external-ear bone-conduction sources, and imposes natural impedances on motions of the TM produced by vibration-driven sources within the external, middle and inner ear. The model is further modified by the addition of realistic cochlear scalae, a helicotrema and vestibular and cochlear aqueducts, all of which are defined by the analysis of micro-CT scans of a chinchilla ear. The multiple vibration-driven bone-conduction sources are characterized by measurements of vibration-induced mechanical, acoustic, and/or neurological responses, in normal- or manipulated-ear conditions. The measurements under the various conditions enable separation of system responses resulting from individual sources. Two

external-ear bone-conduction sources, which define the contribution of the bony and cartilaginous walls of the ear canal to vibration-driven sound pressures within the canal, are fully characterized. These sources are shown to dominate the vibration-induced sound pressures within the ear canal. The effect of vibration-driven intracranial sound pressures transmitted to the inner ear via the vestibular and cochlear aqueducts is estimated from measurements and the model. Our analyses suggest this mechanism does not play a significant role in vibration-induced hearing mechanics. A method for differentiating the contributions of cochlear compression and cochlear-fluid inertia to bone-conduction hearing is offered, and an application of this method is demonstrated using a proposed cochlear network that includes such mechanisms.

Table of Contents

Acknowledgments

This work would not be possible without a seemingly endless list of people who have supported me during my graduate studies, and before. First, I would like to acknowledge my family. The person I am today, at least in all the good ways, is due to their support and the example they set. Thank you mom, dad, and my best friend and brother, Phil.

I would like to thank Christie, who had been by my side for the whole of graduate school. Your love and support is tremendous and I feel, at times, undeserving of it. And a big thank you to her family, who treated me like one of their own.

Thank you to my friends, old and new, for their wisdom and support.

I'd like to recognize my classmates Sarah, Kevin, Darcy, Claire S., And Claire C. for making the journey a fun one. I can't imagine having gone through this experience under different circumstances, nor would I want to.

I've had the opportunity to work with a lot of great people at Mass Eye and Ear. A big thank you to Mike for taking the time to answer my many questions, even though he had a million other things to be doing, and Melissa for teaching me how to perform necessary surgical procedures.

Thank you to all of my committee members: Dr. Heidi Nakajima, Dr. Sunil Puria, Dr. Tao Cheng, Dr. Felipe Santos, Dr. Denny Freeman, Dr. Aaron Remenschneider, and Dr. Dan Merfeld. Thank you to all of the SHBT faculty members who have helped along the way.

I've had wonderful academic mentors over the years. Dr. Bob Celmer, the director of the acoustics program and University of Hartford, played a vital role in my academic journey. He cares deeply for his students, goes beyond what is expected of any professor, and, when needed, shows the tough love.

And finally, a huge thank you to John Rosowski. You treated me with respect, even when I made no sense, asked silly questions, and did not get your movie, book, and music references. You were completely invested in me as a person, not just as a student; you placed immediate importance on my health, relationships, and general interests, with academics being a close second. Most importantly, you are my friend. Thank you for everything.

Dedication

This work is dedicated to my parents, Nelson and Joanne. Without them, this manuscript would not exist. The path I chose after completion of high school was far from straight. My twenties were a wild ride. I made an attempt at college immediately after high school, moved to New York City for music, then moved back home to fight, with the help of my parents, a battle with mental illness. This was followed by another attempt at making it in the Big City. Finally, by the end of the decade, I decided to return to school. I was almost thirty before beginning college for the second time, and my parents lovingly reminded me of my record thus far. It wasn't a pretty one. They did not, however, dissuade me from returning to school. Instead, they gave me their full support. Although I worked many hours each weekend at a grocery store while in school, it would not have been enough without financial support from my parents, and for their help in that regard, I am extremely lucky and grateful. I will never be able to repay them, because what it would take is well beyond a dollar amount. This dissertation is for them, in hopes that in some small way, I can show them what they and their limitless love and support mean to me.

List of Tables and Figures

Tables

Figures

CHAPTER 1. Introduction

I. The auditory system

The mammalian auditory system collects acoustic energy from the environment, converts this energy to electrical signals, and processes the electrical information to enable auditory perception. The processes involved in this rudimentary description of hearing are quite impressive, if not amazing, as the ear can respond to sounds that produce motions of the auditory structure of less than 1 nm. The dynamic range of hearing of humans is approximately 6 orders of magnitude, and the frequency range of hearing covers 3 decades. A normal listener has the ability to discriminate between tones whose frequencies differ by less than 1 Hz, and between intensities that differ by less than 1 dB.

The auditory system consists of the two sub systems: the peripheral auditory system, which comprises the external, middle, and inner ear, and the central auditory pathway, part of the nervous system spanning the cochlear nucleus to the auditory cortex. The external and middle ears are responsible for transmitting sound pressures to the inner ear, where these pressures are transduced to electrical signals, transmitted as neural signals and processed by the central auditory system.

II. Air-conduction hearing

When we think of hearing, we typically think of the air-conduction pathway. Sounds from the environment around us make their way to the external ear. The pinna acts as a filter, changing the spectral content of the acoustic signal, allowing us to better ascertain the location of a sound source in 3D space. The sound then travels down the external ear canal, arriving at the tympanic membrane. The oscillating pressure associated with the sound moves the tympanic membrane (or TM) and the connected middle-ear bones: the malleus, incus and stapes. As the

bones rock back and forth, the medial end of the stapes, its footplate, moves in and out of the inner ear, generating sound pressure within. The sound pressure inside the auditory inner ear (the cochlea) sets the basilar membrane and the attached organ of Corti (our hearing organ) into motions that excite the sensory hairs cells, generating action potentials in the auditory nerve, which are interpreted by the brain as sound. (Figure 1.1)

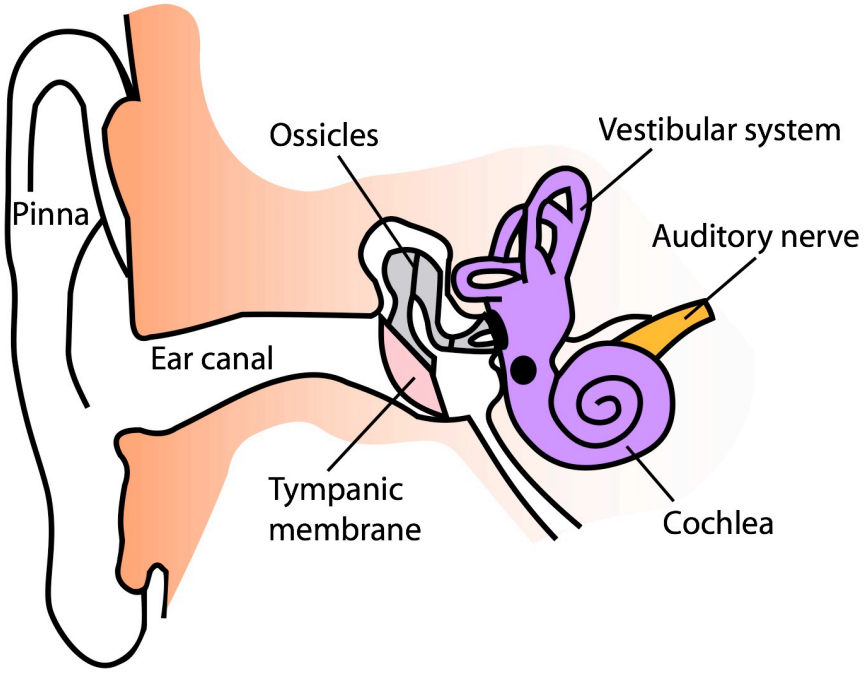

Figure 1.1. The human auditory periphery.
The human auditory periphery consists of the external ear (the pinna and ear canal), the middle ear (the tympanic membrane and ossicles), and the inner ear (containing the cochlea).

III. Bone-conduction hearing

A. History and theory

It has been understood for centuries that sound may be transmitted to the ear by vibrations of the skull rather than the air-conduction pathway described above —Cardano, Ingrassia, and Capivacci each described the phenomenon of 'bone-conducted sound' in the 16th century

(Kelley, 1937, Tonndorf, 1976). A few centuries later, in 1827, Charles Wheatstone experimented with the occlusion effect, an acoustic and perceptual phenomenon of bone conduction related to occluding the entrance of the external ear; this effect is the basis for multiple basic hearing tests designed to diagnose conductive hearing loss. Within the same century, further investigation of bone conduction by Weber, Rinne, Schwabach, and others led to the practice of comparing air-conducted and bone-conducted responses to evaluate the condition of the ear (Olsen, 1990). When middle-ear function has been compromised, sound conduction via bone vibration is relatively little affected; yet the same middle-ear pathology generally has a much larger effect on the air-conduction (AC) pathway. Hence, audiometric thresholds will be increased for AC stimulation, while BC stimulation thresholds are relatively unaffected. This difference in BC and AC thresholds, known as the 'air-bone gap', is an indication that ear-canal sound pressure (ECSP) is not properly transmitted to the inner ear.

For many years after bone-conduction hearing was first described, it was unknown as to whether there were separate organs of hearing for bone conduction and air conduction. In 1932, von Békésy performed a test to determine if this were the case. In his experiment he presented a listener with an air-conducted tone, while simultaneously presenting a tone of the same frequency through bone-conduction stimulation. The test-subject was able to control the amplitude and phase of the bone-conducted tone. The hypothesis was that if both forms of sound conduction stimulate the same organ, then a bone-conducted tone of the same frequency and amplitude, but opposite phase, would cancel out the effect of the air-conducted tone on the common sensory structure. Indeed, this was the result of his experiment. Although the original experiment was performed with a tones of a single frequency, 400 Hz, it has been repeated and

extended to cover a greater frequency range in humans (Stenfelt, 2007), cats and guinea pigs (Lowy, 1942).

The theory of bone conduction has evolved over time, but, generally speaking, ideas regarding the mechanisms driving this mode of hearing have not changed much. It has long been agreed that the external, middle, and inner ear are somehow involved, but the degree to which they contribute to bone-conduction hearing has eluded researchers. For example, it is clear from the occlusion effect that altering the condition of the ear canal can alter our perception of bone-conducted sound. Theories about a possible external-ear bone-conduction component have involved compression of the ear canal walls, motion of the lower jaw relative to the skull, and motion of the tympanic membrane. It is also thought that several mechanisms directly stimulate the inner ear. For example, the inertia of the cochlear fluids and compression of the cochlear boundary have been hypothesized to result in perceivable sound pressures within the inner ear. Another possible mechanism is the transmission of sound pressure from the brain to the inner ear through ducts supplying the inner ear with lymph. The ossicles of the middle ear may also play a role in bone-conduction hearing. Vibrations of the head can cause these bones to move relative to the cochlea, generating sound pressures within the cochlea, in a similar manner to the ossicular motions produced by airborne sound.

B. Clinical importance of bone conduction

In-office tuning-fork tests of air and bone conduction, such as the Rinne test, are diagnostic tools to quickly assess the condition of the middle ear. During a Rinne test, a clinician places a vibrating tuning fork on the mastoid of the patient to provide bone-conduction stimulation. When the patient can no longer hear the tone, the still-vibrating tines of the tuning fork are moved

nearby the entrance of the ear canal, at which point the patient should once again hear the tone, as the elicited response to air conduction should be greater than that of bone conduction. If the air-conducted sound is not perceived, this is an indication that the transmission pathway from external ear to inner ear is compromised.

The Bing test makes use of the occlusion effect, which is the expected increase in perceived bone-conduction sound when the external ear canal is occluded, specifically at low frequencies. This effect is due to the increased impedance of the occlusion-terminated canal, redirecting most of the volume velocity generated in the external ear by the bone-conduction stimulus into the middle ear, resulting in increased intracochlear sound pressure, and an increase in the perceived loudness of the stimulus. When the ear canal is occluded in persons with conductive hearing loss due to ossicular fixations or discontinuities, little to no change in loudness is experienced as the pathology interferes with the contribution of the increased ear-canal sound pressure to intracochlear sound pressure.

The occlusion effect has implications beyond diagnoses of middle-ear condition. The effect can result in an undesirable increased perception of self-generated speech, specifically at low frequencies in persons using molded hearing aids that are inserted into the ear canals (Killion, 1988). An idea that the cartilaginous portion of the canal is responsible for the sound pressure generated within the ear canal by bone vibration has led researchers to suggest that a deep-seated hearing-air would reduce the unwanted increase in perceived self-generated speech. Venting of the ear mold allows for some relief of this effect, as the vent reduces the amount of sound energy entering the middle ear.

Bone-conduction hearing aids have been used by thousands of people around the world to treat conductive hearing loss. These devices are similar to air-conduction hearing aids in that

they receive an acoustic signal from the environment and transduce the signal in such a way that it could be presented to the user in a more-accessible way. In the case of air-conduction hearing aids, the audio signal is boosted by electronics and transformed back into an acoustic signal within the ear canal. In the case of bone-conduction hearing aids, after the signal is picked up by the device's microphone, the device vibrates the head, or skull, directly. The vibrations then follow one or more of the several bone-conduction pathway to the inner ear.

Conductive hearing loss affects a great number of people. A study by Frear and Nakajima (2019) looked at approximately 175,000 patients that visited Massachusetts Eye and Ear infirmary over the course of 3 years. Approximately 60% of these patients who described having some issue with hearing were determined to have some form of conductive hearing loss, while 27% were diagnosed with sensorineural hearing loss (typically an issue with the sensory organ of hearing). Of these patients, approximately 16% had a form of conductive hearing loss that was potentially treatable by surgery. In certain cases, the use a bone-conduction hearing aid may be a successful form of treatment.

C. Commercial bone-conduction devices

In recent years, there has been an increase in commercial bone-conduction devices, to be used similar to headphones, that have entered the market. This has been motivated in part by the desire to listen to audio while simultaneously being aware of the environment. This may be important, for example, for runners or cyclists who are performing their activity in busy cities. Typical headphones that use air-conduction technology block the ear canals, causing a loss in awareness of the surroundings, and make it difficult to detect threats, such as vehicles, that are

not in plain sight. Bone-conduction devices offer a solution to this issue, as they leave the ear canals open, while simultaneously transmitting acoustic information via an osseous route.

The use of bone-conduction transducers allows persons to use hearing protection to reduce exposure to air-conducted noise. The threshold of bone-conduction hearing, resulting from the air-conducted sound vibrating the head, is approximately 60 dB greater than that of air-conducted sound through the typical air-conducted pathway. It is difficult to prevent acoustic trauma from bone-conducted sounds as a result of airborne noise.

IV. Aim of this study

In bone-conduction hearing, there are several potential sound transmission pathways to the inner ear. The relative contributions and associated frequencies of these pathways to bone-conduction hearing are not fully understood. This study aims to elucidate the contribution of each of these pathways, or "sources", to bone-conduction hearing, and to develop a lumped-element circuit model to investigate the effect of certain pathologies on bone-conducted hearing. The approach of this study was as follows: 1) An air-conduction hearing model was developed for the chinchilla. 2) The air-conduction model was expanded by including a transmission line model of the external ear canal. 3) Bone-conductions sources within the external ear source were characterized using new BC-induced ear canal sound pressure and skull vibration measurements, and added to the model. 4) The model's cochlear network was expanded by the addition of the vestibular and cochlea aqueduct, and an explicit representation of the cochlear scalae. 5) A method was developed to characterize the inner ear BC source components by the combined use of intracochlear sound pressure measurement and the circuit model. 6) The fit of the model to

inner-ear sound-pressure measurements made with various manipulations of ear structure were evaluated.

By better understanding the mechanisms of bone-conduction, it may be possible to devise methods of diagnosing conductive and sensorineural hearing loss, allowing doctors to more easily determine the exact pathology. This increased understanding may drive advancements in hearing aid technologies, and commercial bone-conduction devices.

CHAPTER 2. Chinchilla air-conduction model of hearing

(published: Bowers et al. 2019)

Abstract. An air-conduction circuit model was developed for the chinchilla middle ear and cochlea. The lumped-element model is based on the classic Zwislocki model of the same structures in human. Model parameters were fit to various measurements of chinchilla middle-ear transfer functions and impedances, using a combination of error-minimization-driven computer-automated and manual fitting methods. The measurements used to fit the model comprise a newer, more-extensive data set than previously used, and include measurements of stapes velocity and inner-ear sound pressure within the vestibule and the scala tympani near the round window. The model is in agreement with studies of the effects of middle-ear cavity holes in experiments that require access to the middle-ear air space. The structure of the model allows easy addition of other sources of auditory stimulation, e.g. the multiple sources of bone-conducted sound—the long-term goal for the model's development—and mechanical stimulation of the ossicles and round window.

I. Introduction

Middle-ear models have been used for many years to investigate how the ear transforms sound pressure at the tympanic membrane to sound pressure in the inner ear. The lumped-element circuit model developed by Zwislocki (1962) was designed to fit measurements of middle-ear input impedance in humans in response to air-conducted sound and is the starting point for more-recent models (Kringlebotn, 1988; O'Connor and Puria, 2008). One benefit of these models is that the effects of pathological changes in ear structure can be predicted by altering the circuit element values and structure (Rosowski and Merchant, 1995; Songer and Rosowski, 2007a). Kringlebotn (1988) built on the Zwislocki model, with a focus on the effect of acoustic energy reflectance at the ear drum and the mechanical coupling between the eardrum and its suspension. In another variation of the Zwislocki model, O'Connor and Puria (2008) modeled the tympanic membrane (TM) as a distributed-parameter transmission line to account for phase delays seen in the middle-ear gain and other transfer functions with an output at the cochlea. While finite-element models have also been used to investigate sound transduction to the inner ear by the tympanic membrane and the ossicular chain (Funnell *et al.*, 1992; Koike *et al.*, 2002; Gan *et al.*, 2004; Higashimachi *et al.*, 2013; Motallebzadeh *et al.*, 2017a), circuit models require less computational power and allow easy specification of the location and output of different sources of sound and vibration. Although various mathematical representations of chinchilla middle ears exist (Songer and Rosowski, 2007b; Wang and Gan, 2016), a lumped-element circuit model of the chinchilla middle ear has only been published recently (Lemons and Meaud, 2016).

While our model is similar in structure, it is unique to that of Lemons and Meaud (2016). Significant differences in parameter values occur because different data sets were used for

fitting: Lemons and Meaud (2016) fit the data of Songer and Rosowski (2007b), while the current model is fit to a more-extensive set of middle-ear and inner-ear data with all measurements made in the same set of ears (Ravicz and Rosowski, 2012; 2013a; b). Moreover, the error-minimization methodology we use, although used elsewhere (Puria and Allen, 1998; Keefe, 2015), was not employed for determining lumped-element model parameters in past models of the chinchilla middle ear and cochlea.

Similarities between chinchilla and human auditory peripheries make the chinchilla a good choice of animal model for hearing research, where the intent is to adapt the model for study of the human auditory system. The behavioral frequency range of hearing in chinchilla extends from approximately 50 Hz to 33 kHz, while the range of hearing in a young, normal-hearing human is approximately 20 Hz to 20 kHz. The surface area of the human TM and stapes footplate are approximately 0.68 cm^2 and 0.030 cm^2 (Hemila *et al.*, 1995), respectively, while those of the chinchilla are approximately 0.56 cm^2 and 0.020 cm^2, respectively (Vrettakos *et al.*, 1988). While the chinchilla has a relatively large middle-ear air volume (2 cm^3) (Ruggero *et al.*, 1990), which like that of human is broken into multiple air spaces (Browning and Granich, 1978), the total volume is about a third of that of the average human air spaces (Molvaer *et al*., 1978) and there is no region that contains the small interconnected air cells found in the human mastoid.

The long-term goal of this research is to use this new model to guide investigations of the multiple mechanisms by which body vibrations (conducted to the inner ear via bone conduction) stimulate the inner ear. This goal has shaped this investigation, primarily in our concentration on sounds of frequencies of 10 kHz and lower.

II. Methods

A. Basic circuit model and model transfer functions

The air-conduction circuit model for chinchilla (Figure 2.1) is a modification of the Zwislocki (1962) model with that model's simple form and a relatively small number of elements. The model has 5 anatomically distinct segments: (**a**) the air-filled middle-ear cavity, (**b**) ossicle-uncoupled TM, (**c**) ossicle-coupled TM, malleus, and incus, (**d**) incudostapedial joint (ISJ), and (**e**) the stapes, cochlea, and cochlear windows.

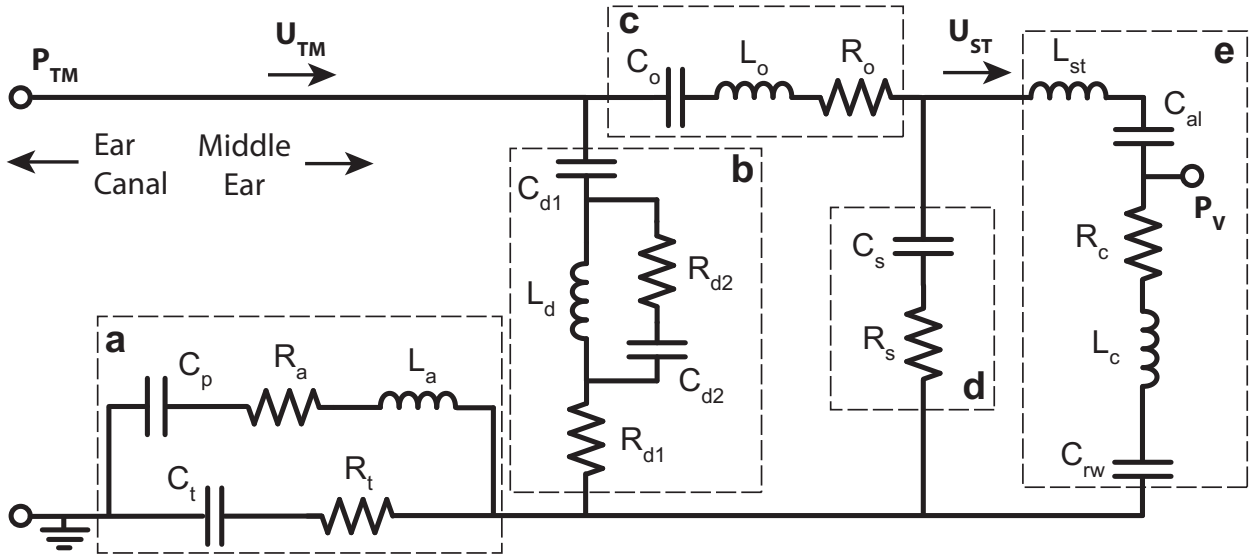

Figure 2.1. Circuit model of the intact chinchilla middle ear.
Anatomically distinct segments are: (**a**) middle-ear cavity, (**b**) ossicle-uncoupled TM, (**c**) ossicle-coupled TM and malleus-incus complex, (**d**) incudostapedial joint, and (**e**) stapes, cochlea, and cochlear windows. Parameter subscripts: *a* – aditus to the superior cavity, *t* – tympanic cavity, *p* – superior cavity, *d#* - ossicle-uncoupled TM, *o* – ossicle-coupled TM and malleus-incus complex, *s* – incudostapedial joint, *st* – stapes, *al* – annular ligament, *c* – cochlea, *rw* – round window.

The circuit model is a ladder network with combinations of series and parallel elements arranged in several branches. The parallel branches (**b** and **d**) model divergent paths for stimulus energy within the eardrum and ossicular joints, both of which "shunt" a fraction of the stimulus away from the inner ear. These shunt paths account for relative motions within the TM and the ossicular chain (Huber *et al.*, 2001; Rosowski *et al.*, 2003; Nakajima *et al.*, 2005). Humans have potentially two ossicular shunts: the incudomalleolar joint (IMJ) and the incudostapedial joint (ISJ). In the chinchilla, the IMJ is ankylosed, therefore shunting within the ossicles in chinchilla is attributed to compliance in the ISJ or the ossicles themselves due to bending (Funnell *et al.*, 1992). Shunts of the latter type would be included in model branch **b**. The model was solved in the sinusoidal steady state, and while its parameter values are all real numbers, the branch and nodal currents and voltages are complex numbers with both a magnitude and a phase.

The model represents sound pressures as voltages and volume velocities as currents. Descriptions of middle-ear function usually include the transformation of sound energy that reaches the inner ear by the ratio of the areas of the TM and stapes footplate ($A_R = A_{TM}/A_{ST}$), and the ratio of the lengths of the malleus and incus lever arms ($L_R = L_m/L_i$) (Dallos, 1973). However, Figure 2.1 includes no explicit transformers. Instead, the transformers are implicitly included in the model parameters and the internal circuit volume velocities ($\mathbf{U_{ST}}$) and sound pressures ($\mathbf{P_V}$) values. To compute the actual scala vestibuli sound pressure and stapes volume velocity (i.e. $\mathbf{P_V'}$ and $\mathbf{U_{ST}'}$), one needs to remove the transformation, e.g.:

$$\boldsymbol{P_V' = P_V A_R L_R} \tag{2.1}$$

$$\boldsymbol{U_{ST}' = U_V \frac{1}{A_R L_R}} \tag{2.2}$$

The model variables with the transformers removed are used to compute two transfer functions (the middle-ear gain – **GME**, and the stapes-velocity transfer function – **SVTF**) and the cochlear input impedance $\mathbf{Z_C}$, specifically:

$$\boldsymbol{GME = P'_V / P_{TM}} \tag{2.3}$$

$$\boldsymbol{SVTF = V'_{ST} / P_{TM}} \tag{2.4}$$

where the velocity of the stapes $\mathbf{V'_{ST}}$ is $\mathbf{U'_{ST}}$ divided by the area of the stapes footplate, and

$$\boldsymbol{Z_C = P'_V / U'_{ST}} = (\boldsymbol{P_V / U_V})(A_R L_R)^2 \tag{2.5}$$

The model directly defines (without the need for transformers) the volume velocity at the TM, $\mathbf{U_{TM}}$, and the sound pressure at the TM in the ear canal, $\mathbf{P_{TM}}$. The ratio of these variables describes the middle-ear input impedance:

$$\boldsymbol{Z_{ME} = P_{TM} / U_{TM}} \tag{2.6}$$

All four of these system functions (Equations 2.3-2.6) are implicit functions of frequency.

B. Modification of the middle-ear cavity model to fit measurement conditions

The model of the middle-ear air spaces in branch **a** of Figure 2.1 describes the circumstance where the middle-ear cavity is split between two major air spaces: one directly behind the TM with compliance C_t, and a second superiorly-positioned space with compliance C_p that is connected to the first by a foramen, or *aditus*, with resistance R_a and inertance L_a. This description can be generally applied to the chinchilla, even though the two model volumes actually represent the combined volumes of multiple inter-connected air spaces (Browning and Granich, 1978). The model of Figure 2.1 represents air-filled cavities that are naturally closed to the outside via bony walls; however, most measurements of middle-ear function require opening

the bony walls for manipulations of middle-ear muscles, observation of the ossicles, or the placement of microphone probes within the inner ear (Songer and Rosowski, 2006; Ravicz and Rosowski, 2013a; b). Modeling this 'open cavity' condition requires adding elements to model the inertances (acoustic masses) associated with sound flow through the openings in the bone, and the radiation impedances from these openings to the outside world (Figure 2.2).

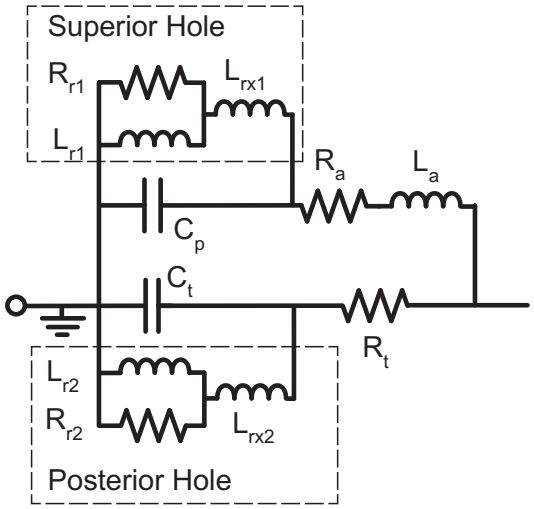

Figure 2.2. Circuit model of the chinchilla middle-ear cavity.
The addition of six elements to the cavity model of branch **a** in Figure 2.1 to account for 1) the placement of a hole into the superior cavity of the chinchilla middle ear (subscript *1*), and 2) the placement of a hole into the posterior wall of the tympanic cavity (subscript *2*). Each hole is modeled by the addition of an inertance ($L_{rx\#}$) that models sound flow through the hole, placed in series with a parallel inertance and resistance (subscript *r#*) modeling the impedance associated with radiation of the sound into the atmosphere (Beranek, 1993).

C. Parameter values set by anatomy and structure

Where possible, model parameters were determined from anatomical values. The compressibility (compliance) of air within closed and nearly-closed cavities, and the compliances of membranes and joints are described by electrical capacitors. Translationally-oscillating media

of known mass (i.e. inertance) and moments of inertia of mechanical masses that undergo rotational motion are represented as inductances. Damping and energy absorbance within the ear are represented by resistors. The middle-ear cavity compliances were constrained by the measurements of the equivalent volume of the combination of the two compliances made by Rosowski *et al*. (2006):

$$C_p + C_t = C_{total} = \frac{Vp+Vt}{\rho_{air} c_{air}^2} = \frac{Vtotal}{\rho_{air} c_{air}^2} \quad (2.7)$$

where ρ_{air} is the density of air, c_{air} is the speed of sound in air, V_p and V_t are the volumes of the superior and tympanic cavities, and V_{total} = 2 cm^3. The masses of the malleus-incus complex and the stapes are related to the inertances L_o and L_{st} by the appropriate transformer values:

$$L_o = (malleus + incus\ mass) \,/\, {A_{TM}}^2 \quad (2.8)$$

$$L_{st} = stapes\ mass \,/\, \left({L_R}^2 {A_{TM}}^2\right) \quad (2.9)$$

As the stapes inertance L_{st} is in series with that of the cochlear inertance L_c, and the Zwislocki model does not distinguish between the two, the early optimization passes (Steps 1–5 described below) were made with L_{st} set to zero. Later, the stapes inertance was constrained by Equation 2.9.

D. Computer-automated objective optimization procedures

As is described in more detail below, the techniques for estimation of circuit model parameters included multiple passes through a computer-automated objective optimization procedure. This fitting procedure involved iterative perturbations of model parameters to produce a 'best' fit of model outputs to the magnitude and phase of experimentally determined system functions. The MATLAB function *fminsearch* was adapted for this purpose. The computed outputs of either the entire circuit model or particular model segments were fit to experimental

data describing the magnitude and phase of system equations relevant to either the complete model or the studied segment, using the Nelder-Mead simplex method (1965) for solving multidimensional optimization problems invoked by *fminsearch*. This iterative method produced an 'optimum' parameter set associated with a minimum in a 'cost' function.

Ideally, the cost associated with the fit to each data set is the mean of the square of the difference between the model output and the experimental data normalized by the experimental data at each frequency point summed over m frequencies (Equation 2.10), where y is the model output and y_o is the experimental data. This normalization converts the deviation into a fraction of the measured values. This generalized formula was sufficient for fitting the model to phase data (after adding 2π to each of the phases as described below). In the case of magnitudes, because the experimental data range over several orders of magnitude, the logarithm (base 10) of both the experimental and model magnitudes were used to estimate the cost (Equation 2.11), as non-logarithmic cost estimates that include normalization by the target value emphasized the fit at data regions with small magnitude and high signal-to-noise ratios. The calculation of the logarithmic magnitude costs in Equation 2.11 did not include explicit normalization to the experimental data, as the calculation of the logarithm provided an implicit normalization to the common reference value, where the log quantities were implicitly referenced by a value of 1 of the same units (e.g. a reference value of 1 mm–$s^{-1}Pa^{-1}$ was used to convert the model and measured |**SVTF**| to log values). The total cost (Equation 2.12) is the root-mean-square of the costs associated with the $n = 6$ system equations (3 magnitude and 3 phase). Equal weight was given to the cost of the magnitude and phase of the transfer functions, and each transfer function was weighted equally.

$$\text{cost}_{\text{phase}} = \sqrt{\frac{\sum_m \frac{(y-y_o)^2}{y_o^2}}{m}} \tag{2.10}$$

$$\text{cost}_{\text{magnitude}} = \sqrt{\frac{\sum_m [\log(y)-\log(y_o)]^2}{m}} \tag{2.11}$$

$$\text{total cost} = \sqrt{\frac{\sum_n (cost)^2}{n}} \tag{2.12}$$

The measured and model phases in some frequency ranges originally included zero as a possible value. Since normalization by a measured phase near zero would greatly increase the cost (Equation 2.10), a +2π shift was applied to the wrapped experimental and model phases before the cost was calculated. This cycle phase-shift was undone before plotting the results.

The first set of parameter values for the initial iteration of the model were based on an optimized version of the Zwislocki human middle-ear model parameters (Bowers and Rosowski, 2016). The application of *fminsearch* results in the iteration of perturbations of all variable parameter values simultaneously, and the calculation of the total cost associated with the updated parameter set.[1] For each run, this repeated perturbation and recalculation of the cost was iterated (on the order of 10000 times) until the predicted parameters stabilized at an 'optimum' value. An example of how the parameter values were altered during a single optimization run is illustrated in Figure 2.3.

[1] At the start of an optimization run, a set of n+1 vertices is created in an n-dimensional space, where n is the number of parameters being optimized. Each vertex comprises the initial parameter values, with a single, unique parameter value adjusted by 5%. The set also includes a vertex having coordinates of the initial parameter set without adjustment. The cost resulting from each vertex (parameter set) is calculated, and the centroid of the n lowest-cost vertices is calculated. The highest-cost vertex is subjected to multiple transformations, about the centroid of

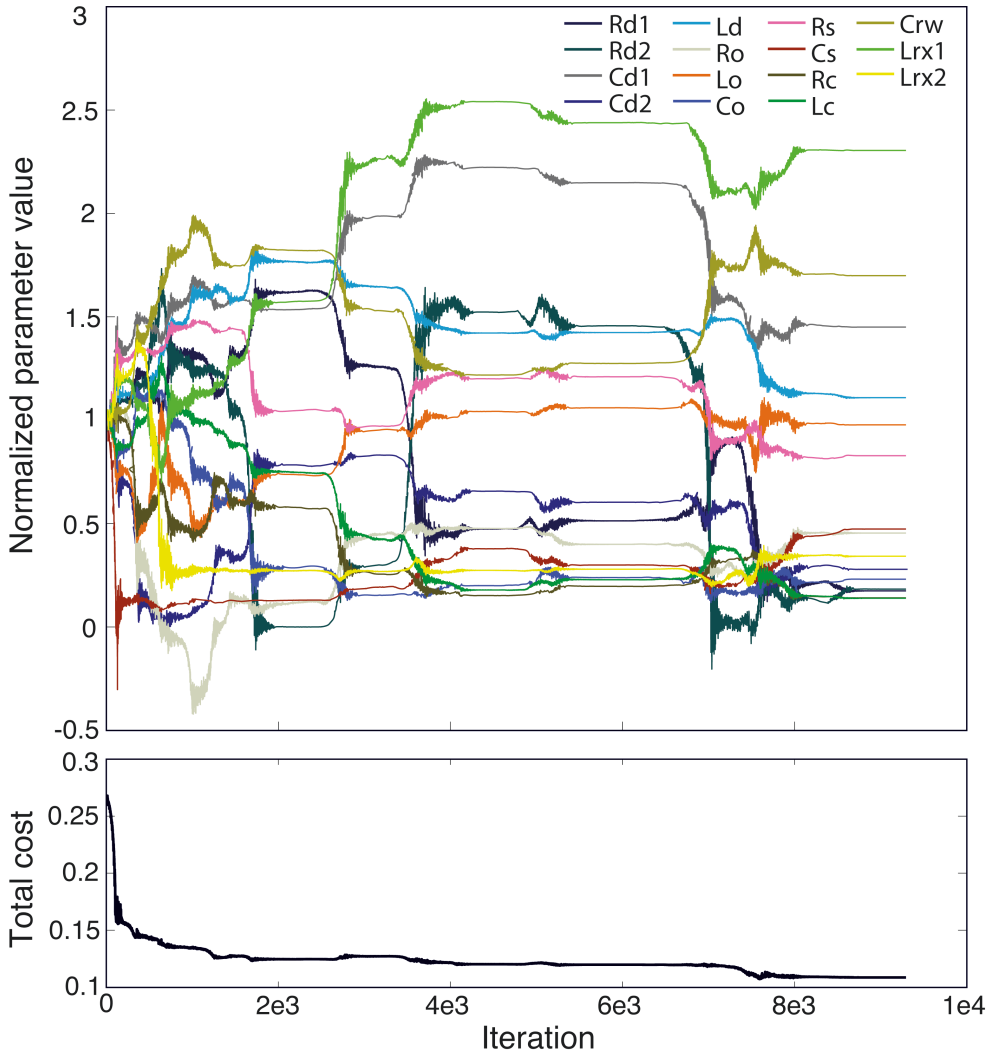

Figure 2.3. Visualization of circuit-model parameter optimization.
An example of a single automated objective optimization run of the MATLAB *fminsearch* algorithm. Parameter values normalized by their starting 'initial' value are shown as a function of the number of iterations of the algorithm. Total cost is calculated using Equation 2.12 and accounts for fitting the model to the magnitude and phase of $\mathbf{Z_{ME}}$, **SVTF**, and $\mathbf{Z_C}$. Significant changes in parameter values occurred during the first 8000 iterations, but stability was achieved by 9500 iterations.

Due to the high probability of multiple local minima in the total cost associated with optimization of the 14 or more variable model parameters solved for in each iteration, hundreds of automated optimization runs (each of which included thousands of iterations) were performed after forced variations in the starting parameter values: before each run, we applied a separate randomized multiplication factor (over a specified range) to each of the parameter values used to initiate the optimization run. Each of these runs resulted in a unique set of parameters and a cost value. The final output of the hundreds of runs was the stable parameter set with the lowest cost.

A complication of the Nelder-Mead simplex method is that limits cannot be placed on possible parameter value solutions. In order to prevent negative parameter values (i.e. negative compliances, masses, or resistances), the absolute values of those chosen by the algorithm were used to calculate the system outputs at each iteration of the automated process.

E. Manual optimization procedures

To supplement the computer-automated objective optimization procedures, manual fitting procedures were implemented. The purpose of manual fitting was either to test whether the model could be improved beyond what the automated process produced, or to correct the objectively-fit parameters to anatomically realistic values. The manual fitting procedures were guided by (i) visual inspection of the model outputs relative to the experimental data and (ii) 'sensitivity analyses' that tested how controlled changes in each of the parameter values altered the cost of the model.

Visual inspection was performed via a graphical user interface (GUI) (supplemental Figure A.1). The GUI allowed adjustment of individual parameter values while displaying in real-time

the predicted model transfer functions superimposed on the measured data, and the cost associated with the adjusted model parameter set.

The sensitivity analyses tracked how the total cost was affected by isolated ±5, ±10 and ±20% changes in each of the individual parameters. Those changes in parameter values that led to decreases in cost indicated a less-than-optimal fit to the data. The single parameter that produced the largest alterations in cost was identified and its value set to minimize cost. The analysis was repeated until the parameters appeared optimum. The change in cost as a function of parameter value perturbation is not necessarily monotonic, hence it is important to examine varying degrees of change. For example, increasing a parameter by 5% may increase cost, but further increases in the same parameter value may result in a cost reduction. If all parameter changes increase the cost, the given parameter set is judged a potential globally-optimal set.

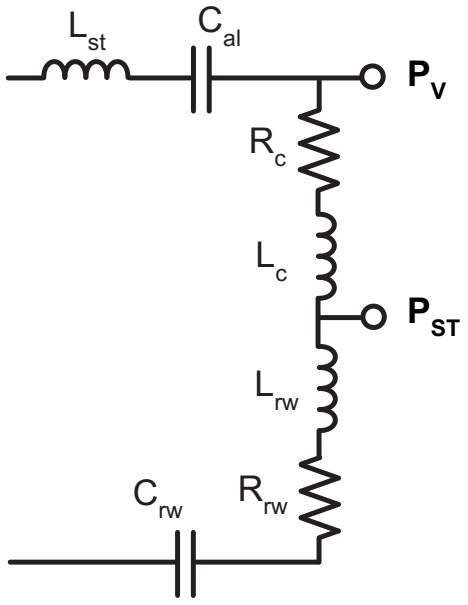

Figure 2.4. Expanded cochlear network.
Expanded cochlear network. An inertance L_{rw} and resistance R_{rw} were added to the cochlear network, allowing calculation of the sound pressure in the scala tympani $\mathbf{P_{ST}}$.

F. Estimation of round-window compliance

After multiple sets of automated and manual optimizations determined an optimum set of model parameters for the elements described in Figures 2.1 and 2.2, the cochlear network of the original Zwislocki model was expanded to include several new elements that allowed model estimates of scala tympani sound pressure ($\mathbf{P_{ST}}$). Fitting the expanded model to $\mathbf{P_{ST}}$ measurements helps constrain the round-window compliance, and allows future model calculations of the pressure difference across the cochlear partition. In experiments by Ravicz and Rosowski (2013a), sound pressures were measured simultaneously in the ear canal near the TM and in the two cochlear scalae, including the sound pressure in the scala tympani near the round window.

To enable accurate estimation of $\mathbf{P_{ST}}$, two elements were added to the cochlear network (Figure 2.4): an inertance to model the mass of a column of water-like perilymph between the scala tympani sound-pressure sensor and the round window (L_{rw}), and an associated resistance (R_{rw}). Such elements have been introduced in multiple previous studies that modeled measurements of $\mathbf{P_{st}}$ (Nedzelnitsky, 1980; Olson, 2001; Nakajima *et al.*, 2009; Frear *et al.*, 2018).[2] As was the case for the vestibule sound pressure, the prediction of the target $\mathbf{P'_{ST}}$ was calculated by removing the implicit effect of the middle-ear transformers on the model representation of $\mathbf{P_{ST}}$:

$$\boldsymbol{P'_{ST}} = \boldsymbol{P_{ST}} A_R L_R \tag{2.13}$$

[2] The physical cause of these additional elements has been associated with either the force used to move the small column of fluid between the $\mathbf{P_{ST}}$ measurement point and the round window (RW), the mass and resistance of the RW, or some combination. The fitted acoustic inertance we define as L_{rw} can be attributed to cylinder of water or cross-section equal to the RW area and length of 1.25 mm. The computed length is a good approximation of the distance between the RW and the $\mathbf{P_{ST}}$ measurement location (Ravicz and Rosowski, 2013a).

A single automated optimization run was used to find the values of C_{rw}, L_{rw}, and R_{rw} that best fit measurements of $\mathbf{P'_{ST}}$ normalized by the sound pressure in the ear canal $\mathbf{P_{TM}}$ (Ravicz and Rosowski, 2013a).

Constrain 9 of the independent middle-ear cavity parameters

Step 1) Estimate C_p, C_t, and L_a from intact-cavity impedance measurements
Step 2) Define R_a and R_t by 200 runs of automated optimization; L_h requied
Step 3) Use the two cavity-hole radii to constrain the radiation impedances R_{r1}, R_{r2}, $L_{r1,}$ and L_{r2}

Computer-automated optimization of 14 middle-ear and cochlear parameters; cavity parameters defined above and transformer ratios fixed by anatomy

Step 4) 200 automated runs with initial values varied by a factor of $10^{\pm 3}$
Step 5) 200 automated runs with step 4 values varied by a factor of $10^{\pm 3}$

Manual adjustment of 26 model parameters

Step 6) Constrain stapes inductance L_{st} by stapes mass; introduce L_{rx1} and L_{rx2}
Step 7) Manual fitting of all defined model parameters using GUI and cost estimate
Step 8) Repeated sensitivity analyses to fine-tune all parameters

Computer-automated optimization of 16 middle-ear and cochlear parameters; cavity parameters, transformer ratios, and stapes inductance fixed by step 8

Step 9a) 200 automated runs with step 8 values varied by a factor of $10^{\pm 0.25}$
9b) 100 automated run with step 8 values varied by a factor of $10^{\pm 0.5}$
9c) 100 automated run with step 8 values varied by a factor of $10^{\pm 1}$
9d) 100 automated run with step 8 values varied by a factor of $10^{\pm 2}$
9e) 100 automated run with step 8 values varied by a factor of $10^{\pm 3}$

Manual adjustment of 26 model parameters

Step 10) Adjust L_{rx1} and L_{rx2} for consistency with anatomic cavity volumes
Step 11) Repeated sensitivity analyses to fine-tune all parameters

Expansion of cochlear network to include L_{rw} and R_{rw}

Step 12) One automated run with all but C_{rw}, L_{rw}, R_{rw}, $L_{c,}$ and R_c fixed; L_{rw}+L_c and R_{rw}+R_c are constrained by Step 11 L_c and R_c ,respectively.

Figure 2.5: Flow chart of model development.

G. Complete procedure for fitting model elements

The procedures for determining the model parameters that best describe the transmission of air-conducted sound through the chinchilla middle ear are summarized in Figure 2.5. Our process tries to minimize the number of free parameters that are subject to optimization by exploring different sections and elements by optimization while separated from other parts of the circuit. Figure 2.5 describes 12 steps.

Steps 1 through 3 describe the initial concentration on an accurate and complete model of the air-filled middle-ear cavity based on the model structure and published measurements of the acoustic impedance of the cavities (Rosowski *et al.*, 2006). (Optimization of 9 model parameters.) In Step 1, measurements of the cavity impedance at low and middle frequencies were used to fix values of the cavity volumes (directly related to C_p and C_t) and inertance L_a of the aditus that connects them. In Step 2, the circuit structure of branch **a** in Figure 2.1 with circuit parameters defined by Step 1, and initial parameters for R_a, R_t, and L_a from the Zwislocki circuit were used as inputs to 200 automated optimization runs used to fix R_a, R_t, and L_a for later fitting procedures. In Step 3, estimates of the radii of the two openings into the middle-ear cavity were used to fix the four radiation impedance parameters included in Figure 2.2 (L_{r1}, L_{r2}, R_{r1}, and R_{r2}). The additional inertances in Figure 2.2 (L_{rx1} and L_{rx2}) were set to zero.

Steps 4 and 5 are independent sets of 200 computer-automated objective optimization runs to fit the magnitude and angle of $\mathbf{Z_{ME}}$, **SVTF**, and $\mathbf{Z_C}$ measured with the middle-ear cavities in the open state. In these steps, the cavity model parameters were fixed at the values defined by Steps 1 through 3, and A_R and L_R (area and lever ratios) were fixed at their anatomically-defined values. For reasons described above, the inertance associated with the stapes mass L_{st} was also fixed at zero. The 14 other elements in branches **b** through **e** of Figure 2.1 were adjusted in both

steps. In Step 4, human-defined initial values were used for all varied elements, and each initial value was individually randomly varied (by a factor between 0.001 and 1000) before each of a series of 200 optimization runs. The 14 resultant parameters of the run with the lowest cost were used as initial values to Step 5. In Step 5, as above, before each of 200 optimization runs, each initial parameter value was individually varied by a random factor between 0.001 and 1000. The 14 resultant parameters of the Step 5 run with the lowest cost define these elements in further stages.

Steps 6 through 8 were manual adjustments of the model parameters guided by calculations of the cost of the fit. Step 6 introduced new model elements. The inertance of the stapes L_{st} was fixed at a value derived from its anatomical mass and the contribution of the two transformers (Equation 2.9). Additional cavity parameters L_{xr1} and L_{xr2} were added to the circuit, with initial values set by manual adjustments in the next step. Step 7 was a manual adjustment of the circuit values using the GUI to provide visual comparisons of the model predictions and the measured magnitude and phase of $\mathbf{Z_{ME}}$, **SVTF**, and $\mathbf{Z_C}$ with middle-ear cavities in the open state. Twenty-six parameters could be adjusted including: the two radii that fix the four radiation impedance elements in Figure 2.2, the other 22 elements of Figures 2.1 and 2.2 (including those added in Step 6), the TM area, and malleus-incus lever ratio. Step 8 was a complete sensitivity analysis on the individual effects of variations in each of the 26 model parameters to fine-tune the manual adjustments of Step 7.

In Steps 9a-e, computer-automated objective optimization runs were performed. Each substep of Step 9 allowed the optimization process to explore a unique range of initial values. Sixteen of the circuit parameters (including L_{rx1} and L_{rx2} introduced in Step 6) were variable, while the 9 middle-ear cavity parameters, the stapes inertance (L_{st}), and the two transformer

ratios (A_R and L_R) were fixed at the values defined by Step 8. All sub-steps of Step 9 used the fixed and modified parameter values of Step 8 as initial values, but a varying range of randomization factors ($10^{\pm n}$) was applied to the initial variables: in Step 9a, n = 0.25 (200 runs); in Step 9b, n = 0.5 (100 runs); in Step 9c, n = 1 (100 runs); in Step 9d, n = 2 (100 runs); in Step 9e, n = 3 (100 runs). The purpose of these repeated optimization-run sets was to search for the true global minimum in cost.

Steps 10 and 11 were manual adjustments. In Step 10, the GUI was used to manually adjust L_{rx1} and L_{rx2}, as the value of L_{rx1} from Step 9 was not anatomically realistic and because of the interplay between L_{rx1} and L_{rx2} and their effects on the middle-ear transfer-function outputs. All other parameters were fixed by the result of Step 9. The modification of L_{rx1} and L_{rx2} in Step 10 required adjustment of certain parameters; in Step 11, L_{rx1} and L_{rx2} were maintained at their manually set values, but the other 24 model parameters (including those associated with the middle-ear transformer ratios) were subjected to repeated manual sensitivity analyses for fine-tuning.

In Step 12, the cochlear network was expanded to allow predictions of the sound pressure in scala tympani near the round window ($\mathbf{P_{st}}$) by adding the inertance L_{rw} and resistance R_{rw} in series with C_{rw}. The values of L_{rw} and R_{rw} were constrained along with the values of L_c and R_c so that the total cochlear inertance and resistance were unchanged from that defined in Step 11. Specifically, the value of L_{rw} plus the new value of L_c must equal the value of L_c defined in the previous step. A similar constraint was placed on R_{rw} and R_c. New parameter values for L_{rw}, $L_{c,}$ R_{rw}, $R_{c,}$ (indirectly by varying $L_{ratio} = L_{rw}/(L_{rw}+L_c)$ and $R_{ratio} = R_{rw}/(R_{rw}+R_c)$) and an updated value of the round-window compliance C_{rw} were determined—optimization of 3 model parameters—by a single computer-automated optimization run (randomization of initial values did not

produce unique results) that fit the model outputs to the $\mathbf{P'_{ST}/P_{TM}}$ measurements of Ravicz and Rosowski (2013a). All other parameter values were fixed.

III. Model fits

A. Model of the middle-ear air spaces

The parameters of the two inter-connected chambers of the intact middle-ear cavity (branch **a** of Figure 2.1) that incorporate the tympanic and superior cavities (the former with volume approximately 3 times that of the latter, and both totaling approximately 2 cm^3) were independently analyzed from the rest of the model (TM, ossicles, and cochlea). Step 1 fixed the model parameters that describe the cavity compliances (C_t and C_p) and the inertance of the aditus (L_a) that connects them, based on a combination of manual and automated fittings to measurements of the input impedance of the cavity, with intact walls, made at frequencies between 0.1 and 2 kHz (Figure 2.6a). The low-frequency impedance (at 0.2 kHz, arrow 1 in Figure 2.6a) can be attributed to the parallel compliances of the two air-filled cavities, with the relationship described by the following equation:

$$\boldsymbol{Z_{MEC}}|_{f=0.2kHz} \approx \frac{1}{j\omega C_t(1+A_V)} \rightarrow C_t(1+A_V) = \frac{1}{j\omega Z_{MEC}|_{f=0.2\ kHz}} \tag{2.14}$$

where $\mathbf{Z_{MEC}}$ is the impedance of the middle-ear cavity, C_t is the compliance of tympanic cavity, A_V is the compliance ratio of the superior cavity C_p to the tympanic cavity C_t (which equals the ratio of the volumes of the superior and tympanic cavities), and the angular frequency is $\omega = 2\pi f$. Unlike human (Molvaer *et al.*, 1978), there is little inter-individual variation in the total volume of the chinchilla middle-ear cavity (Vrettakos *et al.*, 1988).

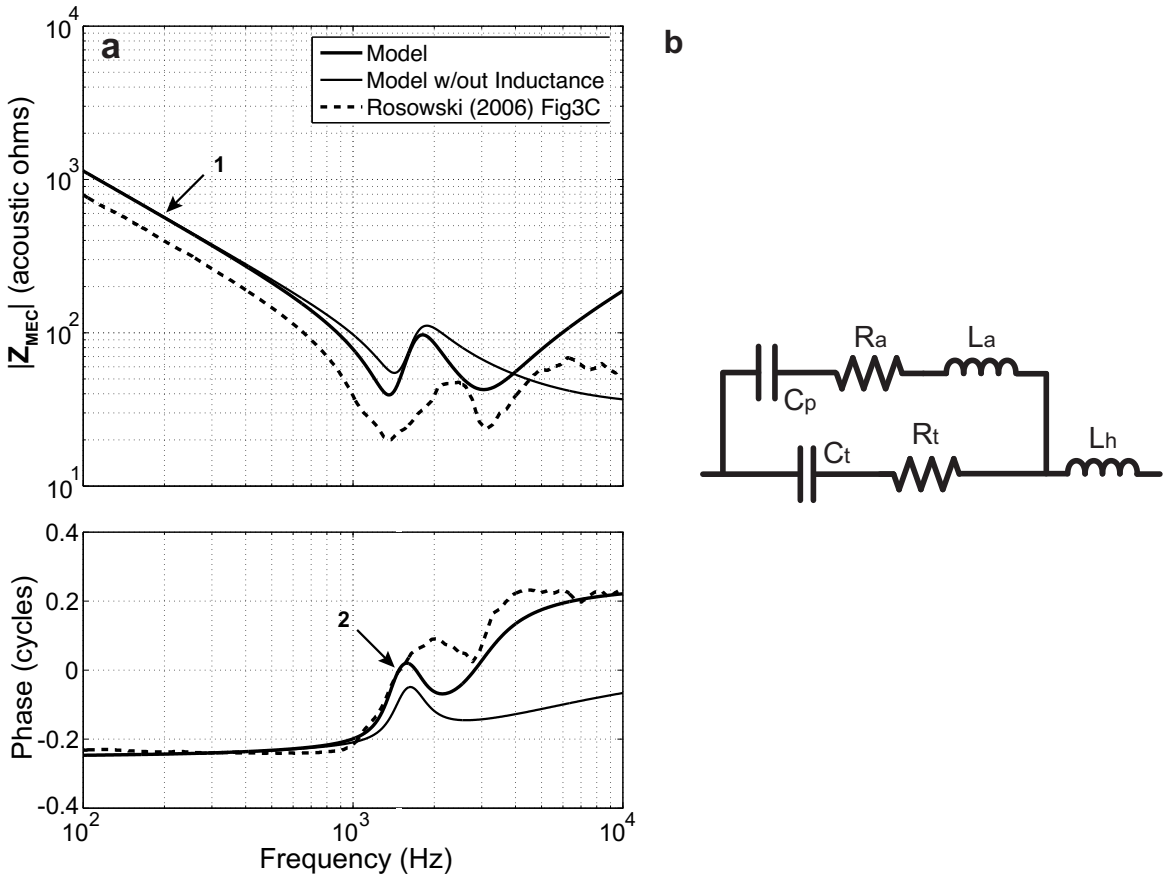

Figure 2.6 Middle-ear cavity.
Impedance of the fitted intact (no holes) middle-ear cavity superimposed on the averaged data of Rosowski *et al*. (2006). The middle-ear cavity model parameters were defined by fitting its parameter values to the measured data using a combination of observations from the mean impedance data and the automated optimization technique. Arrow 1 indicates the frequency at which the summed cavity compliances were estimated. Arrow 2 indicates the frequency at which the inertance L_a was calculated; (b) middle-ear cavity network with a series TM hole inertance that was included in the middle-ear cavity network during this step to represent the perforation in the TM (Voss *et al.*, 2001) that was present during the experimental measurements.

The process of determining the middle-ear cavity parameter values was repeated with A_V values between 0.2 and 0.4 with $A_V = 0.35$ yielding the lowest cost and best fit. The inertance L_a associated with the aditus between the two cavity regions was estimated from the frequency near the lower-frequency minimum in magnitude where the angle of the measured cavity impedance

is zero (at 1.49 kHz, arrow 2 in Figure 2.6a). The minimum in magnitude and zero angle of the impedance are due to the series resonance between L_a and C_p (Step 1); at the resonant frequency ω_o, the imaginary part of the cavity impedance is zero and L_a can be calculated from C_p and the square of the resonance frequency:

$$Imag[\boldsymbol{Z_{MEC}}]|_{f=1.49kHz} \approx j\omega_o L_a + \frac{1}{j\omega_o C_p} = 0 \rightarrow L_a = \frac{1}{\omega_o^2 C_p} \tag{2.15}$$

As noted by the thin solid line in Figure 2.6a, the cavity model described by branch **a** of Figure 2.1 explains many of the features of the cavity impedance measurements made in chinchilla (the dashed line in Figure 2.6a) at frequencies below 2.5 kHz, but it does not explain the second minimum in impedance magnitude and the increasing angle seen at higher frequencies. This difference probably occurs because the cavity impedance measurements were performed in chinchillas with large (~4 mm^2) TM perforations (Rosowski *et al.*, 2006). An appropriately-valued inertance (L_h) (Figure 2.6b) associated with such large perforations (Voss *et al.*, 2001) improved the model fit to the impedance at higher frequencies (thicker solid line of Figure 2.6a). In Step 2, the automated optimization process was used to determine a resistance of the tympanic cavity (R_t), resistance of the aditus (R_a), and the inertance L_h that best fit the measurement in Figure 2.6a, while C_t, C_p, and L_a were held constant with the values defined in Step 1. The magnitude of L_h determined by the optimization is 3.8e-3 kg–m^{-4}, and is consistent with a perforation size of 1.7 mm in radius (Equation 2.16; a and l are the radius and length of the perforation):

$$L_h \approx \rho_{air} l/(\pi a^2) + \frac{2\rho_{air} 0.8}{\pi a} \tag{2.16}$$

Equation 2.16 assumes that the inertance L_h accounts for the mass of air within the perforation as well as the mass portion of a radiation impedance at both ends of the perforation;

the resistance portion of the radiation impedance is not considered. While the contribution of L_h was important to fit the cavity model to the cavity impedance measurements of Rosowski *et al*. (2006) at the higher frequencies, the measurements used to describe branches **b** through **e** of the model were made with an intact TM, and the perforation inertance (L_h) was not included in our later analyses.

While the TM was intact in the measurements used to define the rest of the model, two holes were made in the middle-ear cavity to access structures within it: one hole opened the superior cavity to the outside (and allowed access to the tensor tympani tendon, which was cut in all of the measurements), and a second posterior hole opened the tympanic cavity to the outside (and allowed access for stapes velocity and inner-ear sound pressure measurements). In Step 3, we amended the cavity model structure to the model of Figure 2.2 that includes the effects of the holes and the impedance associated with sound radiation from the holes. The radiation impedances were defined by two elements in parallel (Figure 2.2), having parameter values that depend on the radius of the holes:

$$R_{r1,2} = \frac{\rho_{air} c_{air}}{\pi r^2} \tag{2.17}$$

$$L_{r1,2} = \frac{0.8\rho_{air}}{\pi r} \tag{2.18}$$

where R_r and L_r are the resistance and inertance associated with the radiation impedance, and r is the radius of the hole. Middle-ear cavity subscripts *1* and *2* note the superior cavity and tympanic cavity, respectively. Radii of 3.9 mm and 2.5 mm, estimated from a specimen used in the experiments of Ravicz and Rosowski (2013b), were used to calculate the radiation impedance parameters of the superior cavity and tympanic cavity holes, respectively.

B. Original automated fitting of 14 middle-ear and cochlea parameters: Steps 4 and 5

With branch **a** of Figure 2.1 replaced by the circuit of Figure 2.2, and with most elements of that branch fixed by Steps 1-3 (at this point L_{rx1} and L_{rx2} were set to zero), the parameters of the ossicularly-uncoupled TM (branch **b**), ossicle-coupled TM and malleus-incus complex (branch **c**), incudostapedial joint (branch **d**), and the series combination of the stapes inertance, annular ligament and oval window compliances, and cochlear elements (branch **e**) were approximated by automated fitting (Steps 4 and 5) to measured $\mathbf{Z_{ME}}$, **SVTF**, and $\mathbf{Z_c}$ data (2012; 2013a; b). (The stapes inertance was set to zero and unchanged throughout this fitting step.)

Figure 2.7. Outputs of model at various stages of optimization.
Outputs of model Steps 3, 5, 8, and 12 with superimposed experimental data. Model fits are compared to experimental data of Ravicz and Rosowski (2012; 2013a; b).

Figure 2. 7 (continued)

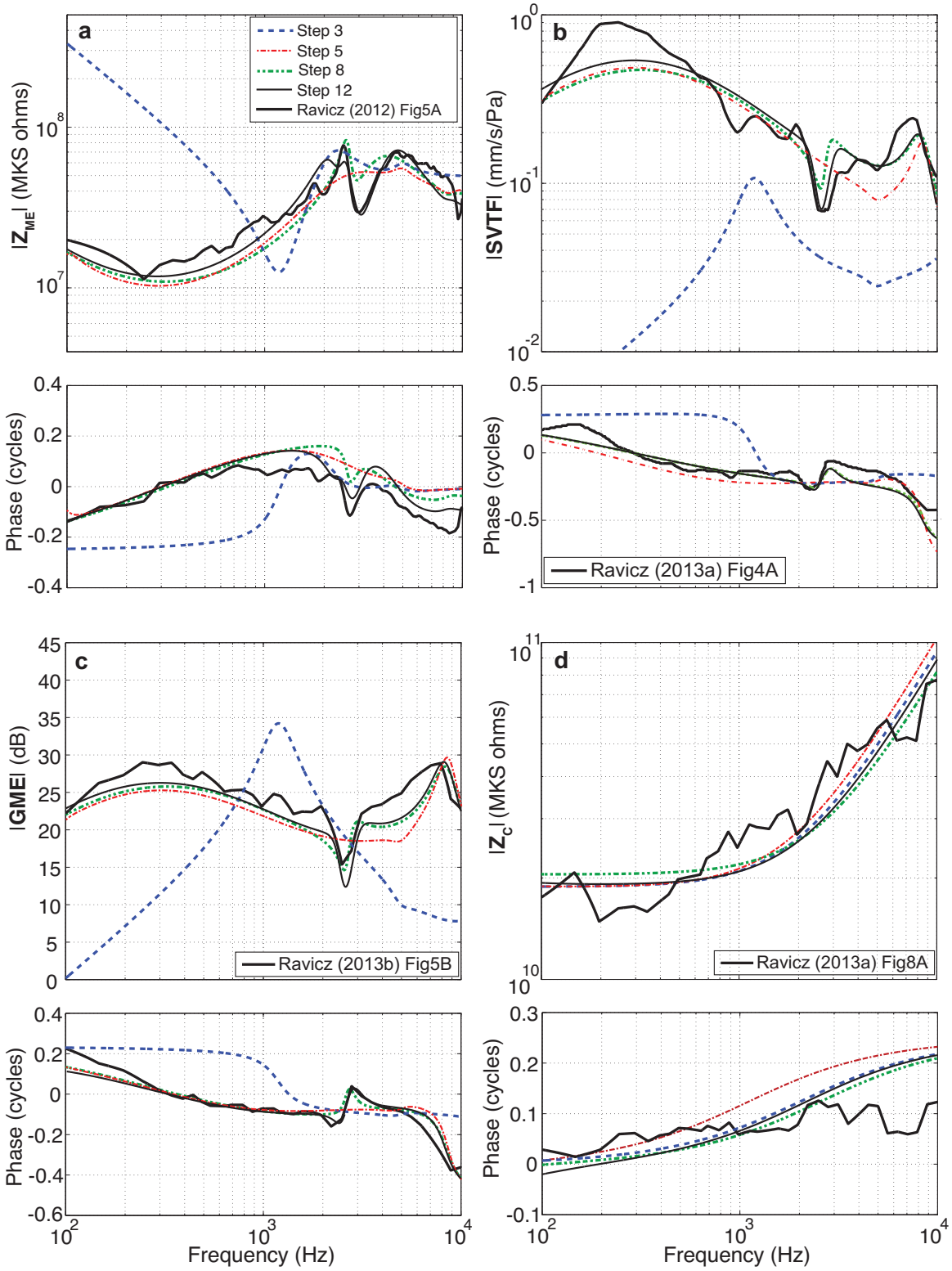

The initial values for the automated optimizations of branch **b**, **c**, and **d** elements were from an optimized version of Zwislocki's (1962) human middle-ear model (Bowers and Rosowski, 2016). Initial values of the cochlear resistive and inertial parameters (in branch **e**) were determined by manual fitting to the cochlear input impedance ($\mathbf{Z_c}$) data (Figure 2.7d). The magnitude of the measured cochlear input impedance (Ravicz and Rosowski, 2013b) is relatively flat up to approximately 600 Hz, after which it increases with increasing frequency. This frequency dependence suggests the series combination of a resistance R_c =1.88e6 kg–s^{-1}m^{-4} and inertance L_c = 1.46e2 kg–m^{-4}, where their values in the model depend on the middle-ear transformer ratios. The resistive effect is assumed to result from the distributed mass and stiffness of the scala fluids and basilar membrane, while the inertance term describes the effect of a mass of fluid between the stapes footplate and the cochlea, as described by Zwislocki (1962). The stapes footplate mass was set to zero, and any inertance in branch **e** determined by the iterative process was attributed to L_c. The annular ligament (C_{al}) and round window (C_{rw}) compliance initial values were defined by the optimized Zwislocki model (Bowers and Rosowski, 2016), as there is no obvious compliance-dominated region in the cochlear input impedance data (Figure 2.7d). The transfer-function predictions produced by these mixed human and chinchilla initial values of the 14 middle-ear elements are illustrated as the Step 3 predictions in Figure 2.7, where the large deviations between the measured and Step 3 model $\mathbf{Z_{ME}}$, **SVTF,** and **GME** are the direct result of the use of human model parameters at this stage.

During the Step 4 and 5 automated fittings, the middle-ear lever ratio L_R and stapes footplate area were fixed at 2.84 and 0.0198 cm^2, respectively (Vrettakos *et al.*, 1988). The effective TM area was constrained to a pars tensa area of 0.70 cm^2 (maximum; Rosowski, 1994), such that A_R

= 35.3. The transformer ratios have a large effect on both the element predictions and the target data (e.g. Equations 2.3, 2.4 and 2.5), and allowing them to vary freely led to highly inconsistent element definitions.

Two sets of 200 computer-automated optimization runs fit the element-dependent transfer functions of the model to the six target system equations, including: the magnitude and phase of the input impedance of the ear ($\mathbf{Z_{ME}}$: Figure 2.7a), the magnitude and phase of the stapes velocity transfer function (**SVTF**: Figure 2.7b), and the magnitude and phase of the cochlear input impedance ($\mathbf{Z_c}$: Figure 2.7d). The measured middle-ear gain (**GME**: Figure 2.7c) was used in the manual fitting procedures, but was excluded from the automatic fitting, as **GME** is directly related to the combination of $\mathbf{Z_c}$ and **SVTF**. The system functions with the model parameters produced by Step 5 (Figure 2.7) were better fits to the target data than the system functions produced by the model with human-based elements (Step 3 in Figure 2.7).

C. Introduction of additional model parameters and manual fitting: Steps 6, 7 and 8

Two shortcomings of the model results of Step 5 are its lack of an explicit stapes inertance, and the poor fit of the model predictions to the prominent notch in the magnitude and phase near 2.7 kHz seen in the middle-ear dependent transfer functions (Figures 2.7a, b, and c). To address the first weakness, Step 6 partitioned the branch **e** inertance into the cochlear inertance L_c and the inertance of the stapes L_{st}, where the latter was initially set by the transformer ratios and a stapes mass of 0.52 mg using Equation 2.9.

The 2.7 kHz notch in the measured magnitude and phase of $\mathbf{Z_{ME}}$, **SVTF**, and **GME** is thought to result from an anti-resonance that results from the parallel combination of the compliances of the middle-ear cavity and inertances associated with sound flow out the cavity

holes (Figure 2.2) that were introduced to observe and manipulate the middle ear (Rosowski *et al.*, 2006). While the model used in Step 5 contains an anatomically defined radiation inertance, that inertance neither produces the notch seen in the data, nor does it account for the fraction of air within the cavities that is accelerated by sound flow out the cavity hole. This additional inertance at the two cavity holes was added in Step 6 by including non-zero L_{rx1} and L_{rx2} into the cavity model with holes in the cavity wall (Figure 2.2).

After introducing these new elements, the model parameters were refined using the GUI to visually fit the model predictions to data from $\mathbf{Z_{ME}}$, **SVTF**, $\mathbf{Z_c}$, and **GME** simultaneously (Step 7). All 26 model parameters introduced by this point (22 circuit-model element values, 2 middle-ear transformer ratios, and the 2 radii of the cavity holes that controlled the radiation impedances) could be varied. In Step 8, repeated sensitivity analyses were performed in which the parameter with the greatest impact was altered to minimize the cost. These cost-guided manual adjustments were repeated until the cost associated with each of the parameters appeared to be minimum. The initial sensitivity analyses of Step 8, which tested the sensitivity of the cost to the parameters defined in Step 7, are illustrated on the left in Figure 2.8. The panels illustrate the fractional change in cost due to ±5%, ±10%, and ±20% variations in individual parameters while all other parameters were held constant. The 26 parameters are arranged along the horizontal axis, where the correspondence between the 26 sensitivity-analysis numbers (SA #) and the parameter names are included in Tables II and III. The existence of decreases in cost associated with changes in the 26 parameters in these panels indicate that Step 7 did not produce an optimum parameter set.

The transfer functions predicted by the parameter set defined by Step 8 show a clear notch near 2.7 kHz in the magnitude and phase of **SVTF**, **GME**, and the phase of $\mathbf{Z_{ME}}$, but the notch in $\mathbf{Z_{ME}}$ magnitude is less well-defined (Figure 2.7a, b, and c).

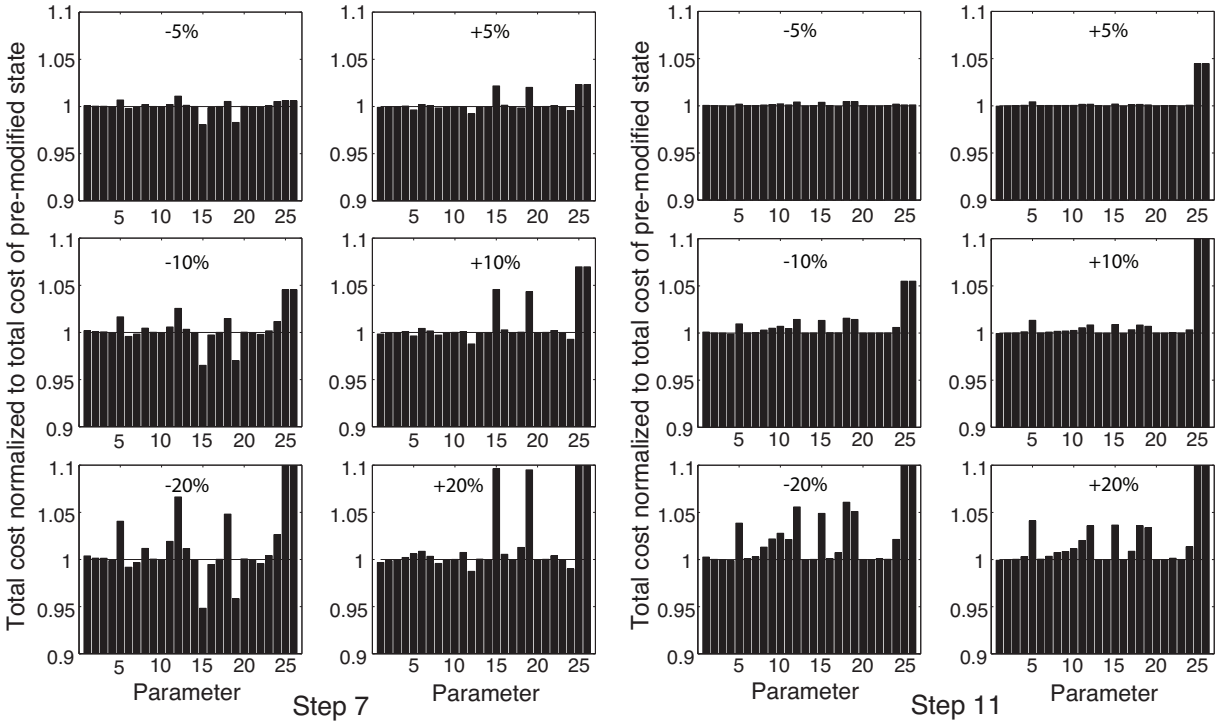

Figure 2.8. Sensitivity analyses.
Parameters were altered ±5%, ±10%, and ±20% and the change in cost was calculated. Shown is the change in cost produced by perturbations in each of the 26 parameters; the SA # of each parameter, which describes its position along the horizontal axes, is in Tables II and III. The sensitivity analysis of resulting parameter set of Step 7 is shown on the left; the deviations from unit values demonstrate some residual non-optimum parameter values. The Step 11 results on the right are consistent with an optimum parameter set, as the perturbations do not decrease the cost. Parameters 25 and 26 are the transformer ratios.

D. Step 9: final automated optimization

Our sensitivity analyses do not guarantee the resulting parameter set is the 'best' fit, therefore additional automated fitting steps were performed. Middle-ear cavity parameters, the middle-ear transformer ratios, and the value of L_{st} were fixed at the values defined in the previous step, and

16 parameters (including L_{rx1} and L_{rx2}) were variable. In Steps 9a-e, a set of automatic fits were performed in which unique, random multiplication factors were applied to the parameter initial values of Step 8. The purpose was two-fold: i) to search in the nearby cost-function space for a lower-cost parameter set, where the resulting parameters are not significantly different from the initial values (small randomization factors), and ii) to search for an equally good, or better set of system parameters that could be significantly different than those determined heretofore (large randomization factors). A multiplication factor having a range of $10^{\pm n}$ was applied to each parameter, where n = 0.25, 0.5, 1, 2, or 3. A set of 200 optimization runs was performed for n = 0.25, while 100 optimization runs were performed for n = 0.5, 1, 2, and 3. The optimization runs of these two steps produced little change in the model parameter set and the predicted transfer functions.

E. Steps 10 and 11: final manual fitting and sensitivity analysis

Step 10 invoked the GUI to adjust any parameters defined by Step 9 that were inconsistent with anatomical values. Specifically, Step 9 defined inertance L_{rx1}, representing the air mass of the superior cavity resulting from the bulla hole, with a mobile volume of air of 23.5 cm^3, which is an order of magnitude greater than the volume of the cavity itself. Manual fitting guided by the dimensions of the cavity resulted in an L_{rx1} with a radius and length consistent with a volume of 0.53 cm^3. This alteration emphasized the 2.7 kHz dip in the magnitude of $\mathbf{Z_{ME}}$. In Step 11, a final sensitivity analysis that investigated alterations in all 26 defined model parameters led to other small adjustments. The final outcome of this analysis was a stable cost value that could only be increased by changes in parameter values (Figure 2.8, right).

F. Step 12: Expansion of cochlear network to better define C_{rw}

By the end of Step 11, most of the parameters of the model were well-defined by a combination of anatomy and the repeated manual and automated optimization steps. An exception was the round-window compliance C_{rw} whose value had little influence on any of the transfer functions used to estimate the model parameter. The lack of a well-defined C_{rw} would interfere with the model's ability to predict the sound pressure in the scala tympani $\mathbf{P'_{ST}}$ (Figure 2.4), a value needed to define the sound pressure across the cochlear partition, a good indicator of the acoustic stimulus to the organ of Corti (Olson, 1999; Nakajima *et al.*, 2009). Direct measurements of $\mathbf{P'_{ST}}$ normalized by sound pressure in the ear canal at the TM do exist (Ravicz and Rosowski, 2013a) and a last optimization run was used with the target data described in Figure 2.9.

An additional complication in modeling $\mathbf{P'_{ST}}$ measurements is that the physical location of these measurements is some small distance from the round window, therefore, we separated out a fraction of the cochlear inertance and resistance (L_c and R_c), determined by the first 11 steps of our fitting procedure, to describe the inertance and resistance (L_{rw} and R_{rw}) of a small column of perilymph between the $\mathbf{P'_{ST}}$ measurement location and the round window (Nedzelnitsky, 1980; Olson, 2001). These terms would also account for any inertance or resistance associated with the RW membrane (Nakajima *et al.*, 2009; Frear *et al.*, 2018).

A single run of the automated fitting procedure was used to determine C_{rw} and what portions of L_c and R_c can be attributed to L_{rw} and R_{rw}; values of L_{rw} and R_{rw} were determined indirectly by optimizing the percent of L_c and R_c, respectively, they were assigned. (Optimization of 3 model parameters.) L_{rw} and R_{rw} were initialized at 10% of the total cochlear inertance and resistance. All parameters of the middle ear, L_{st}, C_{rw}, and transformer ratios were fixed. A single automated

optimization run with thousands of iterations was performed, with initial parameter values taken from Step 11, and with target data of the measured magnitude and phase of $\mathbf{P'_{ST}/P_{TM}}$. Test randomizations of the initial values of the variable parameters did not alter the stable values that resulted from the one optimization run. Figure 2.9 illustrates an excellent fit between the target and the predicted sound-pressure ratios. The transfer functions predicted by the expanded model parameter set produced by Steps 11 and 12 show a good match to much of the data set (Figure 2.7).

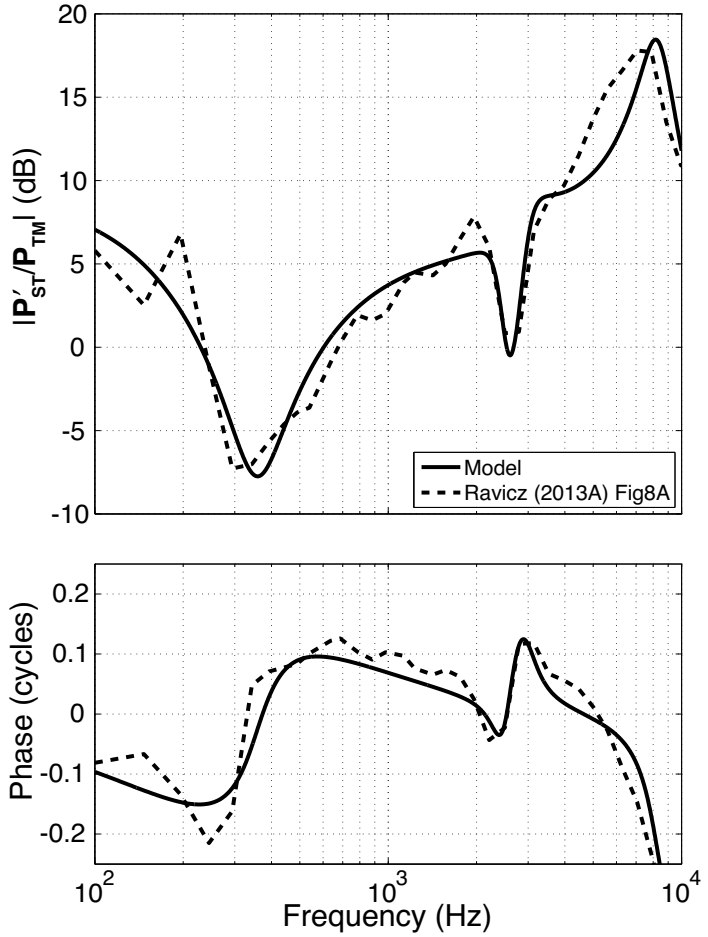

Figure 2.9. Cochlear model fit to intracochlear sound-pressure data.
Fitting the model prediction of $\mathbf{P'_{ST}}$ normalized by ear canal sound pressure, based on the parameter set determined from Step 12. The data is from Ravicz and Rosowski (2013a).

G. Fitness of parameter sets

The total costs associated with the different modeling steps are listed in Table 2.1, and show a general improvement of the fit of the model $\mathbf{Z_{ME}}$, **SVTF**, and $\mathbf{Z_c}$ to the target data (Figure 2.7). The large cost from Step 3 reflects a combination of chinchilla middle-ear cavity and optimized human middle-ear parameters (Bowers and Rosowski, 2016). The first optimizations of the parameters of Figure 2.1 branch **b** through **e**, produce a large reduction in cost (Steps 4 & 5). Cost in general continued to decrease as the original model was refined. The lowest cost was produced by the final manual adjustments and the introduction of a realistic C_{rw} by the additional fitting to the data of Figure 2.9.

Table 2.1. Total cost of the fit after Steps 3 through 12

Output of step	Cost	Output of step	Cost
3	0.703	8	0.0985
4	0.111	9	0.0971
5	0.106	10	0.0900
7	0.113	12	0.0818

H. Final Model parameters

The model parameters that resulted from Step 12 are listed in Table 2.2 (middle-ear cavity) and Table 2.3 (middle ear, cochlea, and transformer ratios). Resistance values have units of kg–$s^{-1}m^{-4}$, inertances have units of kg–m^{-4}, and compliances have units of $m^4s^2kg^{-1}$. The anatomical equivalents of parameters that can be directly related to anatomical features, such as cavity volumes, introduced hole sizes, and ossicular mass, are listed in Table 2.4.

Table 2.2. Middle-ear cavity network parameter values of Step 12 output.
All values are in MKS units. Resistance values have units of kg–$s^{-1}m^{-4}$, inertances have units of kg–m^{-4}, and compliances have units of $m^4s^2kg^{-1}$. SA # is the number assigned to the parameter for the sensitivity analysis. The paired radiation resistances and inertances R_{rx} and L_{rx} are linked in the SA by the radius of the holes.

Parameter	Output of Step 12	SA #
R_a	3.83 e7	1
L_a	3.18 e2	2
C_p	3.62 e-12	3
R_t	1.60 e6	4
C_t	1.04 e-11	5
R_{r1}	8.23 e6	21
L_{r1}	7.39 e2	21
R_{r2}	2.69 e7	22
L_{r2}	1.33 e2	22
L_{rx1}	2.53 e2	23
L_{rx2}	2.59 e2	24

Table 2.3. Middle-ear and cochlea parameter values of Step 12 output.
All values are in MKS units. Resistance values have units of kg–$s^{-1}m^{-4}$, inertances have units of kg–m^{-4}, and compliances have units of $m^4s^2kg^{-1}$. SA # is the number assigned to the parameter for the sensitivity analysis.

Parameter	Output of Step 12	SA #
R_{d1}	8.34 e 6	6
R_{d2}	8.29 e6	5
C_{d1}	1.36 e-12	8
C_{d2}	2.05 e-12	9
L_d	1.02 e3	10
R_o	7.51 e6	11
L_o	1.9 e3	12
C_o	2.07 e-6	13
R_s	3.18 e5	14
C_s	1.70 e-12	15
L_{st}	17.5	16
C_{al}	1.10 e-10	17
R_c	3.15 e6	18
L_c	2.27 e2	19
C_{rw}	2.89 e-9	20
R_{rw}	6.24e4	NA
L_{rw}	68.8	NA
TM area	0.668 cm^2	25

Lever	2.83	26
FP Area	0.0198 cm^2	

Table 2.4. Anatomical equivalents for parameters of Step 12 output.
Anatomical equivalents of middle-ear cavity parameter values are listed below, as well the effective malleus-incus complex mass and the mass of the stapes.

Anatomy	**Output of Step 12**
Tympanic cavity volume	1.47 cm^3
Tympanic cavity hole area	0.490 cm^2
Superior cavity volume	0.513 cm^3
Superior cavity hole area	0.150 cm^2
Malleus-incus mass	7.56 mg
Stapes mass	0.616 mg
Volume of L_{rx1}	0.531 cm^3
Volume of L_{rx2}	0.0509 cm^3

IV. Discussion

A. Degree of fit of the different parameter sets

Outputs from Step 3 in Figure 2.7 indicate that constraining the middle-ear cavity based on middle-ear impedance data and initializing the cochlear parameters based on cochlear input impedance data is not sufficient for producing a good fit to middle-ear transfer-function data when the remaining parameters are set to values determined for the human middle ear.

Outputs of the first automated fitting steps (Step 5 in Figure 2.7) are already quite similar in magnitude and phase to the experimental data (Ravicz and Rosowski, 2012; 2013a; b), with a few exceptions: i) The notches seen in **GME** and **SVTF** at approximately 2.7 kHz are not captured, ii) the model does not capture the two distinct $|\mathbf{Z_{ME}}|$ maxima at approximately 1.3 kHz and 4.2 kHz (a broad peak is predicted), iii) the model underpredicts middle-ear transfer function magnitudes at frequencies below 600 Hz, and iv) the model does not fit the angle of $\mathbf{Z_c}$ well at frequencies above 1 kHz.

The addition of L_{rx1} and L_{rx2} in manual fitting Steps 7 and 8 reproduces the 2.7 kHz notch in the middle-ear transfer functions. The further addition of an inertance to model the stapes mass shifts the high-frequency maximums of |**SVTF**| and |**GME**| to a lower frequency, however, this is not obvious in Step 8, as the effect of the stapes addition was balanced by a decrease in cochlear inertance L_c.

As with earlier steps, the model of Step 12 underpredicts the magnitude of **SVTF** and **GME** at frequencies below 600 Hz, with the largest discrepancy located about the peaks, between 200-300 Hz and at 300 Hz, respectively. The magnitude of these transfer functions are directly related to the middle-ear transformer ratios, and the resistive component of the cochlea. It is unclear as to why the automated-optimization method was unsuccessful in generating a parameter set that better fits the magnitude of **SVTF** at lower frequencies (the cost of the automated process did not account for the fit to **GME**), but it may be due to the fixing of the middle-ear transformer ratios. During the manual fitting procedure, although the transformer ratios could be adjusted, it was not possible to improve the fit to the low-frequency magnitudes of **SVTF** and **GME** simultaneously. The final model under predicts both, as altering the transformer ratios to better fit one transfer function magnitude caused a worse fit to the other.

There is also a tradeoff in the model fit to the magnitude and angle of the cochlear input impedance above a few kHz. The series combination of R_c and L_c can be set to produce a reasonable fit to the magnitude of $\mathbf{Z_c}$ (as in Figure 2.7d), but at the cost of overestimating the angle of $\mathbf{Z_c}$ above 3 kHz. A reduction in L_c can produce a better fit to the $\mathbf{Z_c}$ angle, but will lead to a decrease in the fit of the magnitude.

Figure 2.10. Outputs of complete air-conduction model.
Chinchilla ME transfer functions with the middle ear closed or with two holes in the cavities. Shown are magnitude and phase of model outputs (thick solid line) of Step 12 and experimental data (dashed line) of (a) $\mathbf{Z_{ME}}$, (b) **SVTF**, (c) **GME**, and (d) $\mathbf{Z_c}$. Data are from Ravicz and Rosowski (2012; 2013a; b). In (a-c), the model outputs of Step 12 with the middle-ear cavity parameters set to the closed-bulla (no hole) condition (thin solid line) are shown as a comparison of middle-ear conditions.

Figure 2.10 (continued)

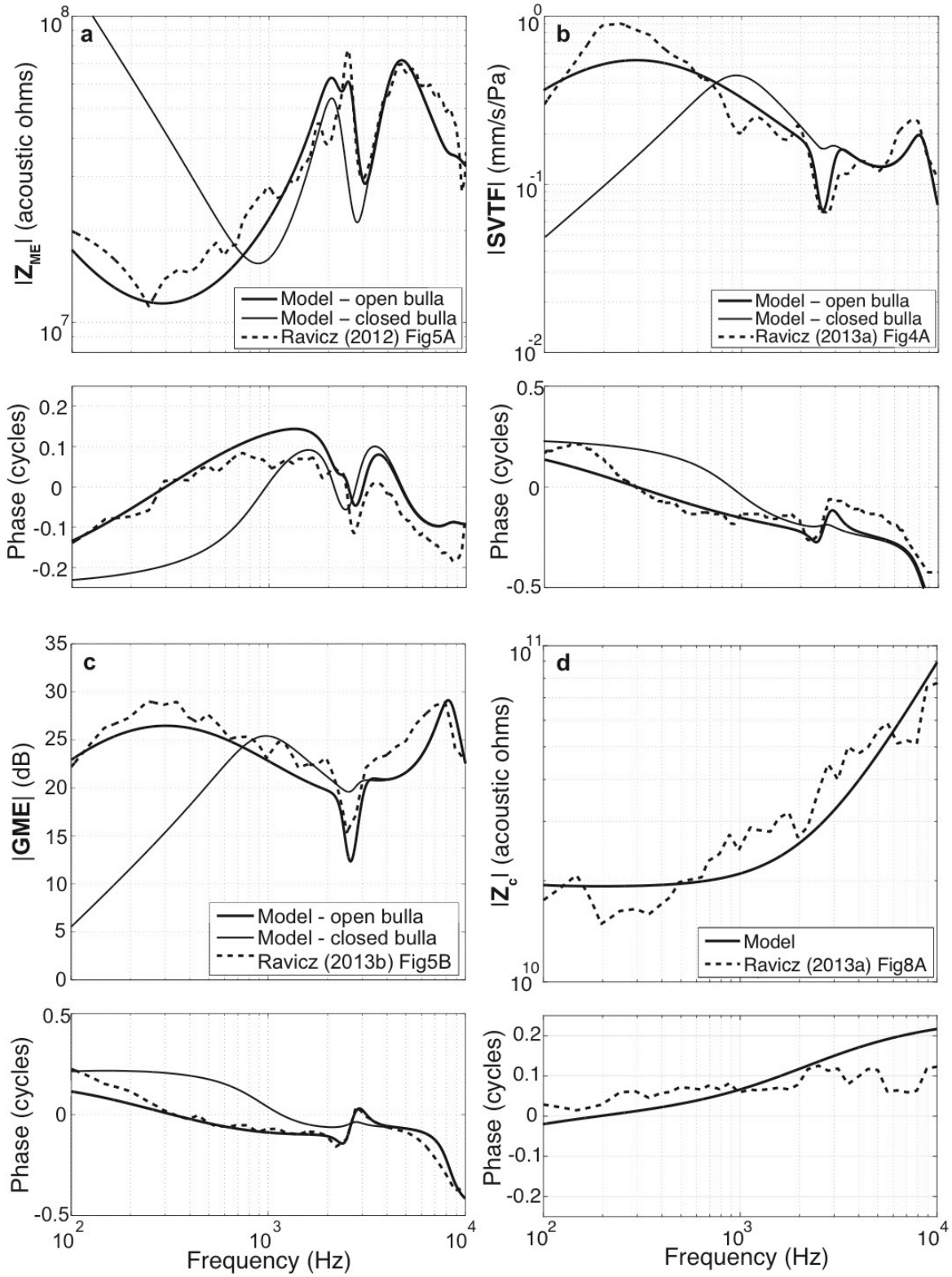

B. Comparison of model parameters to known structures

Compliance of the total middle-ear cavity volume is described in the model by the parallel compliances of C_t and C_p with volumes of 1.47 cm^3 and 0.513 cm^3, respectively, resulting in a total middle-ear cavity volume of approximately 1.98 cm^3. Average chinchilla middle-ear volumes of (1.2, 1.5, 2.0, 2.2, 2.8) cm^3 have been cited (von Bismarck, 1967; Drescher and Eldredge, 1974; Teas and Nielsen, 1975; Vrettakos *et al.*, 1988; Rosowski *et al.*, 2006). The volume of the superior cavity was measured in two chinchillas (one ear each). The individual measurements were 0.527 cm^3 and 0.680 cm^3. Our fitting results that describe the ratio of the two cavity volumes A_V as 0.35 and the sum of the volumes as 2 cm^3 are roughly consistent with this anatomical observation $A_V = V_p/V_t = 0.6/(2\text{-}0.6) = 0.42$.

From Equation 2.8, the inertance of the coupled TM, malleus, and incus, L_o is related to the effective ossicular mass M_o, where $M_o = L_o(A_{TM})^2$ and A_{TM} is the tympanic-membrane area. With $A_{TM} = 0.60$ cm^2 and $L_o = 1.9\text{x}10^3$ kg–m^{-4}, the predicted malleus-incus mass from Step 12 is 7.56 mg. Thirteen chinchilla malleus-incus complexes (with intact manubrium) from experiments were stored in saline and later weighed. The average mass was 12.9 mg. Since this malleus-incus mass (along with the mass of the coupled TM) rotates around supporting ossicular ligaments near its center of gravity (Sim *et al.*, 2007), the calculated M_o is reasonable.

The inertance representing the stapes mass was added to the circuit in Step 6 with a value of 13 kg–m^{-4}, which is equivalent to a stapes mass of 0.52 mg with $L_R = 2.86$ and $A_{TM} = 0.70$ cm^2 (Equation 2.9). This inertance was modified in Step 8 to a value of 17.5 kg–m^{-4} (equivalent to a mass of 0.65 mg) and remained fixed in Step 9. Because Step 11 included adjustments of A_{TM}, L_R, and L_{st}, the final stapes mass became 0.62 mg, which is 55% greater than the 0.4 mg measured by Vrettakos *et al*. (1988).

The area of the tympanic cavity hole was also modified during the final manual fitting process (Step 11) from 0.190 cm^2, based on the measured tympanic cavity hole of a single representative chinchilla ear, to 0.150 cm^2. This is a reasonable change given the amount of variation expected in cavity hole size across experiments.

The inertance terms in the cochlear input impedance can be described in terms of quantities of water-like fluid. Zwislocki (1962) suggested L_c corresponded to a small column of fluid between the footplate and the cochlear partition, and Nedzelnitsky (1980) and Olson (2001) suggest that some component of L_{rw} may be attributed to a small column of RW-entrained fluid positioned between the $\mathbf{P'_{ST}}$ measurement site and the RW. Using the model transformer ratio, we can convert the acoustic inertances seen at the TM to those that appear at the footplate. These acoustic inertances can then be converted to mechanical masses by multiplying by the square of the area of the footplate (Zwislocki, 1962). After these transformations, the masses associated with the optimized L_c and L_{rw} are 8.11 mg and 2.46 mg, respectively. Assuming these correspond to volumes of water-like fluid, the volumes are 8.11 and 2.46 microliters, respectively. If we assume these volumes are cylindrical with a cross-section equal to that of the footplate area, ~2 mm^2, the length of the cylinders are 4.05 and 1.23 mm, respectively. The first is about twice the distance between the footplate and the cochlear partition in chinchilla, while the second is a reasonable estimate of the distance between the $\mathbf{P'_{ST}}$ measurement site and the RW.

C. Effect of closing and opening the cavity on middle-ear sound transmission

While we have fit the middle-ear model to data gathered with the middle-ear air cavity open to enable ossicular manipulations and measurements, the air cavity is closed in the intact animal. Closing the chinchilla air cavity is expected to have two effects (Rosowski *et al.*, 2006): i) an increase in the stiffness of the ear at low frequencies that results in an increase in the magnitude of the middle-ear impedance at low-frequencies, and a concomitant decrease in the magnitude of **SVTF** and **GME**, as sound transmission to the inner ear is reduced; ii) a change in the frequency and depth of the near 2.7 kHz notches in middle-ear transmission that result from an interaction of the cavity compliance and the inertance of the introduced holes.

Closing the cavity holes in our model by replacing the cavity model of Figure 2.2 with that of Figure 2.1 produces such effect, as observed in Figure 2.10. In that figure, we compare the model predictions based on the parameter values from Step 12, with the open cavity data, and model predictions made after closing the model's cavities as described above. The model changes are consistent with both an increase in the stiffness of the ear that increases $|\mathbf{Z_{ME}}|$ and reduces $|\mathbf{SVTF}|$ and $|\mathbf{GME}|$ at frequencies below 800 Hz, alters the frequency and depth of the mid-frequency notches in $\mathbf{Z_{ME}}$ magnitude and phase, and nearly eliminates the mid-frequency notches observed in **SVTF** and **GME** magnitude and phase.

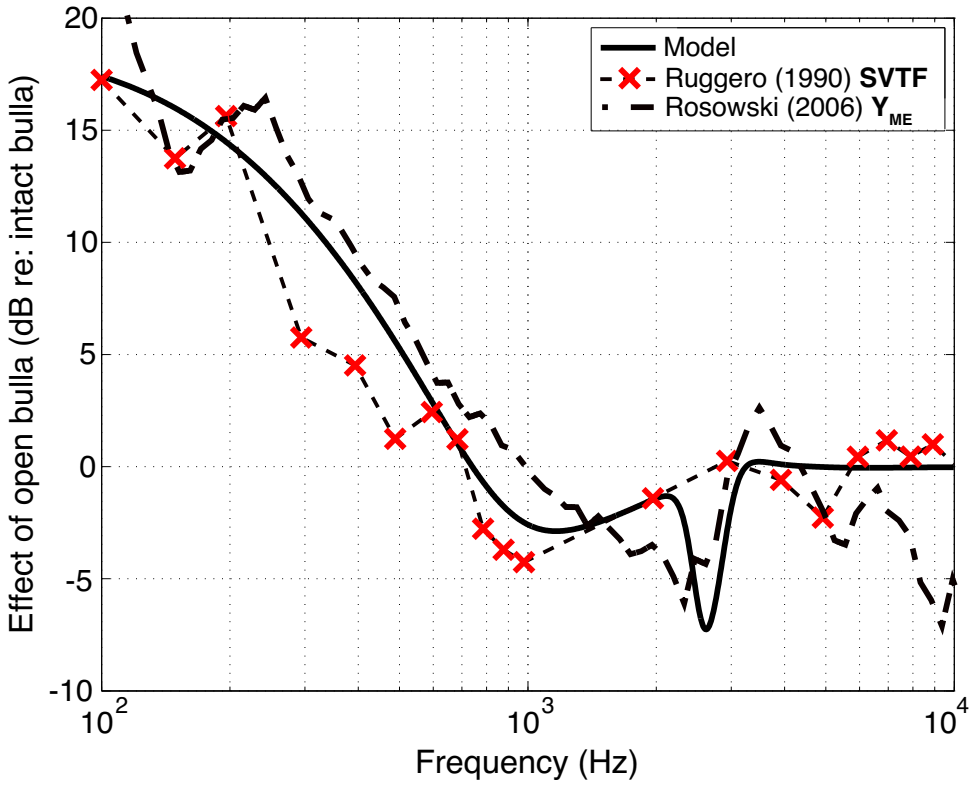

Figure 2.11. The effect of opening the cavity on middle-ear transmission.
The dB difference between the intact and opened cavities in either |**SVTF**| or $|\mathbf{Y}_{ME}|$. The effect in the model is shown as a solid line (Step 12), the effect measured by Rosowski *et al*. (2006) is dash-dotted line, and the effect measured by Ruggero *et al*. (1990) is shown as a dashed line. The × markers show the frequency resolution in the Ruggero data.

To further compare the cavities contribution to middle-ear function, we compare the model predictions to measurements of the effect of opening holes in the walls of the chinchilla middle-ear cavity, which has been evaluated by multiple investigators (Dallos, 1970; Drescher and Eldredge, 1974; Teas and Nielsen, 1975; Ruggero *et al.*, 1990; Rosowski *et al.*, 2006). In all of these studies, at frequencies below 0.7 to 1 kHz the effect of the opening the middle ear was an increase in the magnitude of middle-ear sound transmission by as much as 20 dB at 100 Hz. Figure 2.11 shows the effect of opening cavity holes on the magnitude of the model **SVTF** along

with the **SVTF** data of Ruggero *et al*. (1990) and $\mathbf{Y_{ME}}$ ($1/\mathbf{Z_{ME}}$) of Rosowski *et al*. (2006). (The **Y** ratio is computed from $\mathbf{Y_{ME}}$ measured with middle-ear cavity holes similar to those in the Ravicz studies, set 2 of Figure 2.12 of Rosowski *et al*., divided by the mean admittance measured with intact but vented middle-ear cavities, Figure 3A of that paper.) There is much in common between the model prediction and the data sets, but some differences. In the 2 to 3 kHz region, the model predicts opening the cavities introduces a narrow notch (a narrow-band decrease) in the magnitude. This notch is not seen in the Ruggero *et al*. data, which did not have a high enough frequency resolution to see such a notch, while in the Rosowski *et al*. data, which is based on mean data, the notch is somewhat spread in the frequency domain.

Such a notch, and an accompanying rapid change in phase angle is a common observation of the effect of placing holes in the cavity wall (Guinan and Peake, 1967; Ravicz *et al.*, 1992; Rosowski *et al.*, 2006). In chinchilla, the frequency of the notch has been demonstrated to depend on the size of the cavity holes (Rosowski *et al.*, 2006). The $\mathbf{Z_{ME}}$, **SVTF**, and **GME** data and fits in Figure 2.10 demonstrate the model was able to match the magnitude notch and phase change after the introduction of the additional hole associated inertances L_{rx1} and L_{rx2} in Step 6.

The dependence of the notch on the addition of L_{rx1} and L_{rx2} points out that simply including anatomically correct cavity hole radiation impedances in the model did not produce the notch. We associate the necessary inertances L_{rx1} and L_{rx2} with some fraction of the formerly-enclosed air volumes being accelerated by sound as the sound particles move in and out of the holes. If we assume these air columns have a cross-sectional area equal to the area of the opening of the middle-ear cavities A_h, the volume of the accelerated air columns can be calculated by the following equation:

$$V_{lrx1,2} = \frac{L_{rx1,2} A_h^2}{\rho_{air}} \quad (2.19)$$

.

These hypothetical accelerated air volumes after the manual fitting of Step 11 are 0.531 cm^3 for L_{rx1} and 0.0509 cm^3 for L_{rx2}. These volumes are about 1/3 of the C_t volume and about a tenth of the C_p volume. Our fitting procedure has not reduced the compliant air volumes by these fractions.

D. Possible additional complexity needed to model the low-frequency cochlea

The lumped-element model of the cochlea used in the fitting procedure is based directly on the simple cochlear model proposed by Zwislocki (1962) of a series resistance R_c and inertance L_c. Such a model does a good job of matching the load the cochlea places on the middle ear at frequencies between 0.1 and 3 kHz (Figure 2.7d). However, there are cochlear structures with effects not included in our model that may contribute to the cochlear load on sound transmission, in particular the helicotrema, which is thought to affect the cochlear input impedance at low frequencies (Dallos, 1970; Lynch *et al.*, 1982; Motallebzadeh *et al.*, 2017b). Dallos (1970) attributed variations in the frequency dependence of the cochlear microphonic in chinchillas that occurred at frequencies below 0.3 kHz to the helicotrema. Consistent with such an effect, irregularities in the frequency-dependence of the chinchilla middle-ear impedance were observed in the same low-frequency range (Rosowski *et al.*, 2006), and these irregularities were decreased by removal of the cochlear load. It is possible that the lack of a helicotrema in our model contributes to the model's failure to precisely fit both $\mathbf{Z_{ME}}$ and **SVTF** data at frequencies of 0.3 kHz and below. The significance of such low-frequency effects in our future bone-conduction model is reduced by the limited bandwidth, 0.2 to 8 kHz, of our bone-conduction stimuli.

Step 12 was performed to determine the round-window compliance, as automated optimizations did not predict a value that contributed to the resulting transfer function and impedance outputs in any way. The final value of C_{rw}, although being important for fitting the model to the normalized scala tympani sound pressure measurements, had little impact on the cochlear input impedance and middle-ear transfer functions.

E. Comparison to the model of Lemons and Meaud (2016)

As noted above, Lemons and Meaud (2016) used the Songer and Rosowski (2007b) data to produce circuit-element and two-port transmission-matrix descriptions of the chinchilla middle ear that they modified to investigate inter-species difference in middle-ear function. A significant difference between our and the Lemons and Meaud approach is that they chose significantly different transformer values (TM to footplate area ratios A_R = 0.8/0.0198, and malleus-incus lever ratio L_R = *3.7*) that they fixed before fitting the model. While we fixed our model representation of the footplate area to the same value (0.0198 cm^2), we initiated L_R = 2.86 and A_{TM} = 0.7 cm^2 with different values from the literature, and we used sensitivity analyses to direct manual adjustments in L_R and A_{TM}. As noted previously, the cost of the different model fits was quite sensitive to L_R and A_{TM}, and the fitting procedure led to downward adjustments in both of these quantities. The result of this different approach is a sizeable difference between the overall transformer ratio of our ((A_{TM}/A_{FP}) x L_R = 78.8) and the Lemons and Meaud models ((A_{TM}/A_{FP}) x L_R = 148). This difference, coupled with differences in model structure, make it difficult to compare the element values of the two models.

F. Model limitations and weaknesses

1. Cochlear network

Much of the finer frequency dependence in the experimental $\mathbf{Z_c}$ data (Ravicz and Rosowski, 2013b) is not captured by the model, nor is the less than quarter cycle phase at higher frequencies, as these behaviors cannot be reproduced by a simple series RLC network. Some of the complexity in the data may be associated with the shunting of volume velocity through additional sound pathways such as the cochlear and vestibular aqueducts. Such additional complexity in $\mathbf{Z_c}$ could explain similar differences between the measured and the model-predicted |**GME**| and |**SVTF**| (Ravicz and Rosowski, 2013a; b). A more-complicated representation of the cochlea will be necessary to model the mechanisms of the inner-ear bone-conduction source (Stenfelt, 2016).

2. 3D motion of ossicular chain

Our lumped-element model does not account for observations of complex 3D motion of the ossicular chain (Decraemer *et al.*, 1994). This limitation is shared by the experiments of Ravicz and Rosowski (2013a; b), in which the stapes velocity was measured only in the direction normal to the stapes footplate. In human, over the range of 0.5 to 8 kHz, rocking motions of the stapes are on the same order of magnitude as its linear motion along an axis perpendicular to the stapes footplate (Sim *et al.*, 2010). Puria and Steele (2010) suggest that in larger mammals, such as in human and cat, asymmetry in TM area with respect to the axis defined by the length of the manubrium may cause rocking motion of the ossicles. This differs from smaller mammals such as the guinea pig and chinchilla, in which there is symmetry of the TM area about this same axis. It may then be the case that complex motions of the ossicular chain of the chinchilla are limited to complex modes of motion of the TM resulting from other asymmetries in the membrane.

V. Conclusion

A relatively simple circuit of the middle ear and cochlea that is developed from air-conduction hearing data will serve as the basis for a model for bone-conduction hearing in chinchilla. The model was developed by fitting various model outputs to middle-ear input impedance, middle-ear cavity and transfer-function data, and cochlear input impedance. Parameters that are direct circuit analogs of anatomical features served as model constraints. The model captures the salient features of the data and predicts the effects of middle-ear cavity holes. The greatest difference between the model output and experimental data is in the cochlear input impedance.

Automatic fitting procedures were used that led to decreases in the squared difference (the cost) between target data and model predictions. A GUI also allowed manual fitting that was guided by the quantified total cost of the model fit to the experimental data, and sensitivity analyses that quantified the effect of parameter changes on cost. In some cases, automatic fitting produced erratic results, such as when the stapes mass, transformer ratios of the middle ear, and the annular ligament compliance were allowed to vary. The final parameter values make sense both anatomically and mechanically and are in general agreement with those found in literature. Our model fits middle-ear transfer functions and impedances (Ravicz and Rosowski, 2012; 2013a; b) at frequencies below 10 kHz. No attempt was made to fit to higher-frequency data; we expect phase discrepancies above 10 kHz because our model does not contain any explicit delay term, and such delays have been observed in chinchilla middle-ear data at higher frequencies (Ravicz and Rosowski, 2013a; b).

CHAPTER 3. Characterization of chinchilla external-ear source of bone-conducted sound

Abstract. We are adapting a model for air-conducted sound in chinchilla to include multiple data-defined bone-conduction sources. Here, the magnitude and phase of two hypothetical vibration-driven external-ear bone-conduction sources (EEBCs) are estimated using ear-canal sound-pressure (ECSP) measurements, during BC stimulation. The measurements were made in the normal ear and after external and middle-ear modifications. The EEBC estimates required model estimates of the acoustic impedance of (a) the middle ear in the different measurement states, and (b) the reverse ear-canal impedance in the open and occluded states. Results suggest: 1) motion of both the cartilaginous and bony portions of the ear canal generate BC-induced ECSP; 2) ECSP measured during bone-conduction stimulation is dominated by the EEBC as manipulations of the ossicular chain (i.e. ossicular fixation and ISJ interruption) that effectively isolate the ear canal from the middle and inner ear, do not greatly affect the estimates of the EEBC magnitudes; 3) The relative motion of the jaw with respect to the ear canal has little effect on the measured ECSP. Compound action potentials (CAP) measurements before and after various manipulations of the ear, which quantify the effect of the EEBCs on the inner ear's response to bone-conduction stimulation, suggest they contribute to hearing across a large frequency range when the ear canal is both occluded and open.

I. Introduction

Bone-conduction (BC) hearing, elicited by sound pressure transmitted to the inner ear by skull vibration, is used clinically to diagnose and treat middle-ear disease. Medical BC devices work by bypassing the pathologic external and/or middle ear (with pathologies produced by ear-canal atresia, otosclerosis, ossicular discontinuity, or other disorders) allowing the inner-ear mechanisms of BC to stimulate the organ of Corti. The mechanisms of BC are not fully understood, as skull vibrations travel along multiple pathways to the inner ear. Here we examine one BC pathway: the external-ear component of BC hearing that is related to sound pressure produced in the ear canal by vibratory stimuli. The external-ear pathway is hypothesized to result from the oscillating compression and expansion of the ear-canal walls that perturbs the ear-canal volume and generates a sound pressure within the canal. We model these vibration-induced changes in the ear-canal volume by a pair of ideal volume-velocity sources, where the magnitude of the generated sound pressure depends on the complex magnitude of the vibration-related sources as well as the acoustic impedances of the middle-ear and the air in the ear canal. In the normal ear, this sound pressure is transmitted to the inner ear by way of the ossicular chain, following the same pathway used to conduct air-conducted sound to the inner ear.

In addition to the external-ear bone-conduction sources (EEBCs), other BC sources transmit sound energy to the inner ear: the middle-ear BC source is associated with relative motions between the stapes and the cochlea that result from ossicular inertia; inner-ear source mechanisms include fluid (perilymph) inertia, cochlear-bone compression and expansion (Stenfelt and Goode, 2005), and sound pressures produced within the cranium that are transmitted to the inner ear via “third-window” pathways, including the cochlear and vestibular aqueducts (Freeman *et al.*, 2000), and perineural and perivascular channels.

The EEBCs are commonly associated with the *occlusion effect,* the expected increase in perceived bone-conduction sound when the external ear canal is occluded, specifically at low frequencies. A long-standing theory, developed by Mach (1863), was that the low impedance of the open ear canal allows sound energy, which enters the cochlea via other routes, to escape to the outside world via the ear canal. Under this hypothesis, occlusion of the ear canal increased ECSP due to the increased impedance loading the sources within the inner ear. This idea was challenged by experiments which compared bone-conduction evoked ECSPs in the normal ear and after the tympanic membrane (TM) was resected. Resection of the TM should cause a decrease in the ECSP if the sound energy originates within the inner-ear, but this was not the case (Tonndorf, 1976). In 1930, several scientists independently formed the idea that occluding the ear simply eliminates air-borne masking noise, effectively increasing the sound perceived through bone-conduction stimulation (Hallpike, 1929; Dean, 1930; Pohlmann, 1930). It was later shown that this could not be the only mechanism, as the cochlear microphonic increases along with the perceived loudness when the ear canal is occluded (Tonndorf, 1976). The occlusion effect has continued to be studied by others looking at changes in ECSP (Fagelson and Martin, 1994; Stenfelt *et al.*, 2003), and/or changes in hearing thresholds (Edgerton and Klodd, 1976; Berger and Kerivan, 1983). It is now commonly understood that normally a significant fraction of the sound energy generated within the ear canal by ECBC sources exits the ear via the low-impedance open ear canal, and occlusion of the ear canal, forces more sound energy into the middle ear.

Békésy (1932) first reasoned from experimental observations that only the cartilaginous portion of the ear canal is capable of sufficiently compressing the air within the canal, producing an acoustic pressure, and that if the occlusion were inserted deep to the bony canal, no noticeable

increase in sound pressure would result. Moreover, Békésy concluded that any notable sound pressure generated within the occluded ear canal would be due to relative motion of the mandibular joint (which is located just inferior to the cartilaginous ear canal) with respect to the canal, as the mandible is not fixed to the skull. Contribution of jaw motion to BC hearing has been supported subjectively by changes in bone-conduction hearing when the jaw is clenched and relaxed (Littler *et al.*, 1952). Further support for the importance of the mandible comes from a study in which BC-induced ECSPs were measured in normal subjects and subjects who underwent a hemimandibulectomy (a portion of the mandible is removed) (Howell and Williams, 1989). The occlusion effect at the side of resection was diminished with respect to the effect measured in the ear canal of the contralateral side. However, Allen and Fernandez (1960) reported that in two patients who underwent unilateral mandibular resection, an occlusion effect was recorded, at similar magnitudes, in both ears. Stenfelt and colleagues (Stenfelt *et al.*, 2003) found that resection of the lower jaw in cadaver heads did not significantly alter the measured ECSP.

Stenfelt and colleagues (2003) investigated the EEBCs by looking at the BC-induced ECSP and umbo velocity in the cadaveric human ear. In addition, they investigated potential contribution of the inner- and middle-ear mechanisms to BC-induced ECSP by quantifying the ECSP that results from TM motions produced by driving the ossicles in reverse (driving the vestibular side of stapes footplate). Their results suggest that in humans a) the occlusion effect is as great as 20 dB at frequencies below 2 kHz, b) the occlusion effect is diminished but not eliminated by removal of the cartilaginous portion of the ear canal, c) relative motion of the jaw with respect to the ear canal does not contribute significantly to the BC-induced ECSP, and d) motion of the TM contributes little to BC-induced ECSP. Also, comparisons of the ratio of umbo

velocity to ECSP—during BC and AC stimulation suggested, e) BC hearing in humans is dominated by the EEBC at frequencies between 0.4 and 1.2 kHz when the ear canal is occluded.

The mechanisms of bone conduction and its use in diagnosing the pathologic ear have been studied in various animals, including the cat (Tonndorf *et al.*, 1961; Marres, 1965), guinea pig (Legouix, 1959; Kanagawa and Tokimoto, 1982), mouse (Chhan *et al.*, 2017), and chinchilla (Songer *et al.*, 2003; Chhan *et al.*, 2013; Chhan *et al.*, 2016b). The choice of a non-human animal model in the current study was motivated by the ability to record acoustic, mechanical, and neural responses in normal and manipulated ears; procedures that are not readily performed in live humans. Furthermore, similarities to humans in the frequency range of hearing and in the dimensions of the chinchilla middle and inner-ear structures makes this rodent especially well-suited for study, while one major difference, the lack of mastoid air-cells in chinchilla, allows for greater intraspecies consistency across measurements. A potential confounding factor in relating chinchilla-derived measurements to human is that the cartilaginous portion of the chinchilla ear canal projects from the skull and its muscle layers and is not contained within the soft-tissues of the head as it is in human.

The mechanisms of the EEBC and the occlusion effect (Schroeter and Poesselt, 1986; Stenfelt and Reinfeldt, 2007), and the contribution of the EEBC to BC-hearing (Stenfelt, 2016) in human have been studied using a lumped-element circuit model approach. The latter model incorporates a 2-source representation of the EEBC to account for the distributed nature of sources along the ear canal. The effect of static pressure on transmission of BC-induced ECSP to the inner ear has been studied with a finite-element model (Homma *et al.*, 2010).

Here, the magnitude and phase of the EEBCs are estimated from new ear-canal sound-pressure measurements together with model impedance predictions. The predicted impedances of

the middle ear and cochlea come from a chinchilla AC circuit model (Bowers et al. 2019). The ear canal is modeled by a structure-based concatenation of finite conical horns, and its acoustic impedance is derived from a series of transmission matrices representing these conical segments (Beranek and Mellow 2012). The influence of jaw motion on the BC-induced ECSP is investigated, as well as the potential contribution of non-external ear BC sources to the sound pressures generated within the ear canal. The contribution of the EEBC to BC hearing is estimated by comparison of compound action potentials (CAPs) at threshold, during BC stimulation, in the normal and manipulated chinchilla ear.

II. Methods

A. Preparation

All experiments were performed in accordance with guidelines published by the U.S. Public Health Service and were approved by Massachusetts Eye and Ear Institutional Animal Care and Use Committee. Sixteen live chinchillas were used in this study. In some experiments in which only mechanical and/or acoustic measurements were performed (neural responses were not measured), cadaveric chinchilla heads were used (n = 14, most used the ear that was unused during the live animal experiments). In all experiments in which electrophysiological potentials were measured, the animals were alive and deeply anesthetized; initial doses of 0.05 mg/kg of atropine and 3 mg/kg of Xylazine (subdermally), and 25 mg/kg of ketamine (intramuscularly) were administered, and supplemental doses of either ketamine or a mixture of ketamine and Xylazine (intramuscularly) were administered as needed. The animal's body temperature was regulated at a normal level (38°C ± 1°) and its heart rate was monitored. A tracheotomy was performed and a tracheal cannula inserted. Holes were made in the superior and posterior bullae

(Figure 3.1A). The tensor-tympani tendon was cut by way of the superior bulla hole. Through the posterior bulla hole, a portion of a bony wall that follows the bone covering the tympanic segment of the facial nerve, was removed to provide a view of the incudostapedial joint (ISJ), while making sure not to remove bone to which the stapedius muscle was connected (Figure 3.2). A hole was placed in the bony portion of the external-ear canal near the TM. A probe-microphone positioning sleeve was inserted into the hole so that the medial end of the inserted probe was approximately 5 mm away the umbo and 1mm below the superior portion of the tympanic ring (Figure 3.1A). Due to the tented shape of the TM and the constrained orientation of the probe-tube microphone, the microphone was closer to the perimeter of the TM than to the umbo. The average distance from microphone to TM was about 1.7 mm.

A 3 mm diameter hole was drilled into the top of the skull down to the dura mater. A stainless-steel mount designed for a bone-anchored hearing aid (BAHA) was fitted approximately 1 mm into the hole and was fixed in place with dental cement (Figure 3.1B).

B. Data acquisition

1. Stimuli and measured responses

The vibratory stimuli used for the ECSP measurements consisted of a series of pure sinusoids ranging from 200 Hz to 10 kHz at logarithmically-spaced frequencies with a 24 frequencies/octave spacing. The stimulus waveforms were generated by a Hewlett Packard 33120A waveform generator. The output of the waveform generator was conditioned by a TDT System 3 attenuator, Krohn-Hite 3901 filter, and a Crest 1001A power amplifier, before driving the BAHA attached to the chinchilla skull. One of two BAHAs were attached to the skull-mount; either a BAHA© 3 (BP100) or a BAHA© 5 SuperPower. The skull-motions produced by these

devices were measured with laser doppler vibrometry; the measured head velocity was used to normalize all other measured quantities.

Electric responses to pure tone stimulation were averaged for periods of 0.25 (typical) to 1 second, depending on the strength of the response signals. Fourier analysis of the average tone data via a custom software package (the *High-frequency Measurement System*, written by author MER in *LabView*®) allowed the definition of the magnitude and phase of the stimulus-frequency component and an estimate of measurement noise from frequency components near the stimulus frequency. The velocity and sound pressure data presented in this report include only responses that met or exceeded a 10 dB signal-to-noise criterion; signal was compared to noise floor at ± 3 frequencies points about the frequency of interest.

2. Skull velocity

Skull velocity was measured using a Polytec CLV1000 laser Doppler vibrometer (LDV). The LDV measured the vibration-induced velocity of the outer surface of a portion of the superior bulla (along a bulla septum when possible) and was most sensitive to motion in the rostral-caudal direction (Figure 3.1B). Skull velocities induced by BC stimulation ranged from approximately 0.1 nm/s to 1 mm/s.

3. Ear canal sound pressure

Ear canal sound pressures (ECSPs) within 1.7 mm of the TM ($\mathbf{P_{TM}}$) were measured using a calibrated Knowles microphone and attached probe tube. A custom pre-amplifier boosted the signal by 20 dB before the voltage was recorded. The microphone voltages were converted to sound pressure amplitude and phase.

4. ***Compound action potentials***

Compound action potentials were measured to assess the influence of the BC-induced ECSP on the cochlear stimulus. A National Instruments data acquisition system (PXI-8119,-4461,-6122), controlled by custom software package (*Cochlear Function Test Suite*) written in the LabVIEW Programming Environment, was used for recording CAPs (Maison *et al.*, 2007) during bone-conduction stimulation. An electrode was placed in contact with the cochlear promontory, approximately 1 mm inferior to the round window. Access to the cochlear promontory was achieved through an opening in the posterior tympanic cavity. The electrode response was amplified 1000x by a Grass Instruments pre-amplifier with 300 Hz to 3000 Hz bandpass. Stimuli were 8.5 ms tone bursts of (0.2, 0.25, 0.31, 0.4, 0.5, 0.63, 0.79, 1.0, 1.26, 1.59, 2.0, 2.52, 3.17, 4.0, 5.04, 6.35, and 8) kHz. Stimulus level was adjusted in 5 dB steps. Responses were averaged from 24 measurements at each frequency. Thresholds were the lowest sound pressures that reliably produced a visible N1 (early negative peak associated with the cochlea).

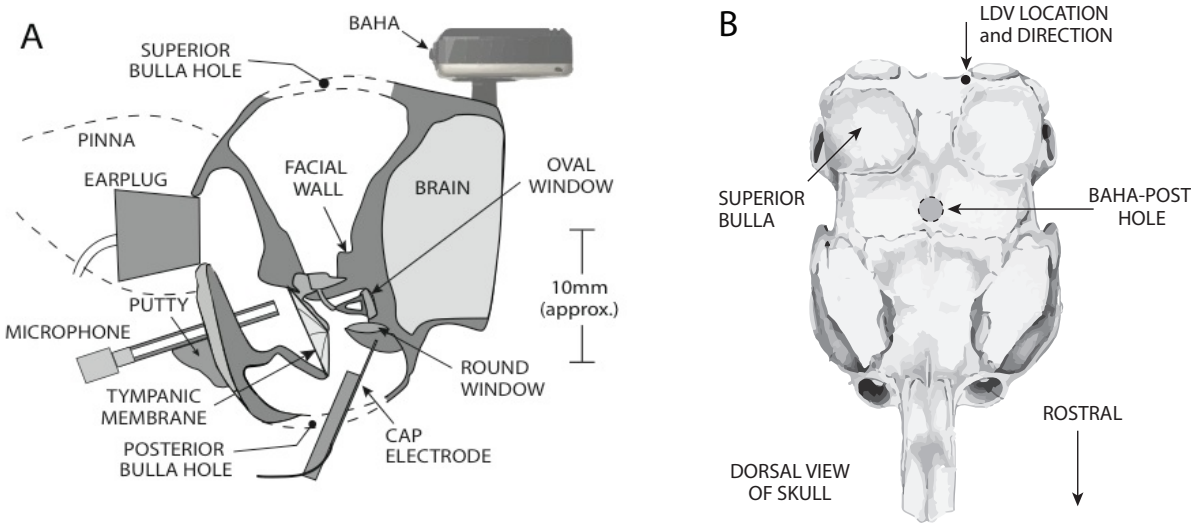

Figure 3.1. Chinchilla experimental setup.
A) Illustration shows the placement of the microphone for recording ECSPs at the TM, placement of the electrode to measure CAPs, the earplug (or silicone) for occlusion of the opening of the bony canal, and location of holes placed in the superior and posterior bullae. B) The BAHA post is placed and cemented 1 mm deep within a 3 mm diameter hole drilled into the

skull along the sagittal suture and just posterior to the coronal sutures. The LDV measures skull velocity from the bone at the top of the posterior bulla, at the back of the head and in a near posterior-anterior direction.

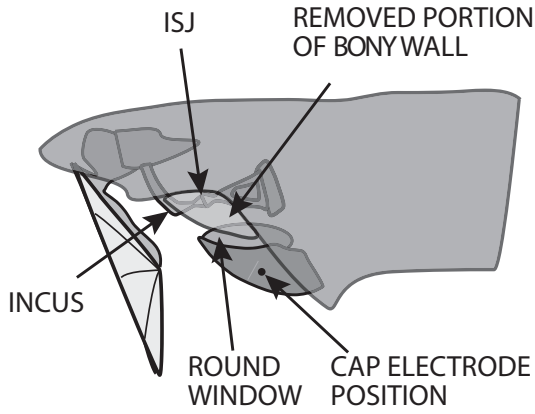

Figure 3.2 Access to the incudostapedial joint.
The posterior bulla hole allowed access to the incudostapedial joint and round window. A portion of bony wall that follows the posterior facial canal is removed when the ISJ is not otherwise visible.

C. Estimation of external ear BC source magnitude and phase

Sound pressure measurements near the TM were combined with model estimates of middle-ear and ear-canal acoustic impedance to characterize the EEBC sources. We first approximated the EEBC by a single ideal (unaltered by the load placed on it) point volume-velocity source located within the external ear canal just lateral to the TM. This source described the sinusoidal change in ear-canal volume change due to the summed compressions and expansions of the canal walls. (A more precise model would be a set of sources distributed along the canal walls throughout the external ear canal.) The definition of the source depended on measurements of the ECSP at the TM ($\mathbf{P_{TM}}$) evoked by bone-conduction that may contain contributions from other

sources, e.g. the motion of the TM or sound air-conducted sound radiated by the BAHA that enters the ear canal. These possible contaminants are dealt with later.

If we consider the walls of the canal to be much stiffer and more dense than air, the acoustic load impedance $\mathbf{Z_S}$ on a sound source near the TM is the parallel combination of the reverse ear-canal input impedance $\mathbf{Z_{EC}}$ (the impedance looking out the ear canal from the TM, e.g. Rosowski et al. 1989) and the middle-ear input impedance $\mathbf{Z_{ME}}$, as described in Figure 3.3 and Equation 3.1.

$$\boldsymbol{Z_S = \frac{Z_{EC} \cdot Z_{ME}}{Z_{EC} + Z_{ME}}} \tag{3.1}$$

As noted above, $\mathbf{Z_{ME}}$ was defined by an earlier model of the middle ear. We modeled $\mathbf{Z_{EC}}$ with a concatenation of anatomically defined conical horns represented by a two-port transmission matrix (described below) that is terminated by either a radiation impedance (unoccluded ear) or an open circuit (occluded ear) (Figure 3.4).

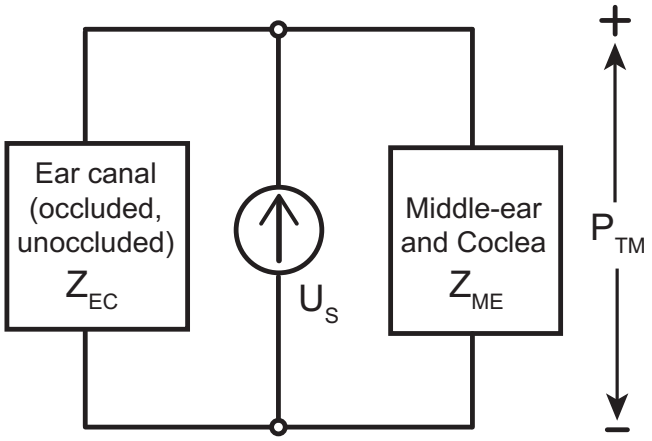

Figure 3.3. Placement of EEBC source.
Block diagram of external-ear bone-conduction source and impedances seen by source: reverse input impedance of the external ear canal $\mathbf{Z_{EC}}$, and the middle-ear input impedance $\mathbf{Z_{ME}}$.

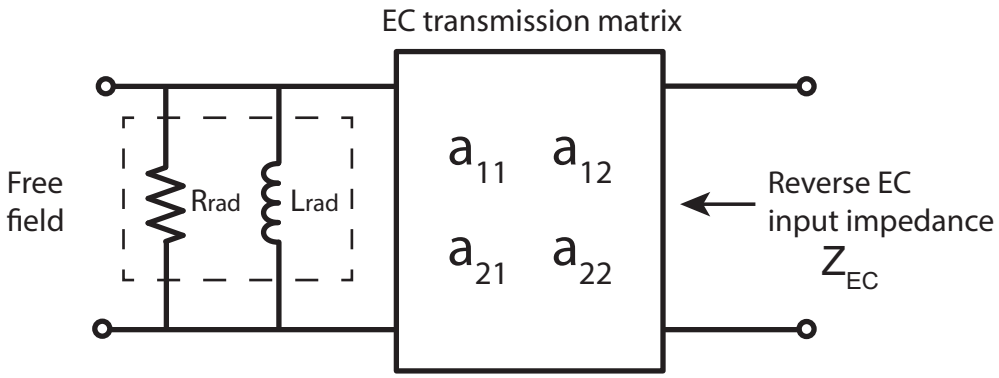

Figure 3.4. Model of external ear canal.
The external ear canal impedance $\mathbf{Z_{EC}}$ is modeled by a transmission matrix coupled to a termination impedance, shown enclosed by a dashed line. The termination impedance here is a radiation impedance, representing the case of the unoccluded ear. The occluded ear termination impedance is modeled as an open circuit.

The volume velocity produced by the single EEBC ($\mathbf{U_S}$) was calculated with the external ear either occluded ($\mathbf{U_{S\_OC}}$, Equation 3.2) or unoccluded ($\mathbf{U_{S\_UN}}$, Equation 3.3).

$$\boldsymbol{U_{S\_OC}} = \frac{\boldsymbol{P_{TM\_OC}}}{\boldsymbol{Z_{S\_OC}}} \tag{3.2}$$

$$\boldsymbol{U_{S\_UN}} = \frac{\boldsymbol{P_{TM\_UN}}}{\boldsymbol{Z_{S\_UN}}} \tag{3.3}$$

where $\mathbf{P_{TM\_OC}}$ and $\mathbf{P_{TM\_UN}}$ are measured sound pressures in the ear canal at the TM in the occluded and unoccluded case, respectively, and $\mathbf{Z_{S\_OC}}$ and $\mathbf{Z_{S\_UN}}$ are the load impedances acting on the source in the occluded and unoccluded cases. In each external ear condition we estimated the single source with $\mathbf{P_{TM}}$ measured under three different middle-ear conditions: normal, interrupted incudostapedial joint, and fixed incus-malleus (described below). In order to standardize measurements across animals and different experimenters, the measured sound pressures are normalized by the measured skull velocity $\mathbf{V_{skull}}$, (supplemental Figure B.4) unless otherwise noted. Skull velocity measurements were consistent within individual experiments,

while skull velocities across experiments were less consistent, likely due to variations in coupling between the BAHA and skull.

D. Estimation of ear canal impedance, Z_{EC}

1. Digital 3D model of ear canal

A 3D reconstruction of the chinchilla auditory periphery, comprising the external, middle, and inner ear, was generated from microCT images from a single cadaveric chinchilla ear. The scan resolution was 36 μm^3/voxel, the highest possible resolution for a specimen approximately 78 mm in length and 35 mm in diameter. The scan was performed at the Ortho Biomechanics Lab at Beth Israel Deaconess Medical Center, Boston, MA. The 3D reconstruction was performed using Amira software. A view of a sectioned 3D representation of the ear is included as supplemental Figure B.1.

2. Geometry of the cartilaginous canal

The geometry of the cartilaginous portion of the ear canal was approximated by the concatenation of conical horn segments of equal length (0.72 mm) and varied cross-sectional areas determined from the 3D model of the canal (supplemental Figure B.2). The longitudinal axis of the cartilaginous canal was approximated by a straight line. The lateral opening of the model's cartilaginous canal tube is located along the canal's central axis and is described by the lateral-most location where the perimeter of the cartilage segment is first complete. Any effects of the cartilaginous pinna flange (more lateral locations where the perimeter is incomplete) should be relatively small (Beranek and Mellow, 2012) and are not considered.

3. Geometry of the bony ear canal

The longitudinal axis of the curved bony canal was determined subjectively. Each cross-section of the segmented representation of the bony canal in supplemental Figure B.2 represents a section that is orthogonal to the longitudinal axis in the 3D model. Distances between adjacent cross-sections were estimated by the straight-line distance between their intersection with the longitudinal axis. The total length of the ear canal, estimated at 10.16 mm, is similar to the summed length of the longitudinal axes of the cartilaginous and bony canals in supplemental Figure B.1.

4. Reverse ear canal impedance

Each conical-horn segment of the ear canal is represented as a 2-port network, and described by a transmission matrix T (Equation 3.4), where P_T and U_T are the pressure and volume velocity at the throat (smaller diameter opening of horn), and P_M and U_M are the pressure and volume velocity at the mouth of the horn (Beranek and Mellow, 2012).

$$\begin{bmatrix} \boldsymbol{P_T} \\ \boldsymbol{U_T} \end{bmatrix} = \begin{bmatrix} \boldsymbol{a_{11}} & \boldsymbol{a_{12}} \\ \boldsymbol{a_{21}} & \boldsymbol{a_{22}} \end{bmatrix} \cdot \begin{bmatrix} \boldsymbol{P_M} \\ \boldsymbol{U_M} \end{bmatrix} = \boldsymbol{T} \cdot \begin{bmatrix} \boldsymbol{P_M} \\ \boldsymbol{U_M} \end{bmatrix} \ . \tag{3.4}$$

Matrix elements of **T** are defined from the geometry of each segment (Equations 3.5-3.8)

$$\boldsymbol{a_{11}} = \sqrt{\frac{S_M}{S_T}}\left(\cos kl - \frac{1}{kx_M}\sin kl\right) \ , \tag{3.5}$$

$$\boldsymbol{a_{12}} = j\frac{\rho_o c}{\sqrt{S_T S_M}}\sin kl \ , \tag{3.6}$$

$$\boldsymbol{a_{21}} = j\frac{\sqrt{S_T S_M}}{\rho_o c}\left\{\left(\frac{1}{kx_M} - \frac{1}{kx_T}\right)\cos kl + \left(1 + \frac{1}{k^2 x_M x_T}\right)\sin kl\right\} \text{ and} \tag{3.7}$$

$$\boldsymbol{a_{22}} = \sqrt{\frac{S_T}{S_M}}\left(\cos kl + \frac{1}{kx_T}\sin kl\right) \ , \tag{3.8}$$

where S_M and S_T are the cross-sectional areas of the mouth and throat respectively, l is the length of the segment and x_M and x_T are related to the slope of the conical walls. Also, k is the wave number defined as $2\pi f/c$; f is sound frequency in Hz; c is the propagation velocity of sound in air, and ρ is the density of air. The geometric description of the conical horn is detailed in supplemental Equations B.1 to B.5 and Figure B.3. The impedances looking into the throat ($\mathbf{Z_T}$) and the mouth ($\mathbf{Z_M}$) of each horn segment are defined by:

$$\boldsymbol{Z_T} = \frac{a_{11}\boldsymbol{Z_{AM}} + \boldsymbol{a_{12}}}{\boldsymbol{a_{21}}\boldsymbol{Z_{AM}} + a_{22}} \tag{3.9}$$

$$\boldsymbol{Z_M} = \frac{a_{22}\boldsymbol{Z_{AT}} + \boldsymbol{a_{12}}}{\boldsymbol{a_{21}}\boldsymbol{Z_{AT}} + a_{11}} \tag{3.10}$$

E. Contribution of middle and inner ear BC sources in EEBC estimates

External-ear volume-velocity sources were estimated from $\mathbf{P_{TM}}$ measurements made in three middle-ear conditions: the normal middle ear, with the incudostapedial joint (ISJ) interrupted, and with the malleus-incus (MI) [in the chinchilla these ossicles are ankylosed into a single bone; (Vrettakos *et al.*, 1988)] fixed to the cochlear promontory by dental cement between the distal incus and the bone surrounding the cochlear base. Immobilization of the MI greatly reduces any contribution of ossicular inertia and inner ear BC mechanisms to the measured $\mathbf{P_{TM}}$ during BC stimulation. ISJ interruption removes contribution of inner-ear BC sources from the $\mathbf{P_{TM}}$ measurements. Estimation of the EEBC in the three manipulated states required the definition of the middle-ear input impedances from our model of the chinchilla middle ear (Bowers et al. 2019).

F. Isolation of contributions of cartilaginous and bony canals to EEBC

As will be described, our initial results suggested the $\mathbf{P_{TM}}$ measured with the unoccluded external ear might be better fit by 2 volume-velocity sources, one accounting for the contribution of the cartilaginous portion of the ear canal ($\mathbf{U_{cart}}$) and a second source accounting for the contribution of the bony canal ($\mathbf{U_{bone}}$). The two-source model terminated medially by the ME and cochlea, and laterally by the impedance associated sound radiating to the outside is illustrated in Figure 3.5A. The cartilaginous and bony canals are modeled as the two-port networks $\mathbf{T_{cart}}$ and $\mathbf{T_{bony}}$, respectively. $\mathbf{P_{EC}}$ is the sound pressure at the boundary between the bony and cartilaginous canals. A similar lumped-element circuit model was developed by Stenfelt and Reinfeldt (2007), with major differences being 1) their ear canal segments were modeled as a network of lumped elements, as opposed to two-port networks, and 2) the bony and cartilaginous canal sources were located midway along their respective canal segments, as opposed to being located at the most-medial location of the segments.

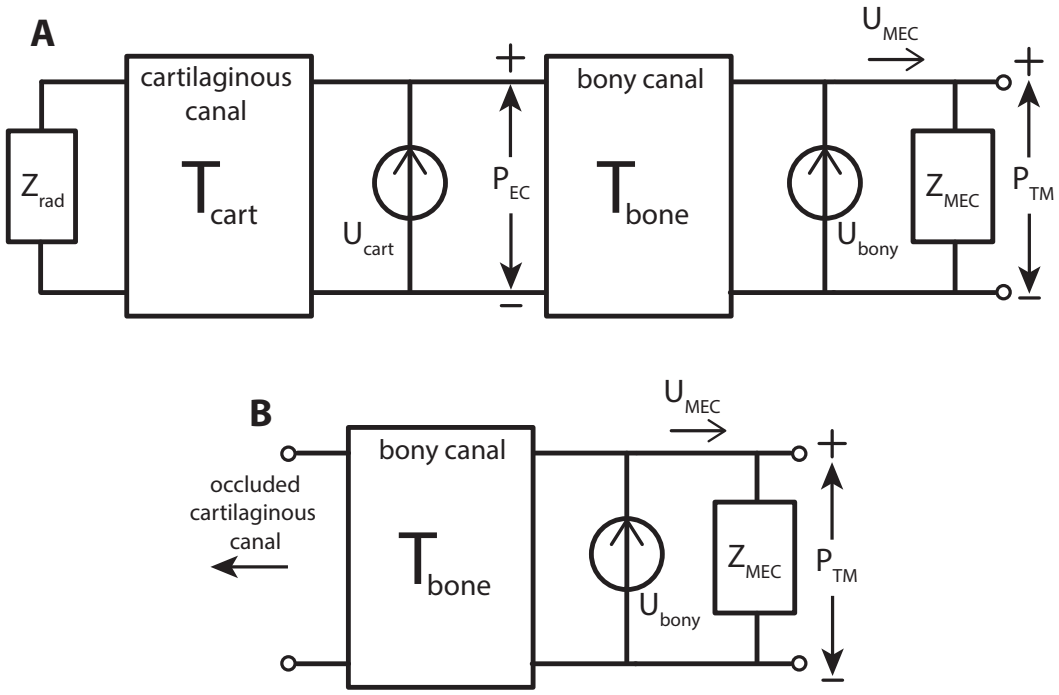

Figure 3.5 Two-source representation of EEBC.
(A) Expanded model of ear canal and it's BC sources, and the middle ear and cochlea, and (B) model of occlusion of the medial end of the cartilaginous ear canal, which includes the rigidly terminated bony ear canal, the bony ear-canal source, and the impedance of the middle ear, and cochlea.

We represent the bony-canal volume-velocity source $\mathbf{U_{bone}}$ in this model by our initial estimate of the EEBC in the occluded ear canal case, as the occlusion prevents any contribution of the motion of the cartilaginous canal walls to $\mathbf{P_{TM}}$ (Figure 3.9B). If we assume $\mathbf{U_{bone}}$ is independent of the occlusion, and using superposition, the $\mathbf{P_{TM}}$ produced by the cartilaginous source, $\mathbf{U_{cart}}$, alone is described as the complex difference between the $\mathbf{P_{TM}}$ measured when the canal is unoccluded and the $\mathbf{P_{TM}}$ produced by $\mathbf{U_{bone}}$ in the unoccluded state. (The contribution of $\mathbf{U_{bone}}$ to the unoccluded $\mathbf{P_{TM}}$ is computed from the source definition and the model.) The sound pressure $\mathbf{P_{EC}}$ (due to the cartilaginous source alone) associated with the difference defined $\mathbf{P_{TM}}$

was then calculated using the ear-canal transmission matrices. $\mathbf{U_{cart}}$ (Figure 3.5A) was then defined as the ratio of its contribution to the BC-induced $\mathbf{P_{EC}}$ to the impedance load on the cartilaginous-canal source produced by the parallel combination of the impedances due to the unoccluded cartilaginous canal and the impedance looking into the middle-ear-terminated bony canal.

G. Estimation of lower-jaw motion to BC-induced ECSP

The contribution of relative motion of the lower jaw to the BC-induced ECSP was investigated by comparing $\mathbf{P_{TM}}$ measurements made while the lower jaw was intact to those made after resecting the boney connection of the ipsilateral side lower jaw to the skull. (Resection of the jaw was performed only on cadaveric chinchillas.) Enough jaw and muscle were removed to prevent contact between the jaw and the ear canal; however, much of the jaw was left in place so as to not significantly alter the vibration-induced motion of the head. The external ear was intact and unoccluded. The ISJ was interrupted to minimize the effects of the middle and inner-ear BC sources on the measured ECSP; results from Methods section I suggest fixation of the ossicles is not necessary to isolate the effect of the external-ear source on the BC-induced ECSP, and ISJ-interruption, although also unnecessary, is relatively trivial to perform.

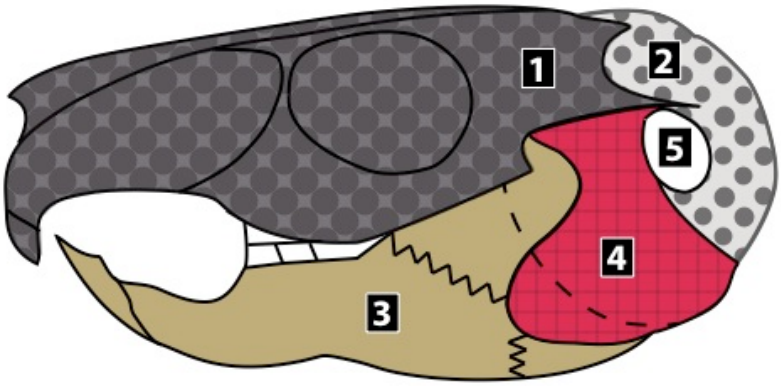

Figure 3.6. Chinchilla skull.
1) Anterior portion of skull, 2) posterior portion of skull [bullae of middle ear], 3) lower jaw, 4) muscle, cartilage, and connective tissue, and 5) entrance to bony portion of ear canal. The dashed line approximates the boundary of the middle-ear cavity behind the soft tissue and jaw. Jagged lines illustrate where the lower jaw was resected, while the teeth bearing components of the jaw were kept in place.

H. Effect of EEBC on bone-conduction hearing

CAP thresholds in response to BC stimuli were measured in the normal ear and the ISJ-interrupted ear while the ear canal was unoccluded. A comparison of these thresholds placed limits on the contribution of the EEBC to hearing thresholds in the unoccluded ear. The process was repeated with the ear canal occluded.

Thresholds in the normal, unoccluded ear were compared to thresholds in the normal, occluded ear to investigate the effect of ear-canal occlusion on BC-hearing thresholds: the so-called ‘occlusion effect’. The process was repeated for the case in which the ISJ was interrupted to investigate whether the occlusion affected non-external-ear BC pathways.

III. Results

A. Vibrational response to BC stimulation

Skull velocity was measured simultaneously with each sound-pressure measurement. Examples of the vibrational response of the skull are shown in supplemental Figure B.4 (Top). With both the BAHA© 3 (BP100) and a BAHA© 5 SuperPower, the measured velocity has a band pass quality. The BAHA© 3 peak response was generally between 700 Hz and 3 kHz, while the BAHA© 5 peak response was between 400 Hz and 900 Hz. The velocity produced by the BAHA© 5 was at least 10 dB above the noise floor across all frequencies, while the velocities produced by the BAHA© 3 did not meet our 10 dB signal-to-noise criterion above 8 kHz.

B. Ear canal sound pressures produced by bone conduction

1. Ear canal sound pressures

Examples of the measured P_{TM} in response to BC stimulation, as well as the measured noise floor, are shown on the right side of in supplemental Figure B.4. The measured ECSPs had a band pass quality that is similar to that of the velocity produced by the stimulator with peak resonances between 700 Hz and 2 kHz. Our 10 dB signal-to-noise criteria often excluded measured pressures at the lowest ($f < 0.35$ kHz) and highest frequencies ($f > 8$ kHz). Errors due to noise may be compounded in our EEBC estimates, as they depend on both velocity and sound pressure.

2. Effect of Canal Occlusion on P_{TM}

The occlusion effect, defined by the ratio of the BC-induced P_{TM} after occlusion at the entrance to the bony canal to the P_{TM} measured with an unoccluded canal, is shown in Figure 3.7 for 3 different middle states: 1) normal ME, 2) ISJ interruption, and 3) the MI fixed to the

cochlear promontory. Occlusion of the normal ear causes an increase in the mean P_{TM} of between 5 dB and 12 dB below 2 kHz. Between 2 kHz and 6 kHz, P_{TM} is higher in the unoccluded case; over this frequency range there are 2 apparent minima in the ratio of occluded to unoccluded measurements, likely determined by resonant frequencies of the ear canal. In the ISJ-interrupted ear, the occlusion increases P_{TM} with increasing frequency from 2 to 10 dB between 300 Hz and 2 kHz. As with the normal ear, the occlusion produces a sharp decrease in P_{TM} between 2 kHz and 2.5 kHz, and the dB value of the ratio becomes negative at approximately 2.1 kHz. Minima are again observed between 2 kHz and 6 kHz. In the normal and ISJ-interrupted ears, occlusion increases P_{TM} above 6 kHz. With immobilization of the malleus-incus occlusion produces a maximum in the ratio near 300 Hz (22 dB on average); as frequency increases from 0.4 to 3 kHz, the effect decreases. The effect increases sharply from 3 kHz to 3.5 kHz. Above this frequency, the mean occlusion effect is minimal.

The differences in the low frequency magnitude of the occlusion effect in the three conditions is consistent with condition-related differences in the middle-ear input impedance, Z_{ME}. ISJ interruption leads to a reduction in Z_{ME} at low frequencies and produces the smallest occlusion effect magnitude at $f < 2$ kHz. Immobilization of the malleus and incus leads to a significant increase in the magnitude of Z_{ME} in the same frequency range and produces the largest occlusion effect magnitude at $f < 1$ kHz. These impedances are discussed and illustrated in the next section.

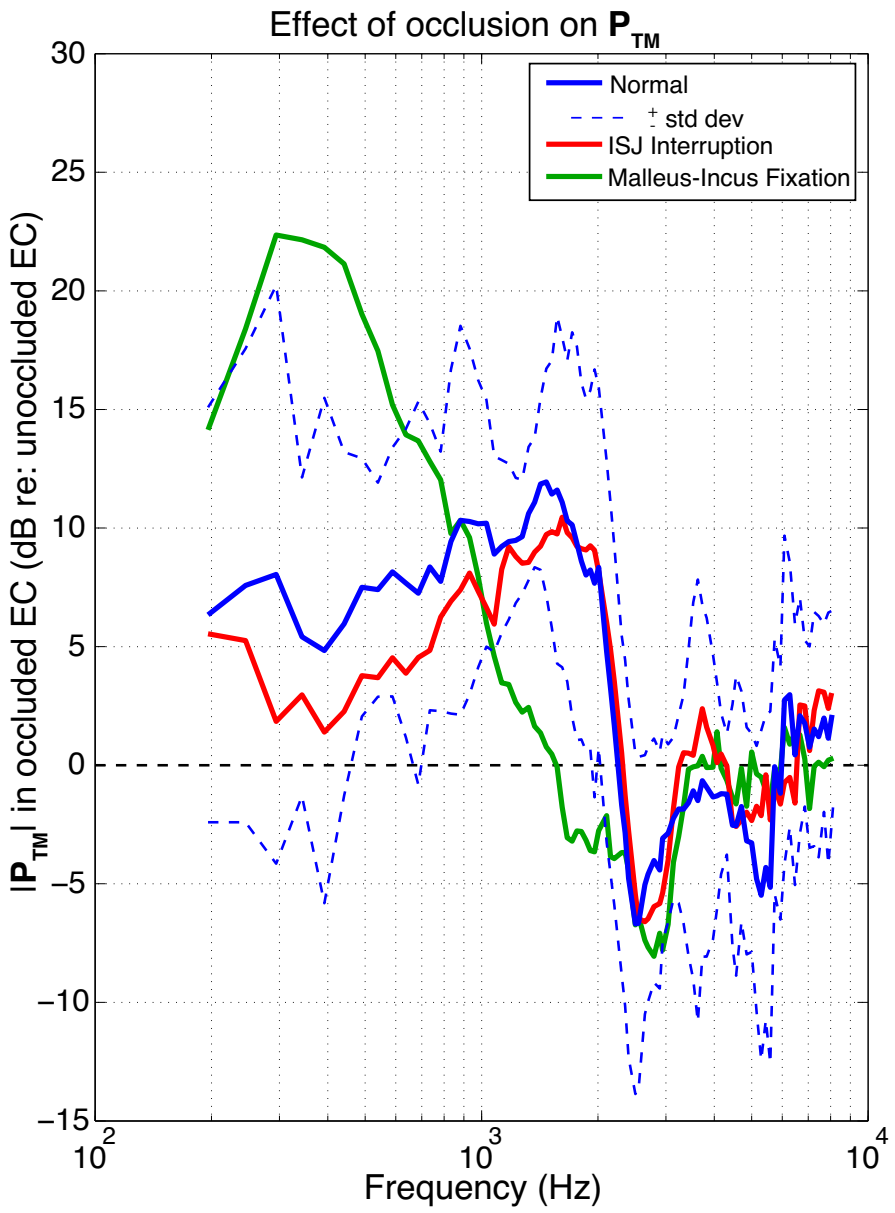

Figure 3.7. Average change in $\mathbf{P_{TM}}$ produced by occlusion of the ear canal for various middle-ear states.
This effect is quantified as the ratio of $\mathbf{P_{TM}}$ in the occluded canal relative to the $\mathbf{P_{TM}}$ in the unoccluded case, and is shown for the normal (n = 12), ISJ-interrupted (n = 12), and MI-fixed middle ear (n = 10). The standard deviations associated with the manipulated states of the middle ear are similar in magnitude to those of the normal state.

C. Acoustic impedances

The acoustic impedance looking out the ear canal from the TM ($\mathbf{Z_{EC}}$) is shown in Figure 3.8A for the following conditions: 1) the impedance of the bony canal terminated by an occlusion (EC occluded), 2) the impedance of the entire canal terminated by a radiation impedance (EC unoccluded), and 3) the impedance of the cartilaginous canal terminated by a radiation impedance (EC unoccluded short). Our canal impedance computations do not account for viscous or heat losses at the tube walls [the effects of such losses are discussed by Lynch et al., (1994)] and therefore predict a very sharp minima in the impedance in the occluded external ear. The sharpness of the resonances in the unoccluded ear canal is limited by losses due to the radiation of sound into the environment (Rosowski *et al.*, 1988). In the same figure, middle-ear input impedances ($\boldsymbol{Z_{ME}}$) are plotted for the 1) the normal middle ear and cochlea, 2) the middle ear with ISJ interruption, and 3) the MI-fixed middle ear.

The load impedances (Equation 3.1) on a single-point source, located in the ear canal near the TM (at cross-section 10 of bony ear canal in supplemental Figure B.2), for the 3 conditions of the middle ear are shown in Figure 3.8B, each combined with the open and closed conditions of the ear canal.

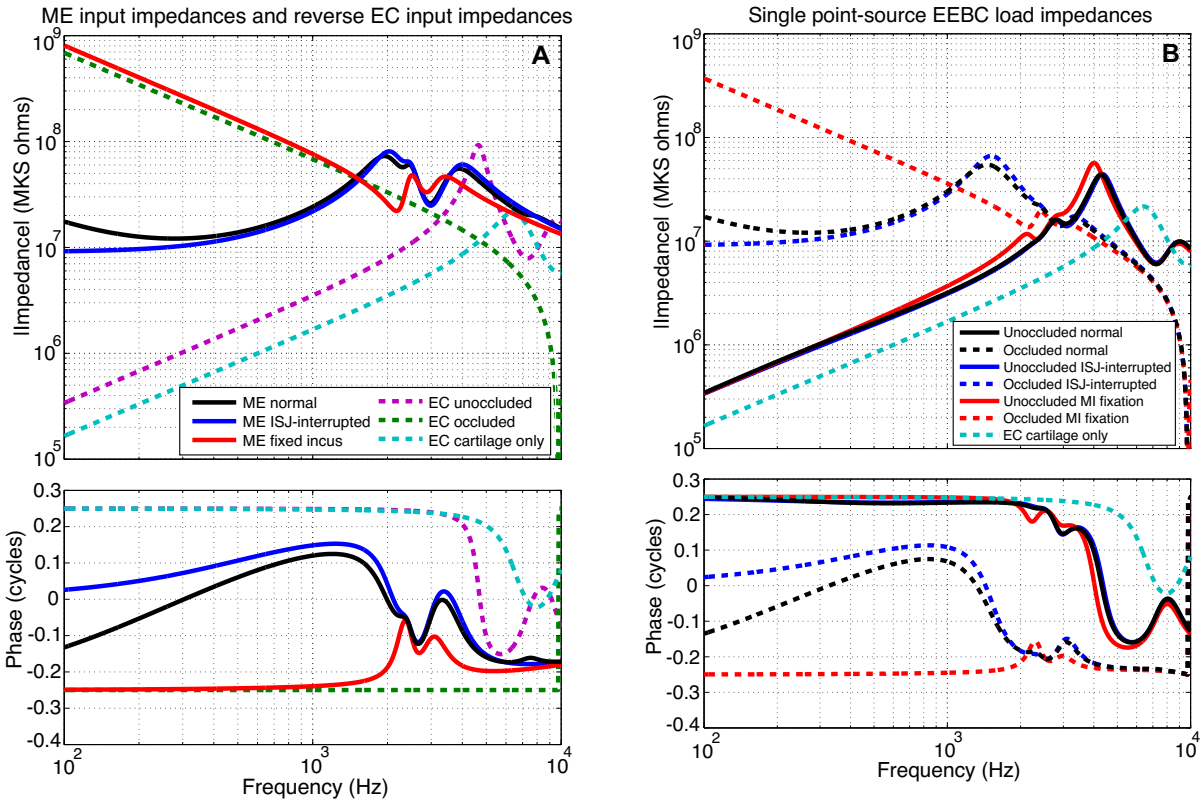

Figure 3.8. Model impedances.
(A) $\mathbf{Z_{EC}}$, the reverse input-impedance of ear canal (unoccluded, occluded, and unoccluded cartilaginous portion only), and $\mathbf{Z_{ME}}$ middle-ear input impedances (normal, ISJ-interrupted, and MI-fixed conditions; open bullae). (B) Computed load impedances acting on a point source located near the TM (at cross-section 10 of bony ear canal in supplemental Figure B.2). Each impedance is a parallel combination of a $\mathbf{Z_{EC}}$ and $\mathbf{Z_{ME}}$. The source impedance produced by the combinations of the unoccluded ear canal impedance and the normal or ISJ-interrupted $\mathbf{Z_{ME}}$ are very similar.

D. Single-source estimates of EEBC

The EEBC (with units of volume velocity, m^3/s, normalized by head velocity, m/s) was first approximated as a single point-source located near the TM. In all cases, the middle-ear cavities were open. We first estimated the source from the unoccluded-ear data using Equation 3.2, $\mathbf{P_{TM}}$ measurements and the source-load impedance estimates of Figure 3.8B. The magnitude and

phase of $\mathbf{U}_{S\_UN}$ in the case of the normal ME, ISJ interruption, and the MI immobilization are shown in Figure 3.9A. As noted previously the middle-ear manipulations were designed to remove any middle- and inner-ear contribution to the measured sound pressures. The bottom panel in Figure 3.9A points out the magnitudes of the three computed source estimates are generally within ±3 dB. Students' t-test comparing two conditions at each frequency suggest the magnitudes of the estimated EEBC in the ISJ-interrupted ear compared to the normal ear are not statistically different at any frequency with valid measurements ($P > 0.05$). The magnitude of the EEBC in the MI-fixed condition compared to that of the normal ear appear statistically different over a limited range of frequencies (3.1 to 4.2 kHz; $P < 0.02$). While these significance estimates are not corrected for repeated significance testing, their grouping across multiple contiguous frequencies argues against a chance occurrence.

The EEBC was also estimated in the occluded ($\mathbf{U}_{S\_OC}$) ear-canal case (Figure 3.9B). The normalized source magnitudes, based on the 3 middle-ear conditions, are fairly flat below 3 kHz, while increasing at approximately 12 dB/octave above this frequency. The magnitude of the estimated EEBC based on measurements in, and impedances of the ISJ-interrupted ear are not statistically different from the normal $\mathbf{U}_{S\_OC}$ at frequencies between 200 Hz and 8 kHz ($P > 0.05$), and the differences between the occluded source magnitudes for the normal and the ISJ condition are less than 1-2 dB (Figure 3.9B, bottom panel).

The source magnitude based on the occluded, MI-fixed condition is different from that of the occluded, normal middle-ear-based estimate over much of this frequency range (grey boxes denote frequency regions over which there are apparent statistical differences in estimated mean magnitude, $P < 0.05$). Given the more random distribution in the frequency domain of some of these findings and a lack of correction for repeated significance testing, some of these

differences are likely random in nature. However, the clustering of apparent significance between 0.6 and 1 kHz argues for real differences in this range, and its likely the computed source magnitudes in the IM-fixed condition are 6 to 10 dB smaller than the normal and ISJ-interrupted sources in this range.

Figure 3.10 compares the computations for the single-source estimates in the unoccluded and occluded ear canal conditions in the case of a normal middle ear. The magnitude of $\mathbf{U}_{S\_UN}$ is about 10 dB larger than $\mathbf{U}_{S\_OC}$ at frequencies below 3.5 kHz. Between 4 kHz and 5 kHz, $|\mathbf{U}_{S\_OC}|$ is approximately 10 dB greater than the magnitude of the unoccluded condition, and above 5 kHz the two magnitudes are similar. The phases of the sources estimates are similar above 500 Hz, but diverge below this frequency. The consistent ~10 dB differences in the EEBC source magnitudes computed from the occluded and unoccluded sound pressures at frequencies less than 5 kHz, suggests that a single source in the bony canal near the TM cannot explain the sound pressures we measured in the two ear canal conditions and argues for the presence of another source within the cartilaginous canal.

Figure 3.9: EEBC estimates in the normal and modified middle-ear condition, with and without occlusion of the ear canal.
(A) The EEBC is estimated as a point source located near the lateral side of the TM. The measured sound pressures, each scales relative to the skull velocity, are divided by the appropriate modeled ME input impedance, depending on the middle-ear condition in which the sound pressures were measured; normal (n = 12), ISJ-interruption (n = 12), or immobilized MI (n = 10). Top panel shows the computed source magnitudes; grey boxes denote frequency regions where there is a computed difference between the normal and IM-fixed magnitudes ($P < .05$). The middle panel shows the computed phases. The bottom panel shows the ratios of the ISJ interrupted and MI fixed computations to the normal case. (B) As in A, single sources computed in the occluded case; normal (n=12), ISJ-interrupted (n=12), and MI-fixed middle-ear conditions (n=10).

Figure 3.9 (continued)

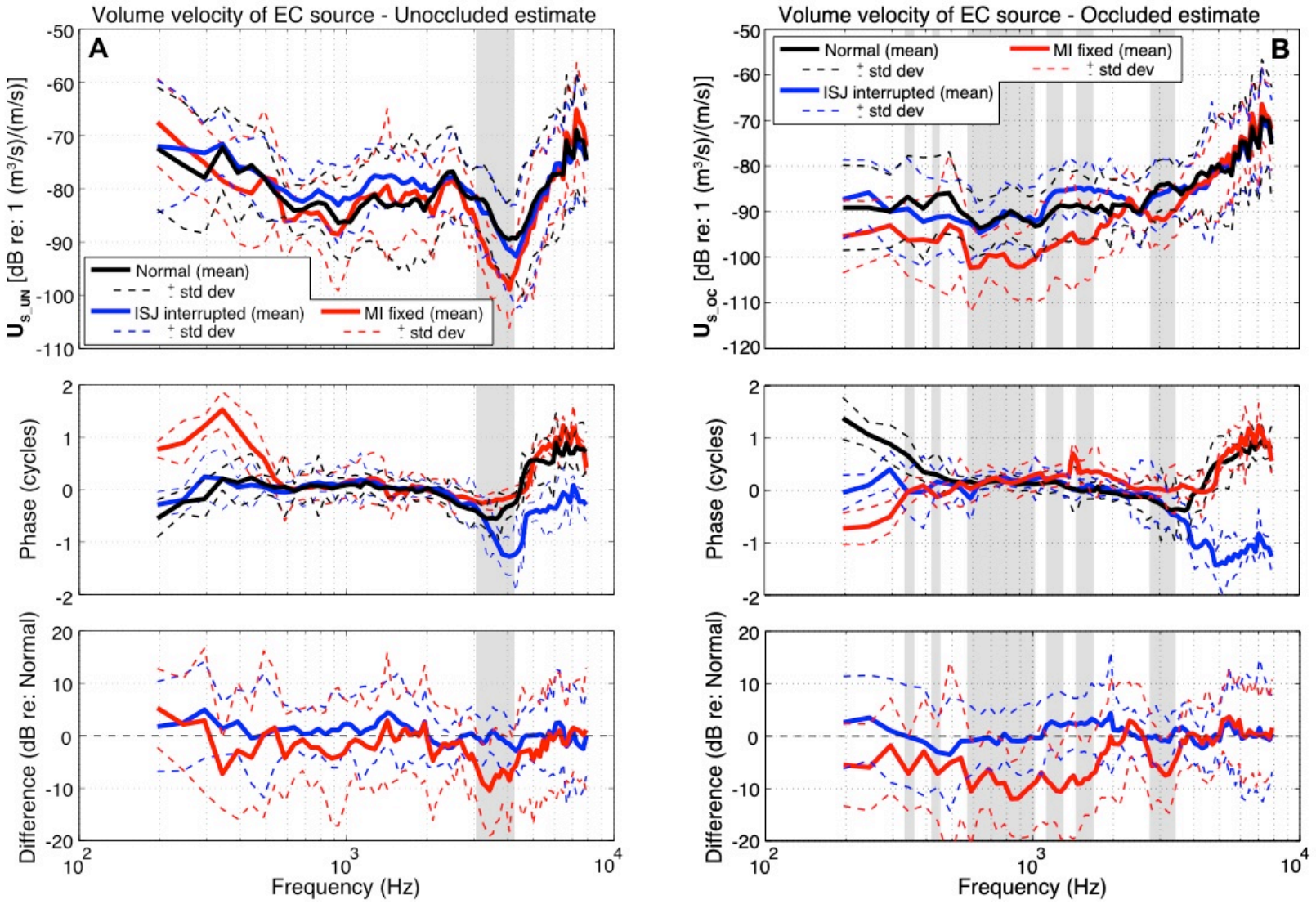

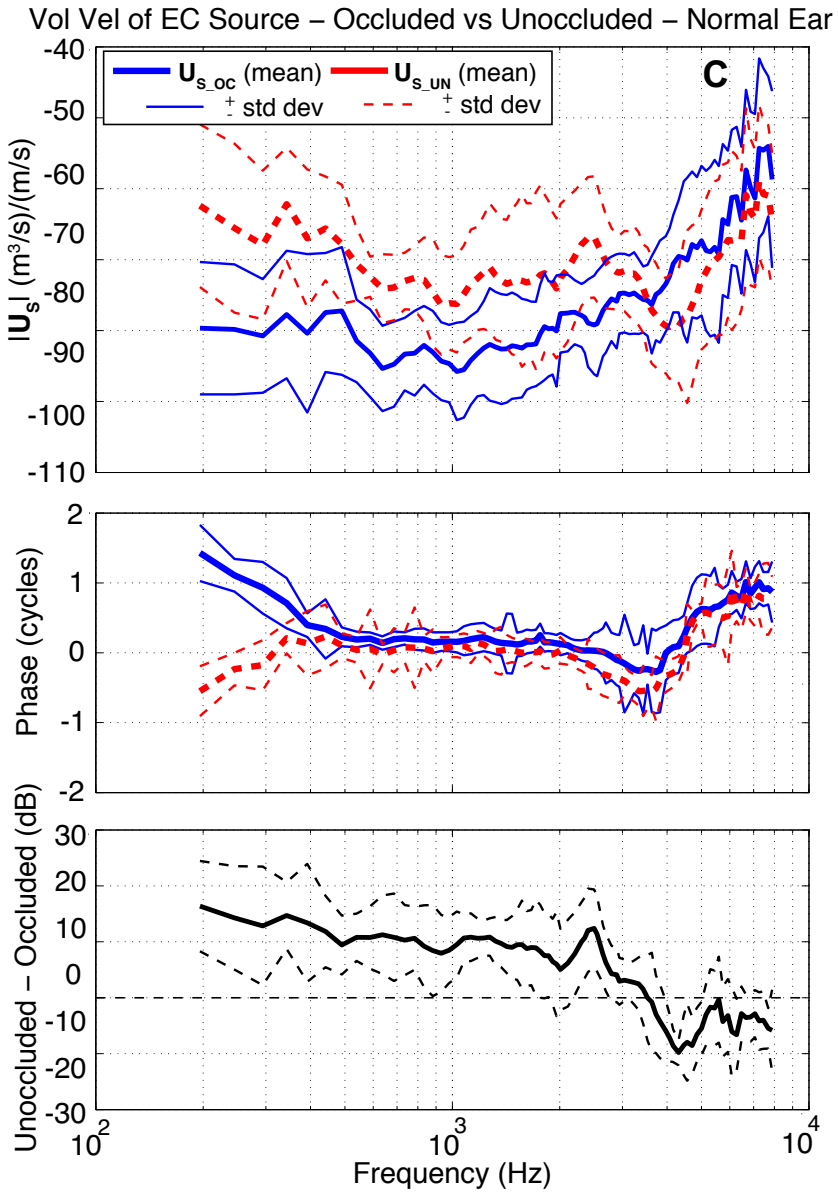

Figure 3.10: EEBC estimates in the normal middle-ear condition, with and without occlusion of the ear canal.
EEBC estimates in the normal-ME condition, with and without occlusion of the ear canal (n = 12 in each case).

E. Bony and cartilaginous canal EEBC estimates

The inability of the single-source model to explain both the occluded and unoccluded sound pressure data, led to tests of a two-source model, with 1) a source for motion of the bony canal walls $\mathbf{U}_{\mathbf{bone}}$ set equal to $\mathbf{U}_{S\_OC}$ (Figure 3.9B), where the occlusion removes any contribution from

the cartilaginous portion of the canal to the measured $\mathbf{P_{TM}}$, and 2) a second source for the motion of the cartilaginous canal walls $\mathbf{U_{cart}}$. We used superposition (as described in the methods) to separate out the contribution of $\mathbf{U_{cart}}$ to $\mathbf{P_{TM}}$ in the unoccluded condition, and then used the model (as described in the methods) to compute the complex magnitude of the cartilaginous canal source.

Estimates of $\mathbf{U_{cart}}$ and $\mathbf{U_{bone}}$ are shown in Figure 3.11. Results are shown for the normal, ISJ-interrupted, and MI-fixed cases. The magnitude and phase of the computed $\mathbf{U_{cart}}$ is nearly independent of the middle-ear condition. At frequencies between 0.5 and 3 kHz $\mathbf{U_{cart}}$ magnitude is about 10 dB greater in magnitude than $\mathbf{U_{bone}}$ for the normal and ISJ-interrupted conditions and between 10 and 20 dB greater than $\mathbf{U_{bone}}$ computed for the IM-fixed condition. $|\mathbf{U_{bone}}|$ for all three conditions is approximately 20 to 25 dB less than $|\mathbf{U_{cart}}|$ at frequencies below 0.5 kHz. Above 4 kHz, the magnitudes of $\mathbf{U_{bone}}$ and $\mathbf{U_{cart}}$ in all middle-ear conditions are similar, with the exception of the normal-ME case between 5 and 7 kHz, where the magnitude of $\mathbf{U_{cart}}$ is up to 10 dB greater than the magnitude of $\mathbf{U_{bone}}$. The source estimates of the two distinct canal sections are generally in phase between 500 Hz and 2 kHz, with the exception of the MI-fixed condition, where the bony-canal source leads $\mathbf{U_{cart}}$ by between an eighth cycle and a quarter cycle between 1 and 3 kHz. Above 3 kHz, comparisons of the different source phase angles are complicated by phase differences of more than 1 cycle.

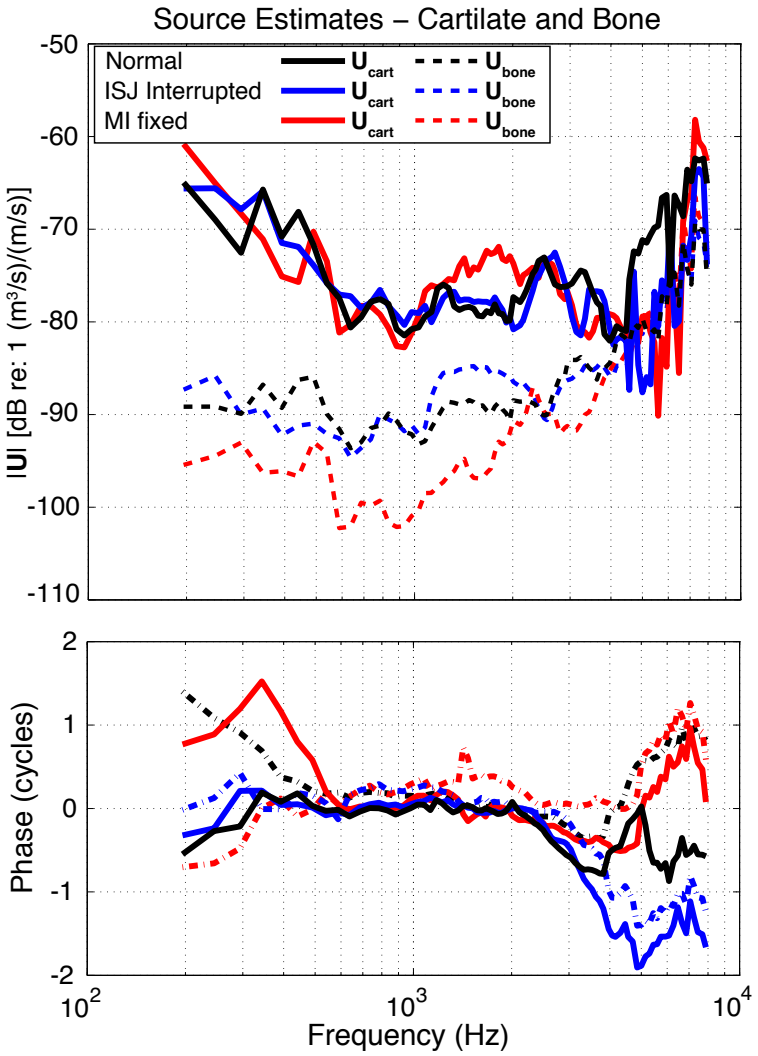

Figure 3.11. Estimates of cartilaginous- and bony-canal sources.
Mean source estimates of the cartilaginous EEBC in the normal, ISJ-interrupted, and MI-fixed middle-ear conditions, shown with the bony-canal source estimates from Figure 3.9B. The number of ears in each population is identical to that described in Figure 3.9, and the standard deviations about the means for the $\mathbf{U}_{\mathbf{cart}}$ sources are equal to those of $\mathbf{U}_{\mathbf{bone}}$.

The measured ECSP at the TM in the unoccluded case with a normal middle ear is shown in Figure 3.12, as are the sound pressures predicted by the cartilaginous and bony-canal sources.

As the characterization of $\mathbf{U}_{\mathbf{cart}}$ depended on the difference between the measured $\mathbf{P}_{\mathbf{TM}}$ in the

unoccluded case and a computation of the $\mathbf{P_{TM}}$ due to $\mathbf{U_{bone}}$, we see no difference between our measured $\mathbf{P_{TM}}$ and the predicted sum of the $\mathbf{P_{TM}}$ produced by the two sources.

The analysis suggests that ECSP in the unoccluded ear is dominated by $\mathbf{U_{cart}}$ below 0.9 kHz and in a band of frequencies between 2 and 4 kHz, where the summed sound pressure resulting from both sources approximates the larger sound pressures produced by $\mathbf{U_{cart}}$. At frequencies between 1 and 2 kHz the sound pressure produce by the two sources are similar in magnitude and phase such that the summed $\mathbf{P_{TM}}$ is roughly twice (6 dB larger than) the $\mathbf{P_{TM}}$ produced by either source. At frequencies above 5 kHz, the measured $\mathbf{P_{TM}}$ in the unoccluded ear is equal to that predicted for the $\mathbf{U_{bone}}$ source alone, and we see a sharp minimum in the $\mathbf{U_{cart}}$ associated $\mathbf{P_{TM}}$. At higher frequencies the sound pressures predicted from $\mathbf{U_{bone}}$ and $\mathbf{U_{cart}}$ are of a similar magnitude.

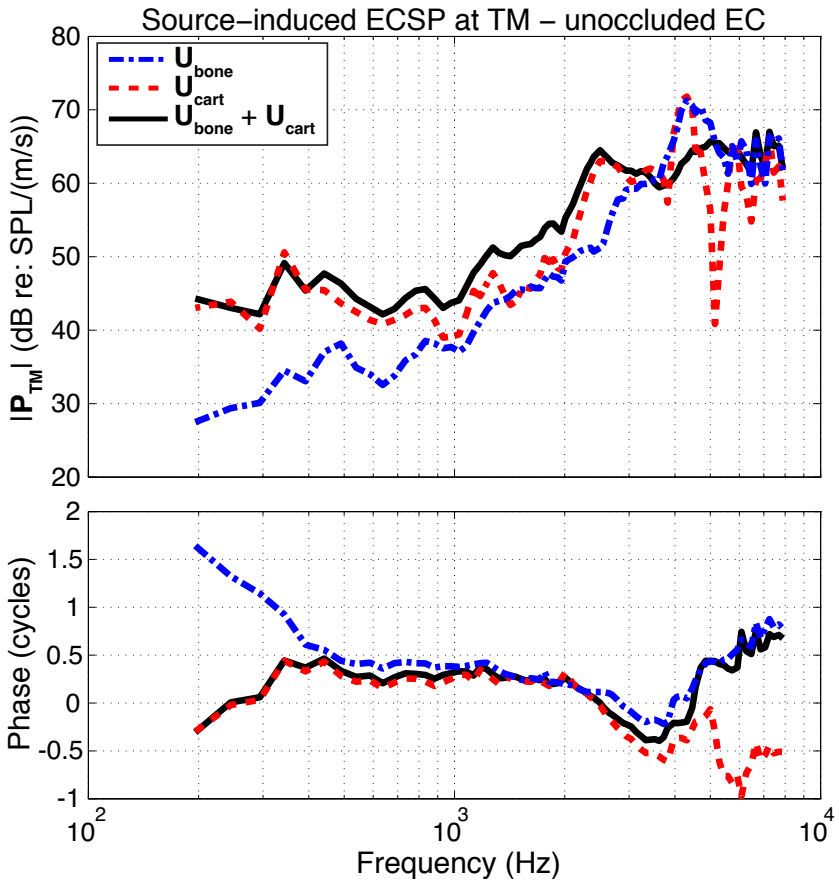

Figure 3.12. BC-induced ECSP.
Sound pressure in ear canal at the TM produced by the $\mathbf{U_{bone}}$, $\mathbf{U_{cart}}$, and the superposition of the two (as measured in the normal middle-ear condition).

F. Contribution of jaw motion to EEBC

Contribution of motion of the lower jaw to the measured ECSP was investigated by comparing the measured $\mathbf{P_{TM}}$, with the lower jaw intact and resected (Figure 3.13). Measurements were made at the TM in the unoccluded ear, as occlusion of the canal might remove potential contribution of volume displacement of the cartilaginous canal space resulting from jaw motion.

The mean magnitude of $\mathbf{P_{TM}}$ with the jaw resected shows no significant difference compared to the mean estimate of the normal case; differences of up to 4 dB are seen between the two estimates, however, their mean values are within one standard deviation of one another.

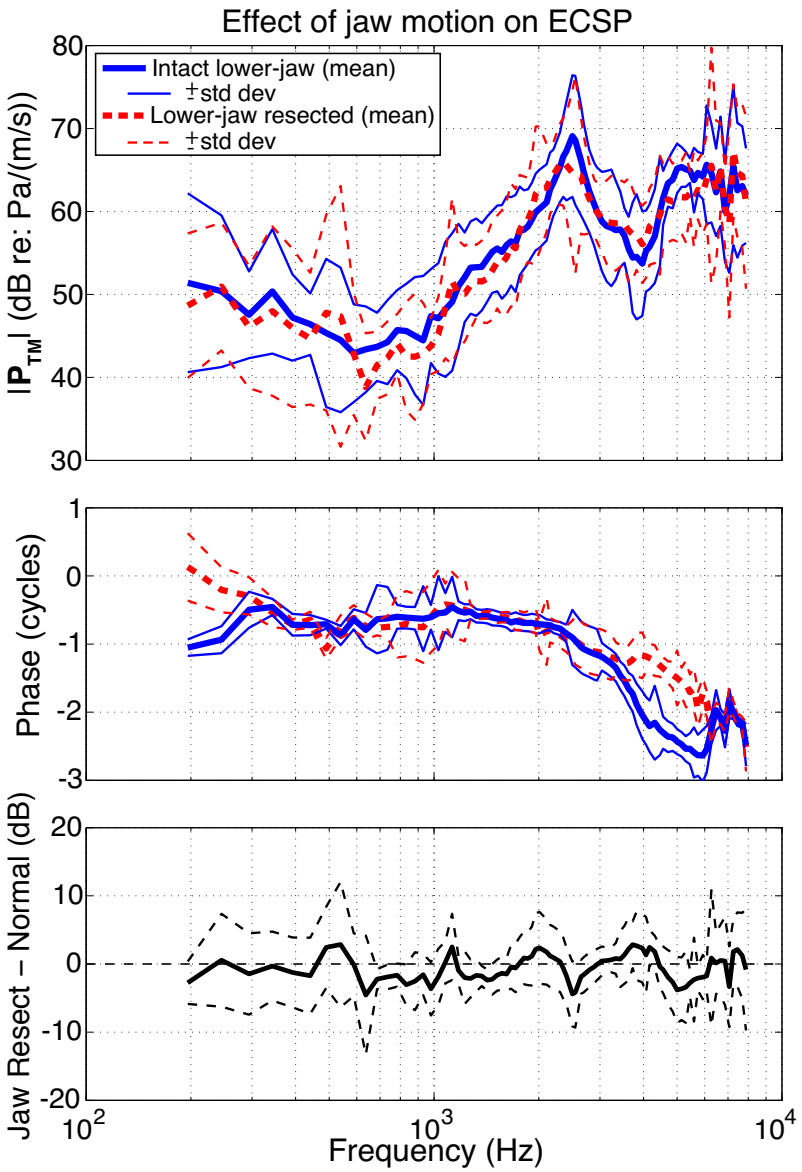

Figure 3.13. ECSP measured at the TM with intact and resected lower jaw (n = 6 in each case).

G. Effect of occlusion on the BC stimulus to the inner ear: CAPs

BC-induced CAPs were measured in deeply anesthetized chinchillas, with the ear canal occluded or unoccluded, both before and after ISJ interruption. The CAP thresholds in the ISJ-interrupted case, relative to the normal ME, are shown in Figure 3.14 for the two ear-canal conditions. The effect of occlusion on CAP thresholds is shown for the normal ear and ISJ-interrupted ear in Figure 3.15.

Interruption of the ISJ causes an increase in CAP thresholds in both the unoccluded and occluded ear. Thresholds are increased by 4 to 5 dB in the unoccluded ear at frequencies below 2 kHz, while the thresholds are increased by 8 to 10 dB in the occluded ear across the same range of frequencies. The effect of the ISJ interruption on CAP thresholds decreases above 2 kHz and begins to increase again above 4 kHz, peaking at 6.2 kHz, and again decreasing above this frequency. Above 4 kHz, the effect of the ossicular discontinuity is similar for the open and occluded ears.

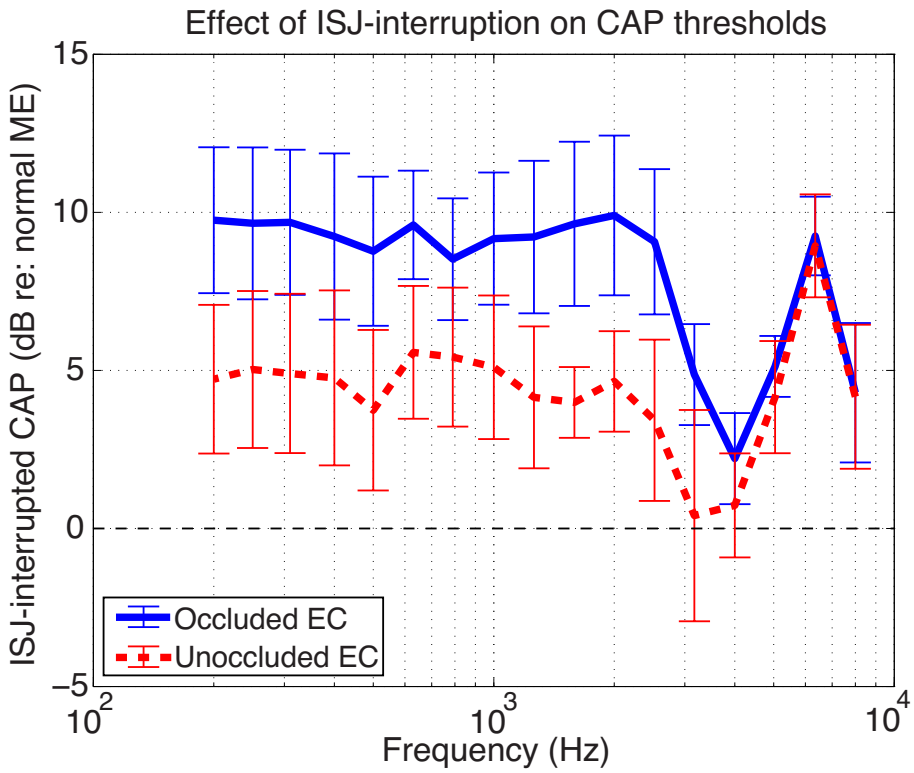

Figure 3.14. Effect of ISJ interruption on CAP thresholds.
Effect of ISJ-interruption on BC-inducted CAP thresholds in the occluded (n = 5) and unoccluded (n = 6) ear canals. Error bars represent ±1 standard error.

Figure 3.15 indicates that occlusion of the ear canal results in no significant change in CAP thresholds while the ISJ is interrupted. In the normal ME, however, CAP thresholds are higher in the unoccluded state. An increase of 5 dB occurs at 1.5 kHz, an increase of approximately 3 dB is seen between 200 Hz and 500 Hz, and more modest increases occur at all other frequencies. The results in Figure 3.14 and Figure 3.15 indicate ISJ interruption effectively isolates the external and inner ears, and that even in the unoccluded normal ear EEBCs introduce sound pressures that can lower the threshold to BC stimulation of the head.

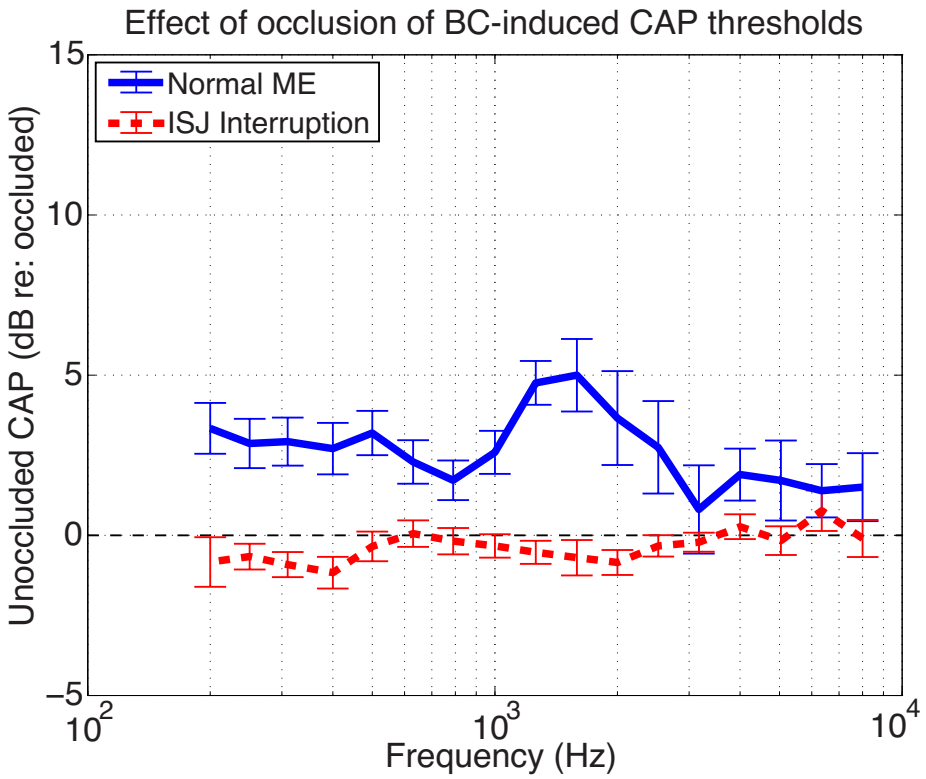

Figure 3.15. Effect of EC occlusion on CAP thresholds.
Effect of ear canal occlusion on BC-induced CAP thresholds in chinchillas with normal middle ears (n = 7) and ISJ-interrupted ears (n = 5). Error bars represent 1 standard error.

IV. Discussion

A. Isolation of EEBCs from BC-induced ECSPs

Our characterization of EEBCs in terms of volume velocities, produced by compressions and expansions of the cartilaginous and bony ear-canal walls, depends on ECSP measurements and modeled ear-canal and ME impedances, and assumes that no other bone-conduction related sources contribute to BC-induced ECSPs. To test this assumption, we assume interruption of the ISJ removes the effect of any inner-ear BC sources on the measured ECSP, while fixation of the MI reduces any contribution of ossicular inertia and TM motion to the BC-induced ECSP.

Single-source EEBC magnitude and phase estimates are shown for the normal, ISJ-interrupted, and MI-fixed middle ear in Figure 3.9A and B. The great similarity of the estimates made in the different middle-ear conditions (Figure 3.9A and B) is consistent with the ear-canal sound pressure in BC being dominated by the EEBCs, though the existence of some differences in the source estimates are consistent with a small contribution of middle- or inner-ear sources to ECSP in BC.

Some of the observed differences in Figure 3.9A and B may have another cause. The estimates of the EEBCs under the different middle-ear conditions also depend on knowledge of the middle-ear input impedances $\mathbf{Z_{ME}}$. We used a model of the middle ear (Bowers and Rosowski, 2019) to define those impedances, where the model was explicitly fit to measurements of the normal $\mathbf{Z_{ME}}$, in circumstances (tensor-tympani cut, two middle-ear cavity openings) very similar to those used in these measurements. We therefore expect a good correspondence between the model $\mathbf{Z_{ME}}$ and the $\mathbf{Z_{ME}}$ present in the normal ears in our test population. The $\mathbf{Z_{ME}}$ with the ISJ interrupted is a model prediction based on removing the influence of the stapes, annular ligament and inner ear from the model, where these three structural components and their connection to the rest of the model are well characterized and fairly simple, and there is good reason to expect that $\mathbf{Z_{ME}}$ in the IJS-interrupted state is fairly well defined by the model. The model's definition of the governing structures and their circuit location and description in the fixed MI case are less well defined, and therefore $\mathbf{Z_{ME}}$ in the MI-fixed case is less certain, and the meaning of differences between source estimates based on the MI-fixed condition and the other middle-ear states is less clear. In light of these uncertainties, the great similarity of the predicted source strength in the case of the normal and ISJ-interrupted middle-ear conditions points to the presence of little if any contribution to BC-induced $\mathbf{P_{TM}}$ from

the inner ear, and the small but significant differences between the EEBCs predicted for the MI-fixed and normal states may be the result of either some small contribution of the ossicles and TM motion to ECSP or errors in model predictions of $\mathbf{Z_{ME}}$ in the MI-fixed case (Figure 3.8B).

B. Effect of ear canal occlusion on source estimate

If our initial model of EEBC as a single source unaffected by ear-canal occlusion was correct (i.e., the source is constant under the two conditions), the pressure and impedance loading the source would change proportionally (Equations 3.2 and 3.3) and the source computed for the occluded and unoccluded ears would be the same. The observed differences in source estimates (Figure 3.10) suggest the presence of a more-distributed external ear source, which separates the bony and the cartilaginous canal sources, and whose outputs sum in the unoccluded condition. This led to our inclusion of a second source BC-related volume-velocity source due to compression of the cartilaginous ear canal. Comparisons of the occluded and unoccluded source estimates suggest the source in the unoccluded condition is of larger magnitude when compared to the source computed for the occluded condition (Figure 3.10).

C. Two-source representation of EEBC

In defining our two-source model, we identify $\mathbf{U_{bone}}$ as bounded by the boney walls of the canal, and we base our estimates of this source on $\mathbf{P_{TM}}$ measurements and model impedances in the occluded case (Figure 3.9B), where the occlusion removes any contribution of the cartilaginous ear canal (Figure 3.5B). The definition of $\mathbf{U_{cart}}$ depends on model impedances and the sound pressure difference between $\mathbf{P_{TM}}$ measured in the unoccluded ear and estimated $\mathbf{P_{TM}}$ resulting from $\mathbf{U_{bone}}$ in the unoccluded condition. While the $\mathbf{U_{cart}}$ we have defined is of larger magnitude than $\mathbf{U_{bone}}$ (Figure 3.11), the sound pressures measured in the occluded condition,

when only $\mathbf{U_{bone}}$ is active, is larger in magnitude than in the unoccluded state at many frequencies (supplemental Figures B.4A & B). The difference in the observed sound pressures occurs because much of the sound energy produced by both of these sources in the unoccluded ear is shunted out the open ear canal away from the middle ear, similar to the low-pass filter action described by Tonndorf (1966).

The difference in magnitude between the two sources may result from differences in the area of the bony and cartilaginous canal walls as well differences in the rigidity and mass of the walls: the less-impedant cartilage walls may move more in response to head vibration. The increased motion of cartilage vs. bony walls was intuited by Békésy (1932); though he suggested the bony walls of the human ear canal were so stiff that $\mathbf{U_{bone}}$ would approximate 0. This is clearly not the case in our measurements in chinchillas, where one difference may be the relatively thin bone of the chinchilla ear canal. The complete lack of mobility of the human ear-canal bone was questioned by Stenfelt et al. (2003) who were able to produce BC-induced ear-canal sound pressures in human ear canals with deep canal plugs.

D. Other potential sources of ECSP

1. Effect of lower-jaw motion on BC hearing

Bone-conduction induced ECSPs were measured in the ISJ-interrupted unoccluded ear, with the lower jaw intact and with the portion of the jaw nearest the ear canal resected, along with nearby connective tissue between the lower jaw and the skull. Comparison of these 2 ECSPs are shown in Figure 3.13. The sound-pressure magnitudes are not significantly different between the two conditions. The results suggest relative jaw motion does not play a significant role in BC

hearing in the chinchilla, and any sound pressure generated by relative jaw motion appears smaller than the sound pressure produced by other EEBCs.

2. Motion of the occlusion plug

Some fraction of the ECSPs we measured could also result from motion of the earplug used to occlude the canal. In one ear, the volume velocity generated by motion of the occluding plug was estimated by measuring the velocity of the plug, in the direction of the canal's longitudinal axis, and by multiplying this velocity by the cross-sectional area of the canal. The estimated volume velocity produced by motion of the occluding plug is more that 40 dB down from the ear-canal source estimates across all frequencies, suggesting that the measured $\mathbf{P_{TM}}$ used for estimating the canal sources are unaffected by motion of the occlusion plug.

3. BAHA-induced airborne sound

Sound-pressure measurements were made at the TM and at the entrance to the bony canal, while the BAHA was either coupled to or detached from the head. In both cases, the body of the BAHA was kept in the same location, relative to the location of ECSP measurements, in both cases. The ECSPs were compared to determine whether the measured sound pressure is dominated by BC mechanisms or airborne sound radiated from the BAHA (supplemental Figure B.5). The $\mathbf{P_{TM}}$ in the coupled case was greater in magnitude, across all frequencies, than when the BAHA was uncoupled, with the difference generally being larger than 20 dB.

D. Contribution of EEBC to BC hearing

The sensations of sound associated with bone conduction are hypothesized to be the result of a summation of contributions of multiple sources, including ear-canal compression, relative motion of the ossicles and the petrous bone, and inner-ear sources related to fluid inertia,

cochlear-wall compression, and third-window connections between the cranial cavity and the inner ear. We assessed the contributions of external and middle-ear sources to BC hearing by looking at how ear-canal occlusion and the interruption of the ISJ affects CAP thresholds in our preparation. However, it should be noted that changes in thresholds cannot be absolutely attributed to removal of BC sources lateral to the cochlea, as ossicular discontinuity and fixation alters the loading impedance on the inner-ear sources, and can therefore modulate the intracochlear sound pressure produced by such sources (Chhan *et al.*, 2016a).

Comparison of thresholds between the 2 conditions of the ME were performed with the ear canal open and occluded. ISJ interruption results in a 5 to 10 dB increase in CAP thresholds below 2.5 kHz, with the larger magnitude observed when the EC is occluded. Little change is seen around 4 kHz in either case, and CAP threshold increases above this frequency are similar for the open and occluded ear. Since this increase in threshold is most apparent at frequencies less than 2.5 kHz, where we might expect the contribution of ossicular inertia to be small, this suggests the EEBC is a significant contributor to BC sensitivity in the chinchilla whether the ear is occluded or not.

Changes in the differential sound pressure **ΔP** across the cochlear partition at the basal end of the basilar membrane approximates the change in acoustic stimulus to the organ of Corti (Olson, 1999; Nakajima *et al.*, 2009). Chhan et al. (2013) compared **ΔP** in the normal and ISJ-interrupted ears, with occluded EC, to investigate the potential contribution of the external and middle-ear sources of BC to hearing. Interruption of the ISJ caused a 5 to 10 dB decrease in **ΔP** at frequencies below 3 kHz. A similar effect is seen in changes to CAP thresholds in the data presented here. The mean data shows a relatively constant 10 dB threshold increase after ISJ-

interruption at frequencies below 2 kHz; however, the individual chinchilla thresholds show similar variability to the **ΔP** data of Chhan et al. (2013).

Effect of ear-canal occlusion on CAP thresholds in the normal ear are in agreement with **ΔP** data from Chhan et al. (2016b) below 3 kHz; occlusion of the canal results in an increase in cochlear drive during BC stimulation. Above this frequency range, the cochlear pressure differential decreases, while the data presented here suggests **ΔP** would increase, albeit to a smaller degree compared to the change at lower frequencies.

E. Comparison to humans

The dominant contribution of EEBCs to BC-induced ECSP, as suggested by results shown in Figure 3.9A, agrees with results of BC experiments performed in human. Stenfelt et al. (2003) compared the BC-induced ECSP and ECSP resulting from reverse stimulation of the ossicles (results were normalized by relative motion between the umbo and the tympanic ring). Their results suggest that TM motion does not contribute significantly to ECSP during BC stimulation, and can be extended to suggest an insignificant contribution of ossicular inertia to the ECSP as well. Earlier experiments by Tonndorf (1976), in which the BC-induced ECSP was measured before and after TM removal, support the hypothesis that neither TM motion, nor the middle and inner ear BC sources contribute to the measured ECSP.

The effect of occlusion in chinchilla with a normal ME is an approximately 5 dB to 10 dB increase in ECSP at frequencies below 2.0 kHz (Figure 3.7). An increase of 10 dB to 20 dB has been shown in cadaver heads (Stenfelt *et al.*, 2003). Above this frequency, the two-studies show similar effects at frequencies associated with the resonances of the open or closed canal. A negative effect is seen at approximately 2.5 kHz to 3 kHz due to the quarter wavelength

resonance in the open canal. There is an upward trend above this frequency that does not quite reach a positive effect and may be associated with the half wavelength resonance of the occluded ear. A comparison is made between the modeled occlusion effect in chinchilla, where the effect of the cartilaginous portion of the ear canal is removed, and the measured occlusion effect in human cadaver heads that have the same ear-canal manipulation (supplemental Figure B.6)—the normal ear condition is included. A reduction in the occlusion effect is seen in both the chinchilla (n = 3) and human ear canal after the cartilaginous portion of the canal is removed at frequencies below approximately 1.5 kHz. An increase is seen in the effect in chinchilla after resection of the canal between 2 kHz and 3 kHz, which may be due to the shift of the open-canal quarter-wavelength resonance to a higher frequency.

Resection of the chinchilla lower jaw did not produce a significant change in ECSP (Figure 3.13). This result supports the hypothesis that relative motion between the lower jaw and ear canal does not contribute to BC hearing, as has been suggested by others (Allen and Fernandez, 1960; Stenfelt 2003). However, unlike the human, the jaw joint in the chinchilla is much smaller in absolute size and relatively more distant from the cartilaginous canal.

The effect of the EEBC on BC hearing in chinchilla was investigated by comparing CAP thresholds before and after interruption of the ISJ. Thresholds increase by approximately 10 dB below 2.5 kHz in the occluded ear-canal condition after ISJ interruption, while thresholds increased by approximate 5 dB, below the same frequency, in the open ear-canal condition after interruption (Figure 3.14). The contribution of the EEBC to BC hearing in human was investigated by Stenfelt et al. (2003) by comparing umbo velocity relative to ECSP level (ME input admittance) in response to AC and BC stimulation. Their results suggest the EEBC can contribute to BC hearing between 0.4 and 1.2 kHz when the ear canal is occluded, but would not

in the open-canal condition. This differs from our results in that (under the assumption that the change in CAP threshold is not due to a change in inner-ear BC source-loading and is instead due to the removal of the EEBC) the EEBC contributes to BC hearing in both the occluded and unoccluded ear canal conditions. The lack of effect of loading conditions is based on results by Chhan et al. (Chhan *et al.*, 2016b), in which both stapes fixation and ISJ-interruption result in a decrease in ΔP.

Stenfelt et al. (2003) further investigated the effect of occlusion on BC hearing by comparing the changes in umbo velocity and ECSP after occlusion of the ear canal. Their results show a smaller increase in umbo velocity after the ear canal is occluded, compared to the increase in ECSP at frequencies below 2 kHz. The positive increase in umbo velocity occurs between 400 Hz and 1 kHz and is almost 10 dB lower magnitude in maximum positive change compared to that of sound pressure (700 Hz). A similar result is seen in chinchilla; the maximum positive increase in ECSP is approximately 10 dB, compared to the 5 dB maximum decrease in CAP threshold (1.5 kHz).

The estimated contribution of the cartilaginous source to the ECSP at the TM is greater than that of the bony-canal source at frequencies below 0.9 kHz, and between 2 and 3 kHz in the unoccluded, normal chinchilla ear (Figure 3.11). Above 3 kHz, neither source dominates, with the exception of at 5 kHz, where $\mathbf{U_{bone}}$ dominates, due to a minimum in sound pressure produced by the cartilaginous canal source. Stenfelt et al. (2003) measured ECSP at the TM relative to umbo velocity in the normal open ear, and open ear in which the cartilaginous portion of the canal was removed. The measured ECSP was greater in the normal ear below 1 kHz, but the sound pressure was similar between the two cases above this frequency, suggesting the source of the bony canal is of significance to the BC-induced ECSP above 4 kHz in human. Further

support for this hypothesis can been seen in the changes in CAP thresholds due to ISJ interruption (Figure 3.14). Above 4 kHz, there is no difference in CAP thresholds when comparing the threshold change in the open and occluded ears.

V. Conclusion

The external-ear bone-conduction source was first estimated as a single volume-velocity point-source located near the TM. Estimates of the EEBC, in the unoccluded ear-canal condition, in various states of the middle ear suggest the inner and middle-ear BC sources do not contribute to the measured $\mathbf{P_{TM}}$ induced by BC stimulation, with the exception of a limited frequency range, between 3 and 4 kHz. Therefore, our estimates of the EEBC in the normal ear are valid in the sense that the estimate is dependent upon the measured $\mathbf{P_{TM}}$ and our impedance model alone. Additionally, estimates of the EEBC with the lower jaw intact and resected reveal that relative motion of the jaw does not contribute to the measured $\mathbf{P_{TM}}$ during BC stimulation.

Differences in source estimates of the open and occluded ears, namely a greater magnitude in the unoccluded ear at frequencies below 3.5 kHz, suggest that occlusion of the canal removes contribution of compression and expansion of the cartilaginous canal to the BC-induced ECSP; although the cartilaginous canal is not contained within the chinchilla head, as it is in human, it still plays a role in BC hearing in this animal.

The EEBC was separated into 2 point-sources to model volume velocities produced by the bony and cartilaginous canals separately. The estimated magnitudes of these sources estimates suggest the volume velocity produced by motion of the EC cartilage is greater than that of the bony canal, by approximately 10 to 15 dB below 4 kHz. Above this frequency, the magnitudes of the two sources are similar. In the unoccluded ear, both sources contribute to the BC-induced

sound pressure at the TM, with the cartilage source dominating at frequencies below 0.9 kHz. Our model suggests that as in human, the amount of EEBC-related sound energy that stimulates the middle and inner ear in the unoccluded ear canal is reduced by the low-pass action of the open canal, as suggested by Tonndorf (Tonndorf, 1966).

Comparison of bone conduction CAP thresholds before and after interruption of the ISJ suggests that the EEBC contributes to BC hearing across a wide range of frequencies in both the occluded and unoccluded case. Occlusion of the ear canal decreases the output to the BAHA required to reach threshold, by up to 5 dB.

Differences in anatomy between human and chinchilla prompt caution when attempting to directly relate our results to BC hearing in human, however, our definition of EEBCs associated with the expansion and compression of the bony and cartilaginous canals is consistent with Stenfelt et al. (2003) description of reduced but measurable sound pressures within the deeply occluded human ear canals.

CHAPTER 4. A method for characterizing the inner-ear sources of bone-conduction stimulation in chinchilla

I. Introduction

Vibrations of the head can be transmitted to the cochlea by non-ossicular pathways, generating relative motion between the cochlear fluids and walls. It is widely accepted that such relative motions can result from compression and expansion of the cochlea and inertia of the cochlear lymph. The intracochlear sound pressures generated by this fluid motion can displace the cochlear partition, producing traveling waves along the basilar membrane. Head vibrations may also produce sound pressures within the brain, which can be transmitted to the inner ear via the vestibular and cochlear aqueducts, as well as the perineural and perivascular channels. These cochlear-cranial connections are collectively referred to as third-window pathways [see Tonndorf (1972), who cites Ranke (1953) as the source of this nomenclature]. The relative contributions of cochlear compression, fluid inertia or the third-windows to bone-conduction hearing in the normal and pathologic ear are not at all clear.

Retjö (1914) suggested the inner ear could directly receive acoustic energy from vibrations of the skull, and the theory was described further by Herzog and Krainz (1926), who coined the term *compression mode* of bone conduction. These compressive forces acting on the cochlear walls produce alternating compressions and rarefactions of the cochlear space, which occur even though the fast wave speed through the cochlear bone does not allow any phase differences across the cochlea. As the cochlear fluid is effectively incompressible, these volume changes in the cochlear capsule cause displacements of the cochlear fenestra. The unequal compliances of the oval and round windows as well as the asymmetry of the scalae result in sound pressure differences across the cochlear partition that stimulate the inner ear sensory apparatus.

Inertia of the cochlea fluids is also thought to play a role in bone-conduction hearing, although its contribution relative to cochlear compression is still debated. Kirikae (1959)

suggested that the data supporting compression of the cochlear walls was insufficient and that fluid inertia must play a role in BC hearing. Brinkman et al. (1965) hypothesized that both ossicular and fluid-inertia components play the biggest role in BC hearing across all frequencies. More recently, Stenfelt (2015) suggested that in the normal human ear, fluid inertia dominates BC hearing up to 10 kHz, but that in the case of oval-window immobilization, cochlear compression may dominate at frequencies as low as 1 kHz.

Conceptually, it is possible to effectively enhance or reduce the contribution of different BC components to cochlear stimulation by performing certain manipulations of the ear (e.g. window fixation); however, these same manipulations could alter the behavior of the remaining sources. For this reason, researchers have turned to models to characterize different inner-ear stimulus components. Bohnke and Arnold (2006) first used finite element analysis to study the effect of cochlear-window manipulation on basilar membrane displacement; their use of a homogeneous pressure encompassing the boundary of the cochlea would best model the cochlear compressional component. Kim et al. (2011) used a sinusoidal translation imposed on a finite element model of an uncoiled cochlea to study the inertial component of cochlear stimulation. Their results support the theory that basilar-membrane motion is driven by a difference in cochlear window velocities. Kim et al. (2014) extended this study with a coiled model of the cochlea, with the results suggesting differences in scala volumes, particularly in the hook region of the cochlea, are important to the generation of asymmetric cochlear-window volume velocities.

Others have developed models to address multiple BC components of the inner ear. Schick (1991) developed an electrical model to study cochlear compressional and inertia components, and to investigate the effect of middle-ear pathologies on BC-induced basilar-membrane motion.

The model permitted estimation of sound pressures along the basilar membrane, where large differential pressures produce large displacements of the cochlear partition. The contribution of each of the model sources to such displacements was estimated. Stenfelt (2015) stressed the importance of excitation type, arguing that in-phase (inertial driven motion) and out-of-phase (compressive) cochlear wall motion would occur during BC stimulation. With that, he developed a lumped-element circuit of the cochlea, including sources for both the inertial and compressional component. Stenfelt used a simple model of wave propagation along a linearized cochlear geometry with specific boundary conditions to characterize the relative magnitude of his inertial and compressive sources, where the magnitude of the inertial component is dependent upon the in-phase, or "common" motion of the cochlear boundaries while that of the compressional component is dependent on out-of-phase, or "differential" motion of the boundaries.

In this chapter, we propose a relatively simple cochlear circuit analog that includes sound pressure and volume-velocity sources to model different inner-ear stimulus components in BC hearing. The model is an extension of that defined in Chapter 2, and is a starting point for further study. Intracochlear sound pressures measured in the live chinchilla under various conditions of the ear described here and in earlier work (Chhan et al. 2013; 2016) are used to characterize the sources. A major difference between the study presented here and previous models is that sources in those models were estimated from some intuition of process: while we utilize an intuitive placement of the different sources within the cochlea, we characterize their output magnitudes and phases from measurements of intra-cochlear sound pressure. As a result, in our model, it does not matter if stimulation of the cochlea is due to phase differences along a longitudinal pressure wave across the cochlea, or a pressure difference across the cochlear

boundary, so long as the representative sources produce the appropriate responses in all conditions of the ear. That being said, we still make assumptions concerning the sources' type (pressure or volume velocity), their placement within the model, and the conditions under which these sources are active.

II. Methods

A. Animal preparation

In one set of measurements, vibration-induced intracochlear sound pressure were measured in live chinchillas prepared as described in Chapter 3, in regard to anesthesia, tracheal cannulation, severing of tensor tympani, and attachment of BAHA post to the skull. In addition, a ~ 0.25 mm diameter hole was placed in the bone of the superior medial wall of the vestibule, which was accessed by exposing and removing a small part of the paraflocculus of the cerebellum. A second hole was made in the petrous bone over the scala tympani at about 1 mm apical to the round window. In a second set of measurements, vibration-induced intracranial sound pressures were measured in cadaveric chinchilla heads. These specimens were from earlier experiments in which at least one ear was still completely intact. In these cases, no cochlear fenestrations were performed, but intracranial sound pressures were measured via an opening made in the skull.

B. Intracochlear sound-pressure measurements

Intracochlear sound pressures were measured using fiber-optic pressure sensors (Olson, 1999). Prior to their insertion into the ear, the sensors were calibrated as described in previous work (Olsen, 1999; Nakajima et al.; Ravicz et al. 2012) and were recalibrated after

measurements to check sensor stability. Intracochlear sound pressures were measured within the vestibule and the scala tympani near the round window via the holes described above.

Once each sensor was positioned for recording intracochlear sound pressures, Jeltrate® and dental cement were used to seal the space between the cochlear bone and the sensor to minimize relative motion (Chhan et al. 2016). In order to standardize measurements across animals and different experiments, the measured sound pressures were normalized by the simultaneously measured skull velocity, unless otherwise noted. The velocity was measured as described in Chapter 3.

C. Intracranial sound-pressure measurements

Intracranial sound-pressure measurements were recorded in cadaveric chinchillas. Calibration of the pressure sensor was performed in the same manner as described for intracochlear sound-pressure sensors; however, customized "off-the-shelf" sensors (FISO Technologies Inc.) were used. A 1 mm diameter hole was drilled into the top of the skull of frozen cadaveric heads, approximately 1 cm in front of the BAHA post. Through the skull hole, a hole of the same diameter and 5 mm depth was drilled into the frozen brain. The specimen was then allowed to thaw, after which the removed column of brain was filled with water. A pressure sensor was placed within the water column 3 mm deep and sealed in place. The intracranial BC-induced sound-pressure measurements were also normalized by simultaneous skull velocity measurements.

D. The cochlear model

Different bone-conduction cochlea models were based on the air-conduction model of Chapter 2 and the detailed cochlear anatomy of a single ear. The modified cochlear networks

included elements describing the vestibular and cochlear aqueducts, and additional components describing the distributed mass of the scala vestibuli, scala tympani, and scala media.

1. 3D structures of the cochlea and middle ear

A 3D reconstruction of the cochlea and middle ear was generated from the microCT scans of Chapter 3, using Amira software. In Figure 4.3A and B, the cochlea is segmented such that the vestibule, the superior, posterior, and horizontal semicircular canals, scala vestibule, scala media, scala tympani, vestibular aqueduct, and cochlear aqueducts are differentiated. These segments represent the spaces contained within the cochlear bone. The illustrated ossicles, on the other hand, represent the volumes of the bones. The vestibular and cochlear aqueduct boundaries are highlighted in white in Figure 4.3A and B, respectively. The vestibule segments include the wider end limbs and the ampullae of the semi-circular canals.

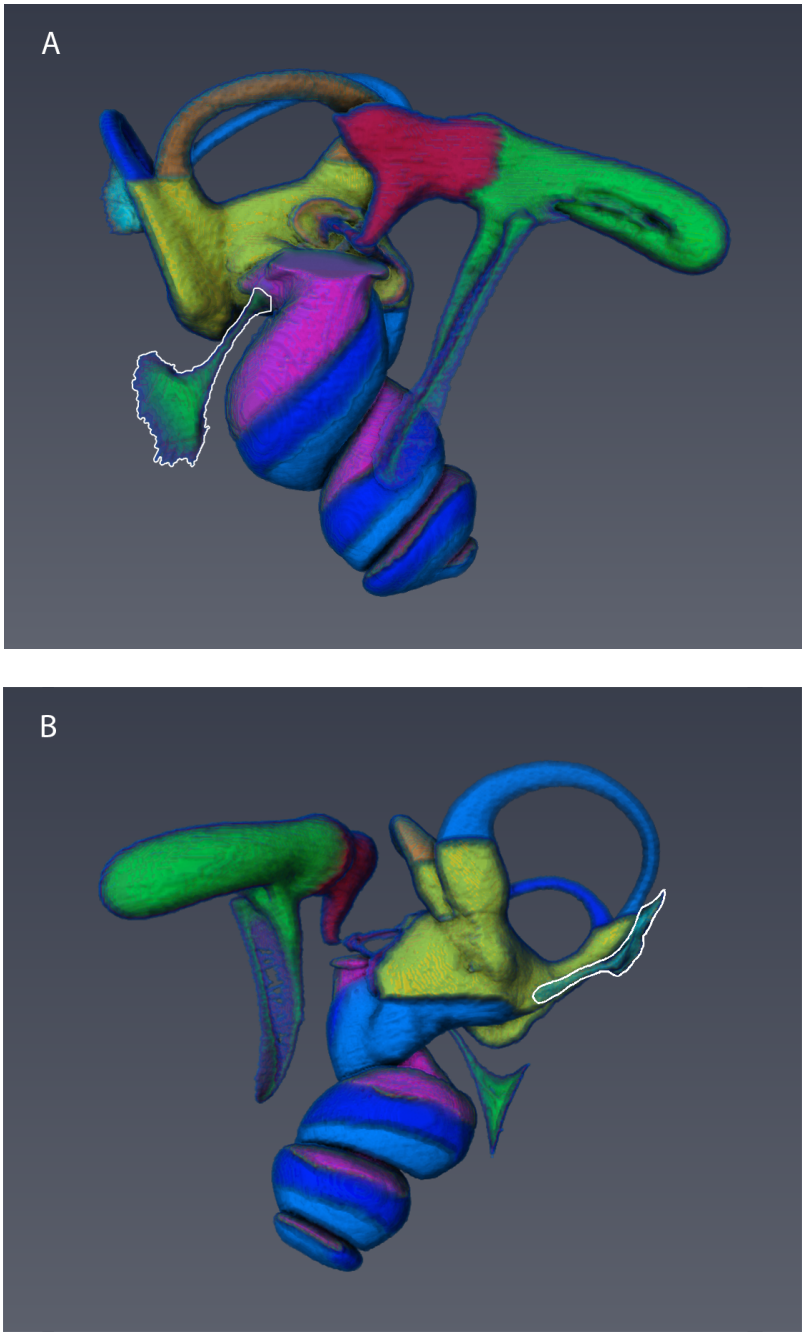

Figure 4.3. 3D reconstruction of chinchilla inner ear from microCT.
(A) Lateral-medial and (B) anterior-posterior views of the reconstructed chinchilla middle ear and cochlea. The cochlear aqueduct (A) and vestibular aqueduct (B) are highlighted in white. The ossicles are coded in different colors: green, the head of the malleus; blue, the manubrium of the malleus; gold, the stapes footplate; red, the incus. The vestibule and semicircular canals are coded by: yellow, the vestibule and parts of the semicircular canals; the three semi-circular canals are in gold, cyan and blue. The components of the coiled cochlea include: the scala vestibuli in magenta, the scala media in blue, and the scala tympani in cyan.

2. Vestibular and cochlear aqueducts

The vestibular aqueduct and cochlear aqueduct connect the fluid spaces of the inner ear to the cranial cavity (Rosowski *et al.*, 2018). The vestibular aqueduct, also known as the endolymphatic duct, forms a communication between the endolymph-filled utricle in the vestibule and the endolymphatic sac, which is situated between the dura mater layers on the medial surface of the petrous bone. The cochlear aqueduct is a perilymph-filled channel between the scala tympani, where it opens near the round window, and the cerebrospinal fluid-containing subarachnoid space.

The geometries of the vestibular and cochlear aqueducts were determined from the microCT scans from our sample ear described in Chapter 3. These geometries were approximated by a concatenation of conical horns; and the impedances of the aqueducts were estimated using the lossless equations describing the ear-canal impedances in the Chapter 3 (Equations 3.4-3.10), using the density, viscosity, and speed of sound of water. Each aqueduct was terminated at the cranial entrance by a compliance of 7.39e-16 m^3/Pa, based on an average chinchilla brain mass of 1.7e-3 kg (Sultan and Braitenberg, 1993) and volume of 1.7 cc.

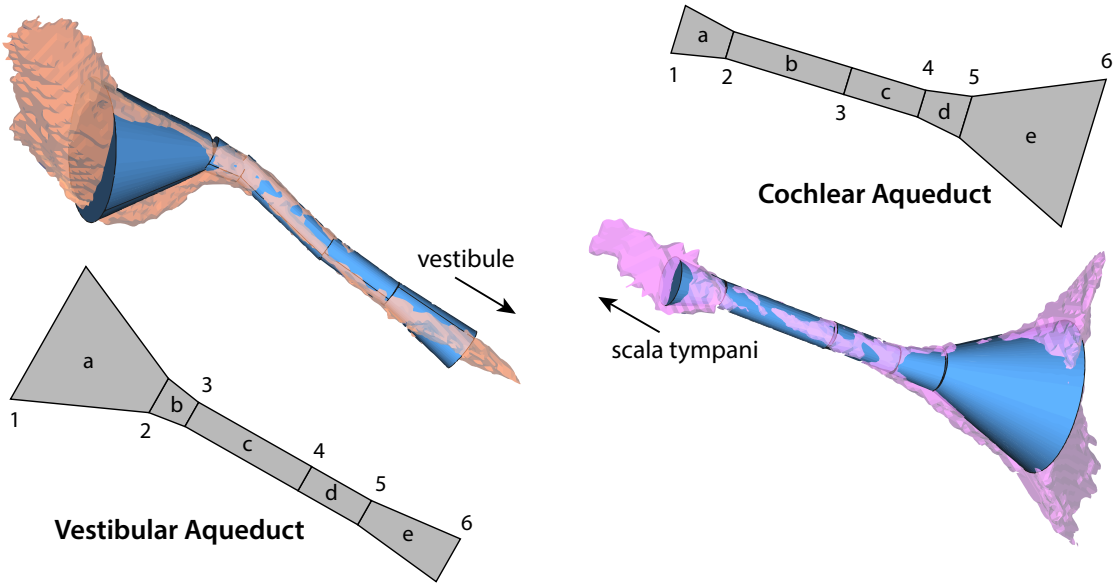

x-sectional area (mm^2)
1=1.571, 2=0.106, 3=0.055, 4=0.051,
5=0.055, 6=0.106,

length (mm)
a=0.83,b=0.25, c=0.85, d=0.55, e=0.63

x-sectional area (mm^2)
1=0.161, 2=0.055, 3=0.051, 4=0.055,
5=0.161, 6=1.571,

length (mm)
a=0.63,b=0.80, c=0.50, d=0.30, e=0.80

Figure 4.4. Vestibular- and cochlear-aqueduct geometries.
The vestibular and cochlear aqueducts were reconstructed in 3D using microCT images of the chinchilla ear. Both aqueducts were modeled as a series of conical horns.

3. Cochlear scalae

The geometries of scala tympani, vestibuli, and media were also determined from the microCT images. The absence of a clear Reissner's membrane or basilar membrane in the images made it difficult to determine the separation between the compartments, and so this distinction was somewhat subjective, and guided by histological sections from the temporal-bone collection at the Massachusetts Eye and Ear. The resultant volumes and average areas of the

scalae (volume divided by a cochlear length of 18.4 mm (Eldredge *et al.*, 1981) are listed in Table 4.1.

Table 4.1. Cochlear-scalae geometries
†Average of the combined scala vestibuli and tympani were determined by the combined volume divided by the average cochlear length

	Volume (mm^3)	Area (mm2)
Scala vestibuli	11.18	0.608
Scala media	3.58	0.195
†Scala vestibuli + scala media	14.76	0.802
Scala tympani	10.53	0.572

The modeled cochlear spaces were simplified by combining the volumes of the scala vestibule and scala media, under the assumption that Reissner's membrane imposes little impedance between the two fluid spaces. The ratio of the volumes (and areas) of the scala vestibuli to scala tympani is 1.06, while the ratio of the volumes (and areas) of the scala vestibuli plus scala media to scala tympani is 1.4. In human, the volume and area ratios of scala vestibuli to scala tympani are approximately 1.66 and 1.5 (Tonndorf, 1972).

The combined space of the scala vestibuli and scala media, as well the scala tympani, were modeled as an inductor and a resistor in series, valued according to Equations 4.1 and 4.2, respectively:

$$L_{scala} = \rho l / S^2 \tag{4.1}$$

$$R_{scala} = 8\eta l / \pi a^4 \tag{4.2}$$

where l is the length of the cochlea, S is its average cross-sectional area, a is the average radius; the density (ρ) and viscosity (η) of the lymph were approximated to be that of water.

4. Network topology

The cochlear network of the BC model is shown in Figure 4.5. The placement of the inner ear BC sources requires additional sound transmission pathways not relevant to air-conduction. In air-conduction, the cochlear input impedance is dominated by the input impedance of the distributed cochlear mass and stiffness (Z_{RC}, Zwislocki 1965). A more distributed cochlear impedance is usually used in bone-conduction models of the inner ear, particularly a model that distributes the mass of the fluid that moves with cochlear compression or inertia (e.g. Schick 1991; Stenfelt 2015, 2016). We make a first attempt at a combined lumped-distributed cochlear model for BC that accounts for fluids displaced by compressive or inertial forces, and at the same time maintains the normal cochlear input impedance to describe the sound pressure difference across the cochlear partition. More complicated models that also account for the distributed stiffness of the cochlear partition are part of future plans. The elements describing the masses of the scalae fluids are contained within a branch parallel to the resistance of the cochlear partition. Additionally, branches of the vestibular and cochlear aqueducts are included to allow sound pressure transmission between the inner ear and the brain cavity, and which will also act as important transmission pathways for the compressional and inertial components of BC when the stapes is fixed and/or the round window is occluded.

The inner ear BC sources we consider are also illustrated in Figure 4.5. The pressure source $\mathbf{P}_{\mathbf{cranial}}$ models a hypothesized uniform intracranial sound pressure defined by our measurements. The sound pressures produced by inertial forces are modeled as an ideal pressure source $\mathbf{P}_{\mathbf{inertia}}$, and two ideal volume velocity sources $\mathbf{U}_{\mathbf{comp1}}$ and $\mathbf{U}_{\mathbf{comp2}}$ describe the compression related changes in the volumes of scala tympani and vestibuli. A similar association of inertial forces

with pressures sources and compression with volume-velocity sources was made by Stenfelt (Stenfelt, 2015; 2016).

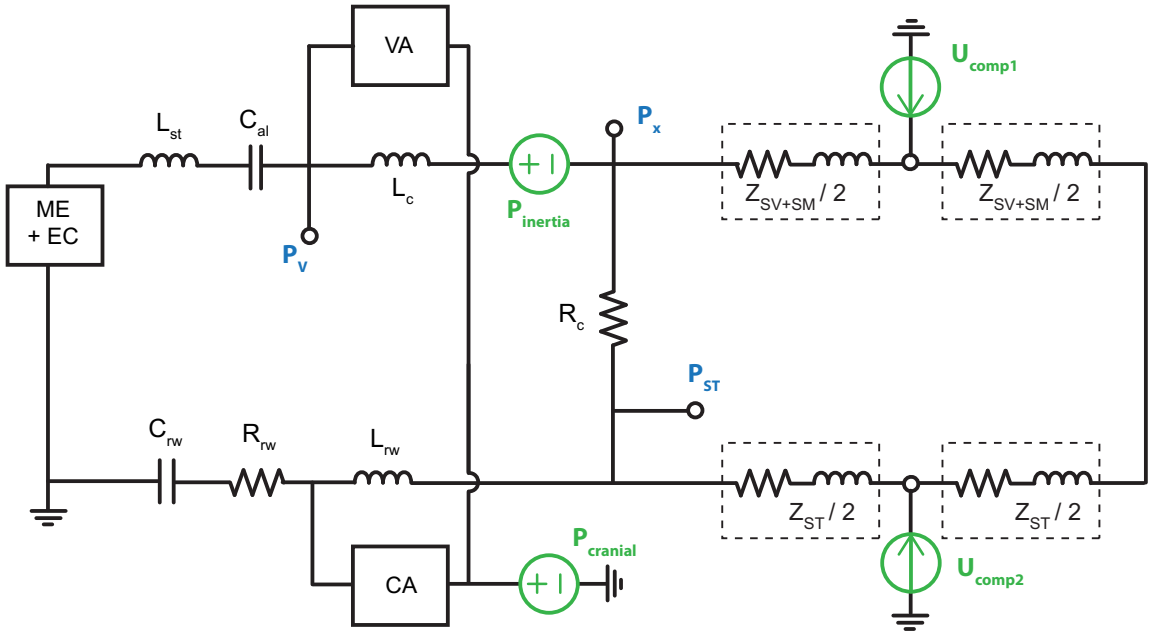

Figure 4.5. Complete circuit diagram of inner ear including its bone-conduction sources. Each block represents a collection of circuit elements (e.g. ME+EC – middle ear and ear canal, SV+SM – scala vestibuli and media, ST – scala tympani) or transmission matrices (e.g. VA – vestibular aqueduct, CA – cochlear aqueduct).

F. Inner-ear BC source estimates

1. Third-window sound-pressure transmission

The pressure source $\mathbf{P_{cranial}}$ of Figure 4.5 model BC-related sound pressures within the brain that stimulate the inner ear. This source is characterized by the mean sound pressure measured within the brain, during BC stimulation. A later results section will show that the contribution of this pressure source to inner-ear sound pressures is generally small over the frequency range of our measurements (0.25 to 8 kHz).

2. Compressional sources

Compression of the cochlear walls is modeled by two volume-velocity sources ($\mathbf{U_{comp1}}$ and $\mathbf{U_{comp2}}$) that model changes in the volume of the cochlear scalae (Figure 4.5). Two sources were used to better model complex relative motions between opposite cochlear walls. In order to characterize these sources we assumed that measurements of BC-induced inner-ear sound pressures, made when the oval and round window were both occluded (*BWx*), were dominated by the two compression sources, as any external or middle-ear contribution to the sound pressures are removed by immobilizing the stapes, and the reduced motion at the windows would decrease any inertial source contributions (Kim *et al.*, 2011). A simplified cochlear network containing only the compressional sources is shown in Figure 4.6.

In this simplified model $\mathbf{P_V}$ and $\mathbf{P_{ST}}$ are the measured sound pressures in the vestibule and scala tympani. $\mathbf{P_X}$ is the pressure in the scala vestibuli at the basal end of the cochlear partition. $\mathbf{Z_{Lc}}$ is the impedance of the fluid between the location of $\mathbf{P_X}$ and that of the pressure sensor within the vestibule. The impedances of the scala vestibuli and scala tympani are divided, with half of each represented as $\mathbf{Z_2}$ and $\mathbf{Z_3}$, respectively. The remaining scala-associated impedances are summed together as $\mathbf{Z_1}$. The resistance of the cochlear partition is $\mathbf{Z_4}$. With the stapes and round window immobilized in the *BWx* condition, $\mathbf{Z_5}$ is the impedance of the vestibular aqueduct, and $\mathbf{Z_6}$ is the impedance of the cochlear aqueduct, placed in series with the impedance of L_{rw}; values of $\mathbf{Z_5}$ and $\mathbf{Z_6}$ may differ depending on the condition of the ear.

The estimated $\mathbf{P_V}$ and $\mathbf{P_{ST}}$ induced by the third-window pathway were subtracted from the measured values in the *BWx* condition. These pressure differences were used to solve for the compressional sources.

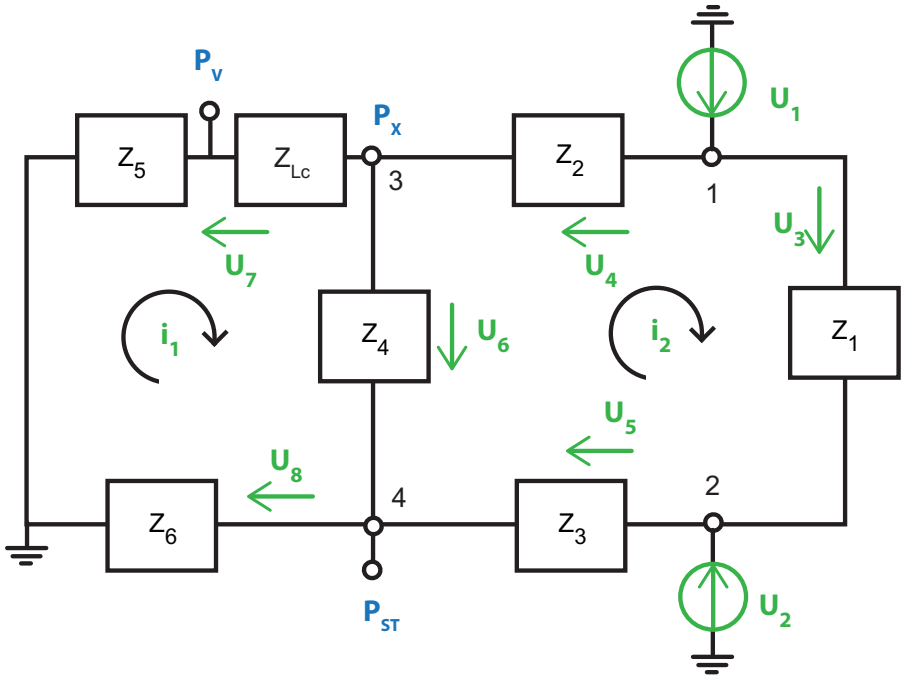

Figure 4.6. Circuit diagram for estimating compressional sources and their effects on intracochlear sound-pressures.
$\mathbf{U_{comp1}}$ and $\mathbf{U_{comp2}}$ of Figure 4.5 are represented here as $\mathbf{U_1}$ and $\mathbf{U_2}$, respectively.

The system of Figure 4.6 was described by a set of linear equations according to Kirchhoff's current and voltage laws, which were combined in matrix form (Equation 4.3); $\mathbf{U_1}$ and $\mathbf{U_2}$ are equal to $\mathbf{U_{comp1}}$ and $\mathbf{U_{comp2}}$, respectively. The system was solved to estimate the compressional source volume velocities. The volume velocities $\mathbf{U_6}$ through $\mathbf{U_8}$ are described in Equations 4.4 - 4.7.

$$\begin{matrix} node\ 1 \\ node\ 2 \\ node\ 3 \\ node\ 4 \\ i_2 \end{matrix} \begin{bmatrix} \boldsymbol{U_1} \\ \boldsymbol{U_2} \\ \boldsymbol{U_3} \\ \boldsymbol{U_4} \\ \boldsymbol{U_5} \end{bmatrix} \times \begin{bmatrix} \mathbf{1} & \mathbf{0} & \mathbf{-1} & \mathbf{-1} & \mathbf{0} \\ \mathbf{0} & \mathbf{1} & \mathbf{1} & \mathbf{0} & \mathbf{-1} \\ \mathbf{0} & \mathbf{0} & \mathbf{0} & \mathbf{1} & \mathbf{0} \\ \mathbf{0} & \mathbf{0} & \mathbf{0} & \mathbf{0} & \mathbf{1} \\ \mathbf{0} & \mathbf{0} & \boldsymbol{-Z_1} & \boldsymbol{-Z_2} & \boldsymbol{-Z_3} \end{bmatrix} = \begin{bmatrix} \mathbf{0} \\ \mathbf{0} \\ \boldsymbol{U_6 + U_7} \\ \boldsymbol{U_8 - U_6} \\ \boldsymbol{P_X - P_{ST}} \end{bmatrix} \quad (4.3)$$

$$\boldsymbol{U_7 = P_V / Z_5} \tag{4.4}$$

$$\boldsymbol{U_8 = P_{ST} / Z_6} \tag{4.5}$$

$$\boldsymbol{P_X = \left(P_V + P_V \frac{Z_{LC}}{Z5} \right)} \tag{4.6}$$

$$\boldsymbol{U_6 = (P_X - P_{ST}) / Z_4} \tag{4.7}$$

Once $\mathbf{U_1}$ and $\mathbf{U_2}$ were defined, they were used to compute the contribution of the compressional sources to the sound-pressure measurements made in the interrupted incudo-stapedial joint (*ISJx*) and normal experimental conditions. In the former case, any middle or external contribution to the sound pressures are removed, while in the latter case all potential sources contribute to the measure sound pressures.

3. Inertial sources

The inertial component of BC is modeled here as a single pressure source. The choice of source placement was a result of analyses involving unique network topologies and numbers of sources. The inertial pressure source is placed to produce a volume velocity across the cochlear partition at the basal end of the cochlea (Figure 4.7). Impedance blocks $\mathbf{Z_5}$ and $\mathbf{Z_6}$ comprise the same circuit elements as they do in Figure 4.6. $\mathbf{Z_{PSc}}$ is the impedance of the cochlear partition ($\mathbf{Z_{Rc}}$) in parallel with the impedance of the cochlear scalae ($\mathbf{Z_1}$, $\mathbf{Z_2}$, and $\mathbf{Z_3}$ of Figure 4.6 placed in series).

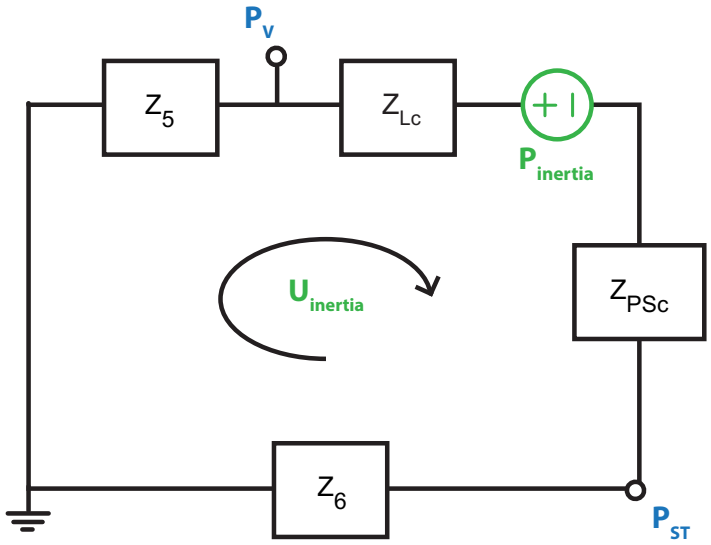

Figure 4.7. Circuit diagram for estimating fluid-inertia source and its effects on intracochlear sound-pressures.

Interruption of the ISJ removes contributions of the inner and middle ear BC sources to measured intracochlear sound pressures. In this case, the stapes is unfixed and the round window is unoccluded, allowing inertial effects to contribute to the measured $\mathbf{P_V}$ and $\mathbf{P_{ST}}$.

Intracochlear sound pressures due to the compressional and third-window sources were estimated in the *ISJx* case from the model and the pre-defined cranial and compressional sources. The combined resulting sound pressures were subtracted from the measured sound pressures of the same condition to estimate $\mathbf{P_V}$ and $\mathbf{P_{ST}}$ produced by the inertial source alone. The pressure difference ($\mathbf{P_V} - \mathbf{P_{ST}}$) and the impedances $\mathbf{Z_5}$ and $\mathbf{Z_6}$ define the current $\mathbf{U_{inertia}}$ (Equation 4.8).

$$\boldsymbol{U_{inertia} = (P_v - P_{ST})/(Z_5 + Z_6)} \tag{4.8}$$

The inertial pressure source was calculated by the total pressure drop across the closed-circuit loop of Figure 4.7 (Equation 4.9).

$$\boldsymbol{P_{inertia} = U_{inertia}(Z_{Lc} + Z_{PSc} + Z_5 + Z_6)} \quad (4.9)$$

With $\mathbf{P_{inertia}}$ defined, intracochlear sound pressures induced by the inertial source were estimated in the normal and *BWx* conditions.

III. Results

A. Impedances

1. Vestibular and cochlear aqueducts

The vestibular and cochlear aqueducts were each modeled as series of conical horns (Equations 3.4 - 3.10). Impedances of the aqueducts, in the direction of inner ear to cranium, are shown for both aqueducts in Figure 4.8. Histological sections of the chinchilla inner ear indicate the aqueducts are partly filled with non-water-like tissue, assumed to have the effect of decreasing the channel cross-sectional area. To model this effect, the diameters of the aqueducts were reduced to half their measured widths. Aqueduct input impedances are shown only in the direction of inner ear to brain, as these impedances model potential pathways for volume velocity produced by the compression and inertial sources. The impedance is mass-like; its magnitude is proportional to the frequency and its phase is a quarter cycle.

Sound pressures transmitted from the brain to the inner ear do not contribute significantly to the measurable intracochlear sound pressures (discussed later in chapter), therefore the aqueduct input impedances in the direction of brain to inner ear are somewhat trivial and are not shown here; the impedances are dominated by the aqueduct itself, not the terminating auditory periphery.

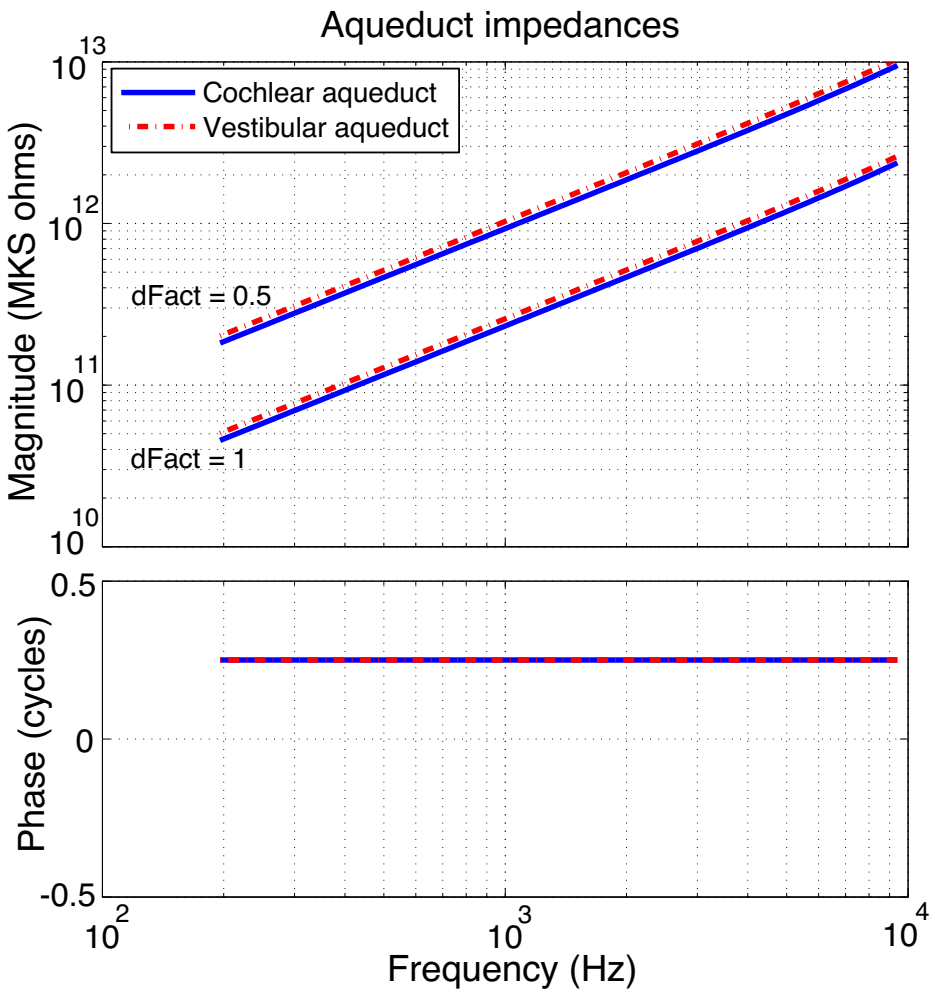

Figure 4.8. Acoustic impedances of vestibular and cochlear aqueducts.
Modeled impedances of the vestibular and cochlear aqueducts in the direction of inner ear to brain according to the measured diameters (dFact = 1) of the aqueducts and to modified versions in which their diameters are halved (dFact = 0.5).

2. Cochlear scalae

The cochlear scalae were modeled as an inductor and resistor in series, representing inertial and viscous effects of the perilymph. The scala vestibuli and scala media were combined based on the assumption that Reissner's membrane has little effect on flow between the two scalae. Impedances of these cochlear spaces are shown in Figure 4.9. The impedance of the cochlear partition is that of R_c of the air-conduction model.

According to Dallos (1970), at low frequencies there is an equilibrium between the impedance of the cochlear partition and its parallel branch associated with flow through the helicotrema. His measurements suggest this occurs at approximately 150 Hz. A helicotrema impedance ($\mathbf{Z_{heli}}$), modeled as an inductor (mass-dominated) was estimated under this assumption (Figure 4.9).

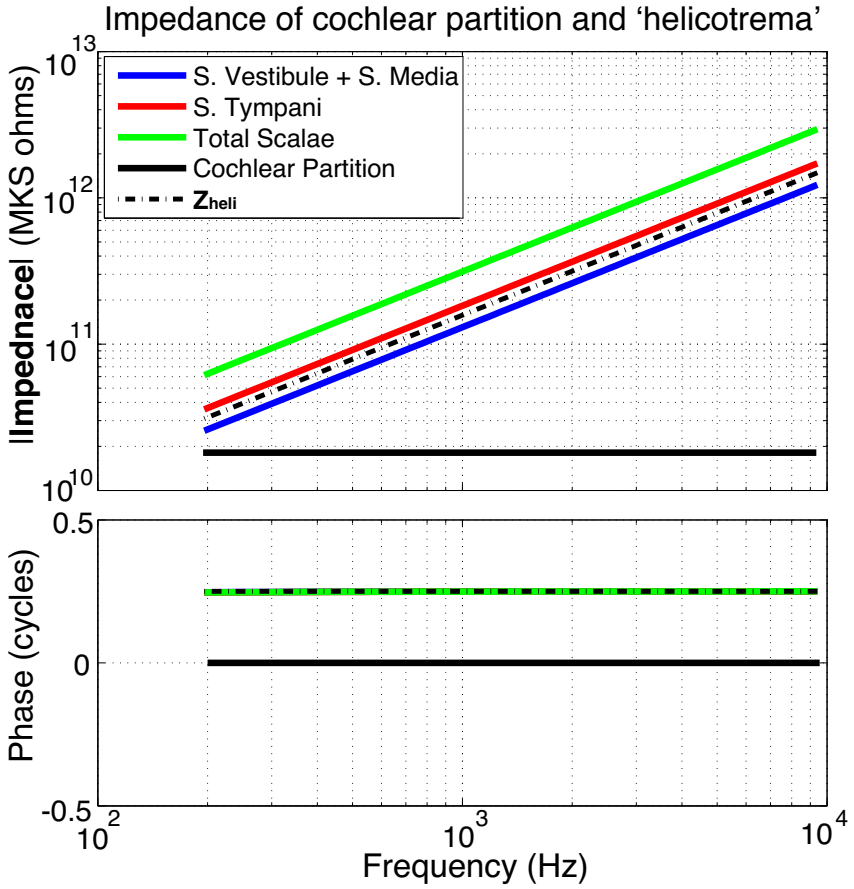

Figure 4.9. Modeled acoustic impedance of cochlear partition, cochlear scalae, and 'helicotrema'.

B. Intracranial sound pressures

BC-induced sound pressures were measured in the brain. The magnitude and phase of the sound pressure, normalized by skull velocity, is shown in Figure 4.10 (n = 3). The sound pressure is considered constant in all conditions of the ear. The pressure source $\mathbf{P_{cranial}}$ of Figure 4.5 was determined by the mean measured intracranial sound pressure.

The mean magnitude of the third-window source increases with a rate of approximately 10 dB/decade between 300 Hz and 2 kHz. Its magnitude increases by approximately 20 dB from 3 and 3.7 kHz. The inertial source magnitude generally decreases proportionally with frequency above 3.7 kHz.

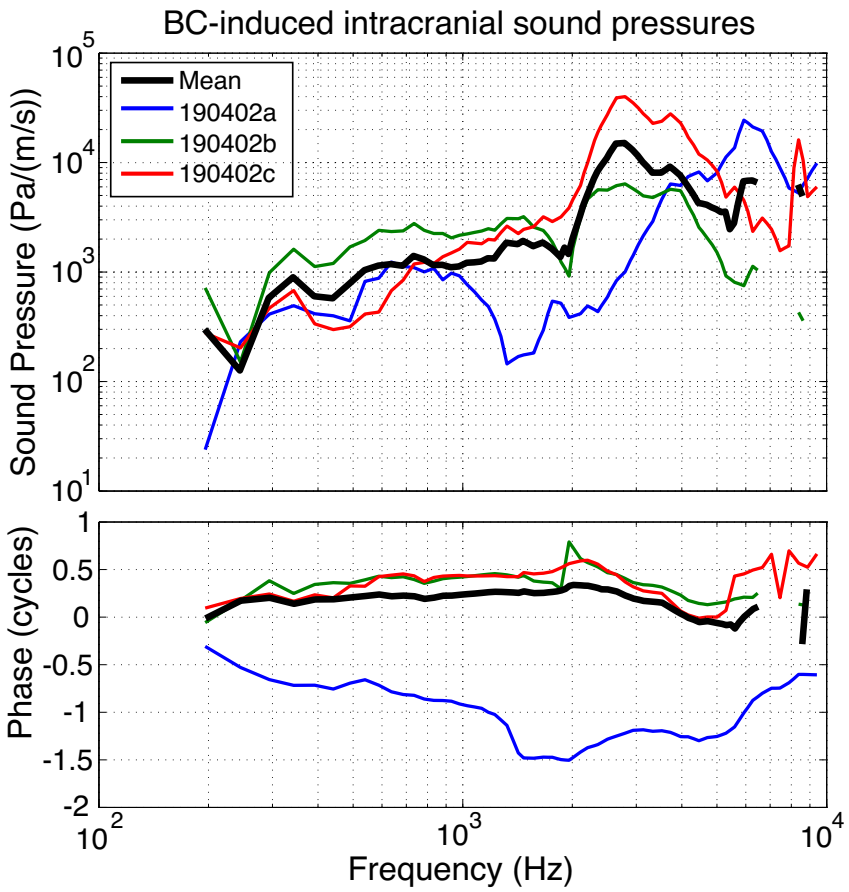

Figure 4.10. BC-induced intracranial sound pressures: third-window pathway.
Sound pressures were measured in the brain of 3 chinchillas during bone-conduction stimulation. The magnitude of these pressures, normalized by skull velocity, model the source associated with the third-window pathways.

C. Compressional source estimates

The magnitude and phase of the compressional BC sources are shown in Figure 4.11. The compressional sources are similar in magnitude with small deviations at frequencies below 800 Hz, and are a half a cycle out of phase.

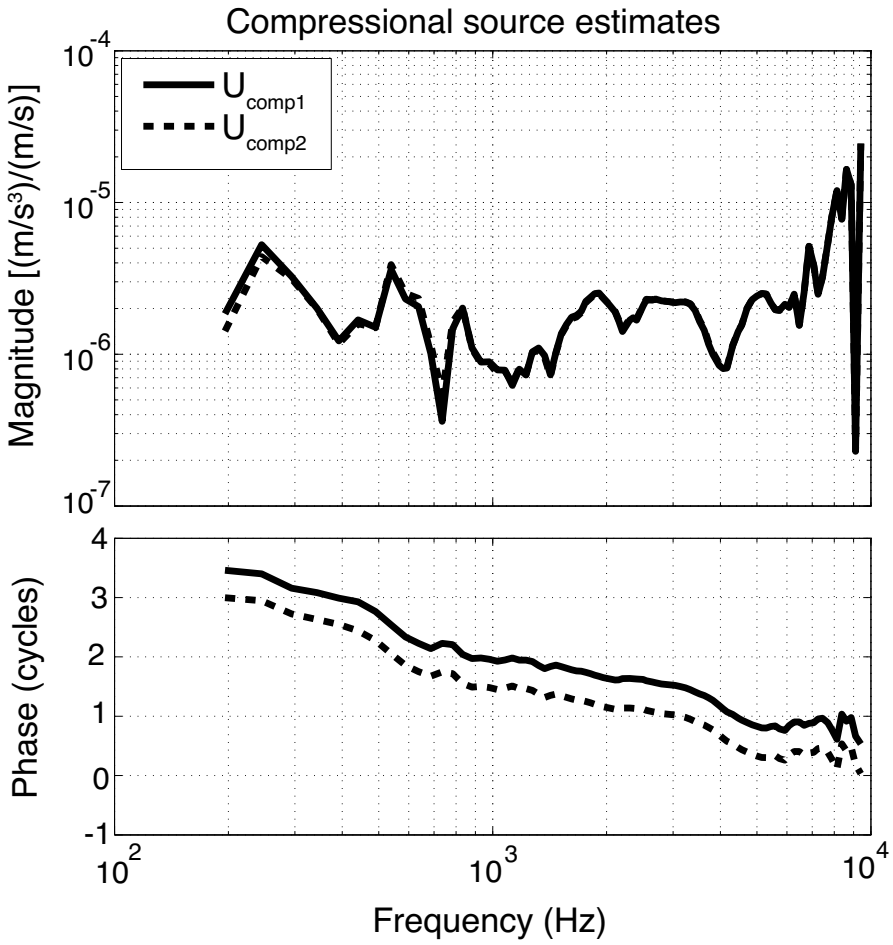

Figure 4.11. Estimates of compressional BC sources of inner ear.

D. Inertial source estimate

The magnitude and phase of the inertial BC source is shown in Figure 4.12. The cranial sound-pressure source (third-window pathway), equal to the mean sound pressure of Figure 4.10, is included in Figure 4.12.

The inertial pressure-source magnitude decreases with increasing frequency at a rate of approximately 30 dB/decade from 200 Hz to 1.2 kHz, the lower-frequency minimum. Another minimum occurs at 3.2 kHz. Magnitude maximums are located at approximately 2 and 6.5 kHz.

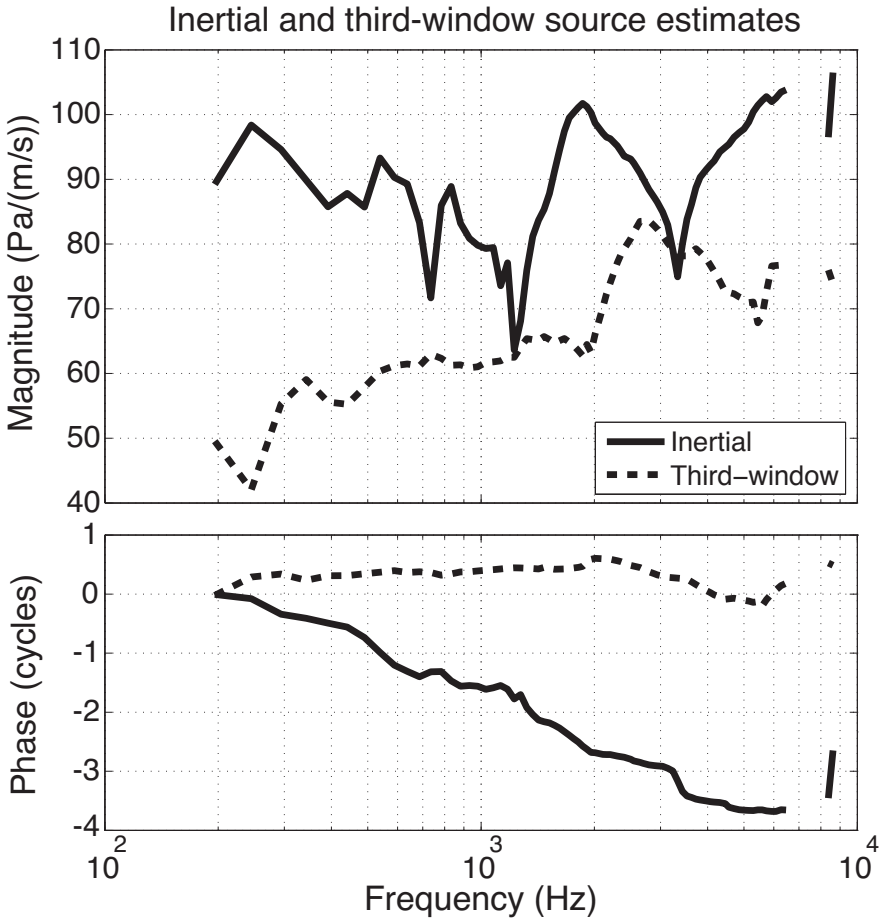

Figure 4.12. Estimates of inertial and third-window-pathway BC sources of inner ear, based on measured intra-cranial sound pressures and modeled impedances.

E. Intracochlear sound pressures; measurements and model predictions

Intracochlear sound pressures were measured during BC stimulation and are shown in Figure 4.13 - 4.15. Included in these figures are the estimated sound pressures induced by the inner ear BC components. The conditions of the auditory periphery are shown in the order in which they were considered for characterizing the volume velocity sources: first, *BWx* is the condition in

which the inertial effects are assumed inactive (Figure 4.13); second, the *ISJx* condition permits inertial effects while simultaneously removing effects of the external ear BC source and minimizing ossicular inertia—only the stapes remains (Figure 4.14). Complete analyses of the *BWx* and *ISJx* conditions were then performed with the inner-ear sources fully characterized. BC-induced intracochlear sound pressures were then estimated in the normal (Figure 4.15), and the *Stx* and *RWx* (supplemental Figure B.1 and B.2) conditions. Analysis of the *BWx* condition performed with the full circuit including the inertial pressure source is shown in Figure 4.16.

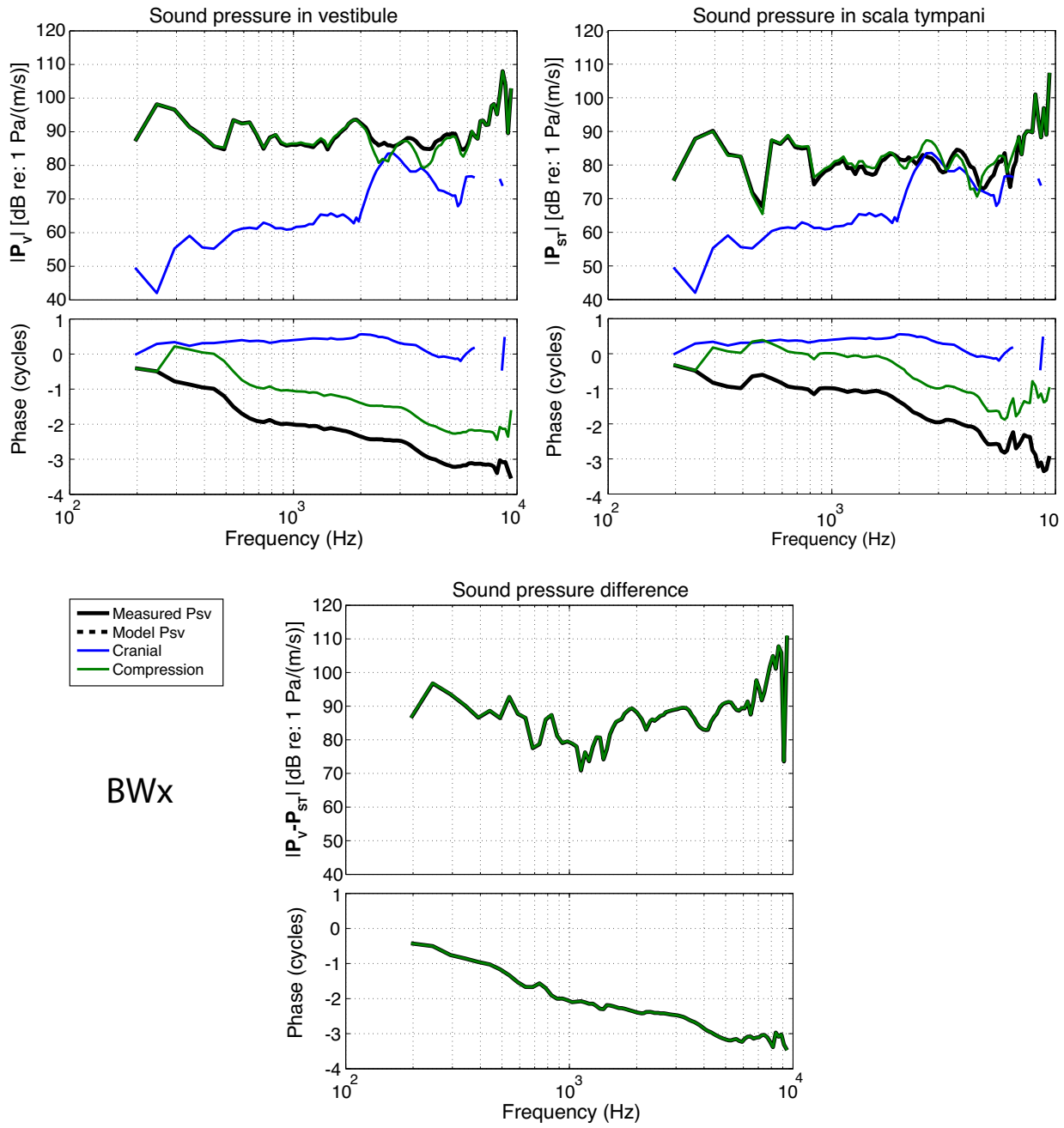

Figure 4.13. Intracochlear sound pressures in *BWx* condition (without inertial source). Intracochlear sound pressures were measured with the stapes fixed and round window occluded, in the vestibule and scala tympani (n = 10); estimated sound pressures due to each of the inner-ear BC components, and their combined resulting pressures, are shown.

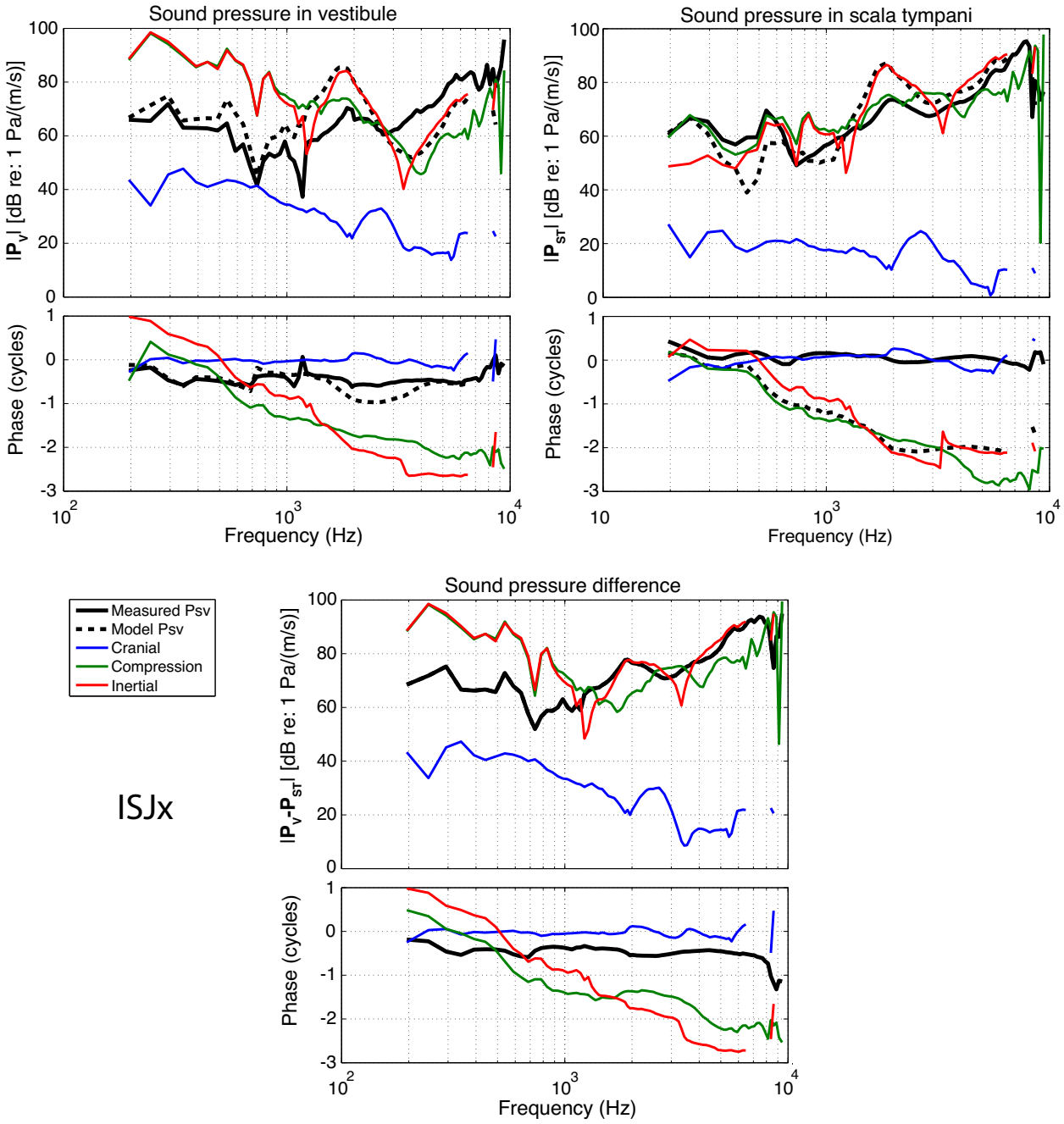

Figure 4.14. Intracochlear sound pressures in *ISJx* condition.
Intracochlear sound pressures were measured while the ISJ was interrupted (no cochlear-window occlusion), in the vestibule and scala tympani (n = 10); estimated sound pressures due to each of the inner-ear BC components, and their combined resulting pressures, are shown.

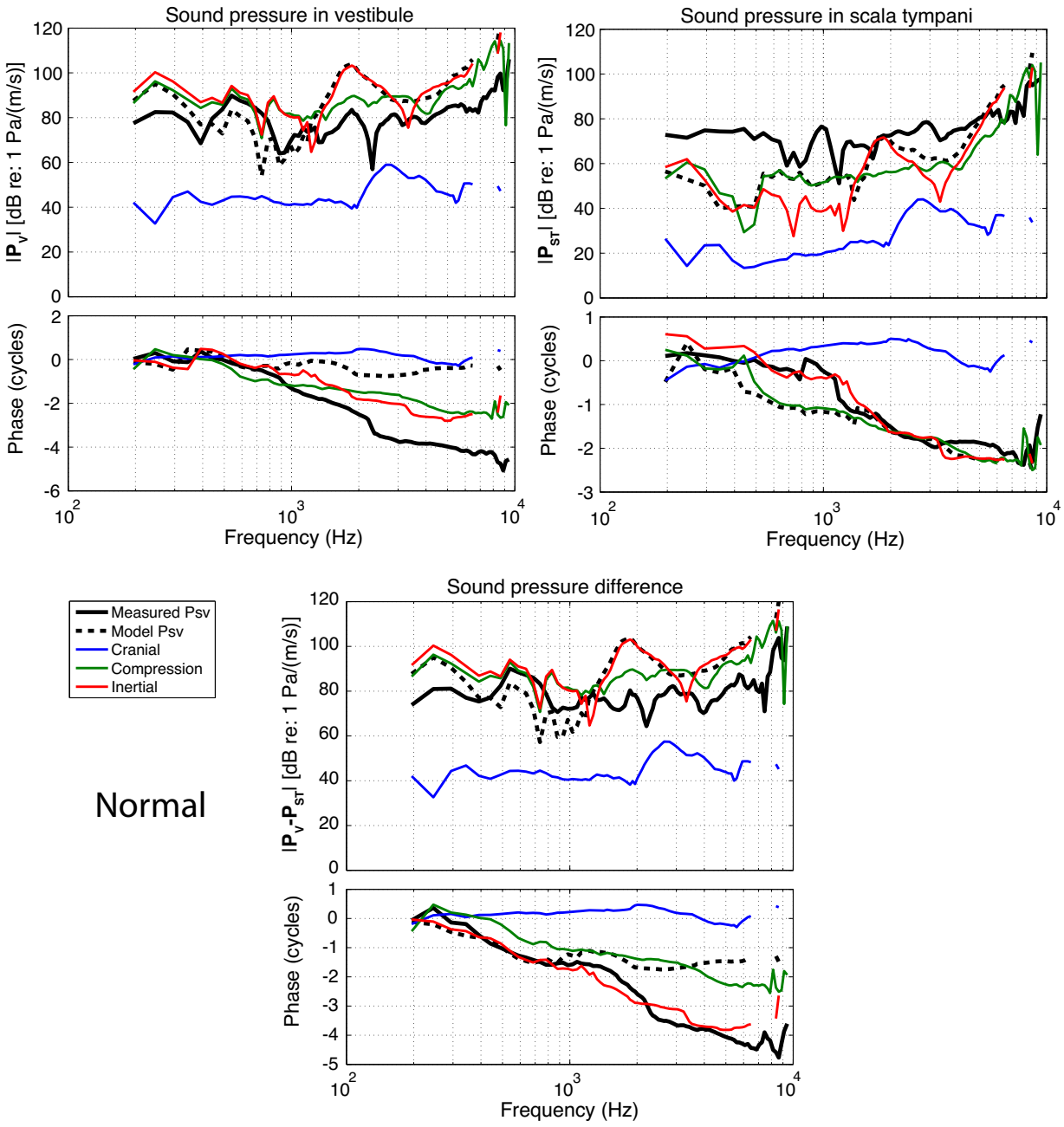

Figure 4.15. Intracochlear sound pressures in normal-ear condition.
Intracochlear sound pressures were measured in the vestibule and scala tympani in the normal ear (n = 24); estimated sound pressures due to each of the inner-ear BC components, and their combined resulting pressures, are shown.

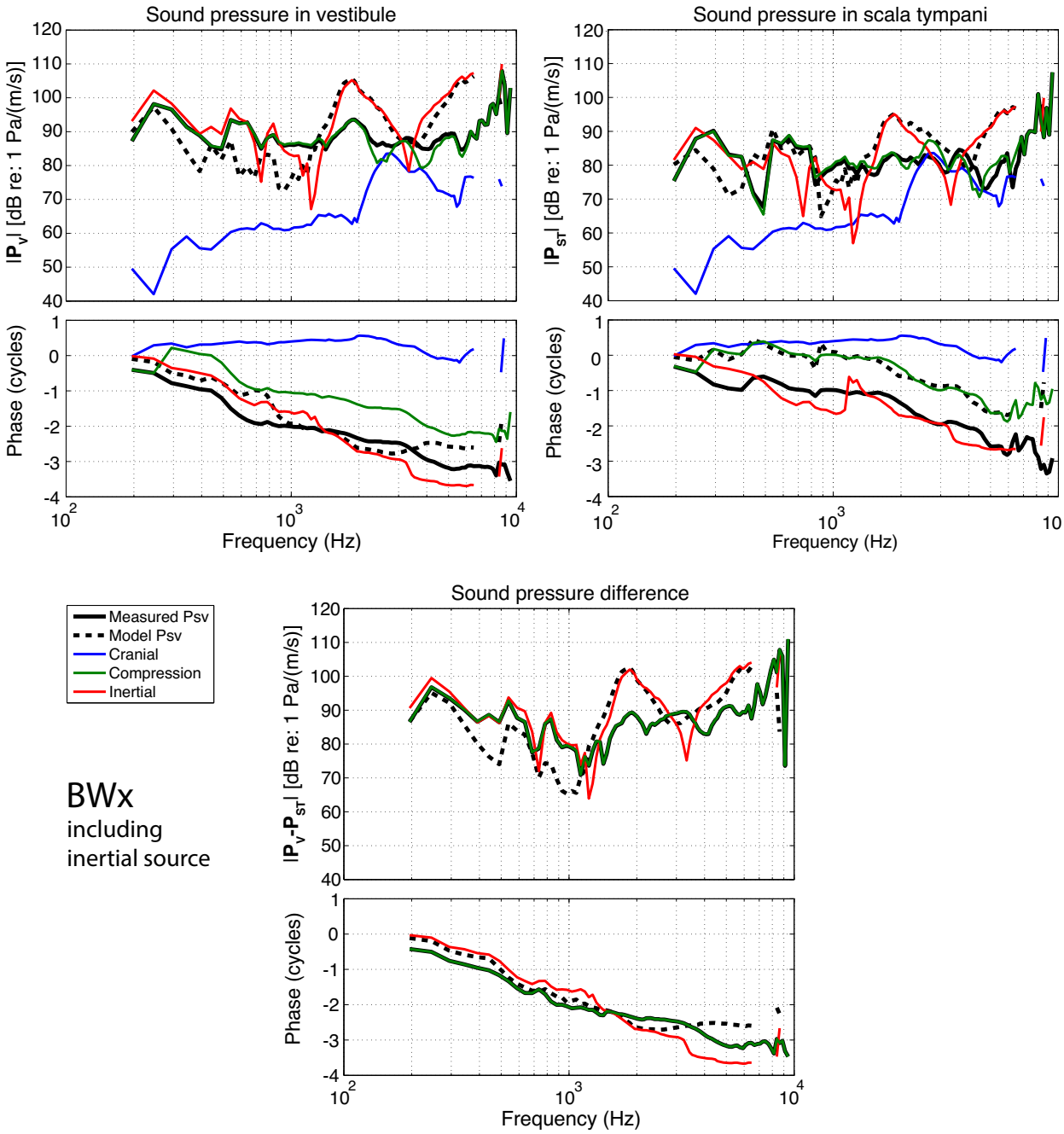

Figure 4.16. Intracochlear sound pressures in *BWx* condition (with inertial source). Intracochlear sound pressures were measured in the vestibule and scala tympani in the normal ear (n = 24); estimated sound pressures due to each of the inner-ear BC components, and their combined resulting pressures, are shown.

The intracochlear sound pressures $\mathbf{P_V}$ and $\mathbf{P_{ST}}$ resulting from the third-window component of BC were estimated in the *BWx* condition (Figure 4.11A and B). The estimated sound pressures are approximately 30 dB less than the measured values below 2 kHz. Between 2 and 4 kHz, the third-window component generates a $\mathbf{P_V}$ within 10 dB of the measured sound pressure, with a minimum difference of 2 dB occurring at 2.6 kHz. $\mathbf{P_{ST}}$ produced by this component is similar in magnitude to the measured sound pressure between 2.6 and 6.5 kHz.

Consistent with our definition of the compressional sources from the data, the magnitude and phase of the estimated sound pressures produced by compressional sources are generally equal to that of the measured sound pressures in the *BWx*, except at those frequencies where the third-window-pathway source appears to contribute to the measured sound pressures. Note that $\mathbf{P_V}$ and $\mathbf{P_{ST}}$ predicted from the cranial source alone are equal (consistent with a circuit where the blocked windows allow no current flow), and this equality produces a 0 pressure difference across the cochlear partition; therefore, the estimated total pressure difference is due to the compressional sources alone.

The inertial source was estimated in the *ISJx* condition, in which all three inner ear BC components are active. The sound pressures predicted by the defined compressional and third-window sources were summed and then subtracted from the measured sound pressures, of this condition, to determine the contribution of the inertial component. We see in Figures 4.14A and B that the estimated total sound pressures from all sources (dashed black lines) does not equal that of the measured sound pressure (solid black line). In Figure 4.14A, the $\mathbf{P_V}$ predicted from the compressional source is an order of magnitude greater than the measured sound pressures at frequencies below 1 kHz, which is balanced by a $\mathbf{P_V}$ predicted for the inertial source of the same magnitude and opposite phase of the compressional sources. In Figure 4.14B, the $\mathbf{P_{ST}}$ resulting

from the inertial and compressional sources are similar in magnitude and generally out of phase between 400 Hz and 1.5 kHz. The compressional sources dominate the total pressure below 400 Hz and around 2 kHz, while the inertial source dominates within the frequency ranges of 1.5 to 2.5 kHz and 3.5 to 6.5 kHz. The difference between the inertia-source and compressional-source induced pressure differences (Figure 4.14C) are similar to those of $\mathbf{P_V}$. While we see differences in $\mathbf{P_V}$ and $\mathbf{P_{ST}}$ between the measurements and model predictions, the estimated total pressure difference is equal to that of the measured difference, which is consistent with our use of the pressure difference data in this condition to compute the inertial source.

Measured and estimated sound pressures of the normal ear are shown in Figure 4.15. The third-window pathways contribute little to the total $\mathbf{P_v}$, except at 2.2 kHz, and do not contribute to the measured $\mathbf{P_{ST}}$ at any frequency. The estimated $\mathbf{P_V}$ of the inertial and compressional source are similar in magnitude and opposite in phase below 1.3 kHz. The inertial source dominates within the frequency ranges of 1.5 to 2.5 kHz. Above 2.5 kHz, the estimated total $|\mathbf{P_V}|$ is up to 20 dB greater than the measured values. The compressional source dominates the total estimated $|\mathbf{P_{ST}}|$ between 500 Hz and 1.5 kHz, while the inertial source dominates the total estimated $|\mathbf{P_{ST}}|$ between 1.5 and 2.5 kHz. The estimated total $|\mathbf{P_V}\text{-}\mathbf{P_{ST}}|$ is up to 20 dB greater than the measured differential above 1.5 kHz.

As a test of our assumption that the inertial source does not contribute to the measured pressures in the *BWx* condition, we used the inertial sources characterized in the interrupted-ISJ condition, to predict its effect on sound pressures in the *BWx* condition (Figure 4.16). The predictions in this set of figures are not consistent with our assumption. Above 1.3 kHz, $|\mathbf{P_V}|$ due to the inertial component is greater in magnitude than $|\mathbf{P_V}|$ generated by the compressional sources, except at approximately 3.1 kHz. A similar effect of the inertial component on $|\mathbf{P_{ST}}|$ can

be seen at the same frequencies. The magnitude of the total estimated $|\mathbf{P_V}\text{-}\mathbf{P_{ST}}|$ is generally less than the measured values below 1.3 kHz and generally greater above this frequency.

Measured and estimated sound pressures in the *Stx* and *RWx* conditions are shown in supplemental Figures C.1 and C.2.

IV. Discussion

A. Impedances of the vestibular and cochlear aqueducts, and cochlear scalae

The vestibular and cochlear aqueducts were modeled as a series of conical horns. In the direction of inner ear to brain (forward), an impedance approximating brain tissue terminated both aqueducts. In the reverse direction, the complete ear model of the appropriate condition terminated the aqueducts. Impedances in the forward direction, dominated by inertial effects, are shown in Figure 4.8. The aqueducts are filled with both lymph and non-water-like tissue, with the latter decreasing the effective diameter of the aqueducts. The diameter was halved in the final cochlear model. As can be seen in Figure 4.8, halving the diameter shifts the magnitude equally across all frequencies by a factor of approximately 4, as would occur if the impedance were modeled by a simple inductor (Equation 4.1). The inductive-like behavior (associated with an acoustic mass) of similar magnitude dominates the impedance of the aqueducts looking from the cranium into the inner ear.

The vestibular and cochlear aqueducts are similar in geometry and are terminated cranially by the same impedance. As such their impedances in the forward direction are similar. When the oval and round windows are occluded, the presence of these aqueducts permits volume velocity within the circuit. In this condition, small changes in the relative impedance of the aqueducts

may cause significant changes in the pressure across the cochlear partition. Visual inspection of histological sections of a single chinchilla inner ear suggests the vestibular aqueduct may be of smaller cross-sectional, compared to the cochlear aqueduct, a difference that could be obscured by the resolution of the microCT images.

Impedances of the cochlear scalae are shown in Figure 4.9. The impedance of the scala vestibuli plus scala media, and the scala tympani are also inductance-dominated across all frequencies investigated. The impedance of the cochlear partition ($\mathbf{Z_{Rc}}$) is lower in magnitude than the scalae impedance estimates. In the case of air-conduction, the cochlear input-impedance is dominated by the impedance $\mathbf{Z_{Rc}}$; however, in bone-conduction the impedance of the scalae may play a role in how cochlear compression and fluid inertia contribute to the cochlear drive. In our model, the placement of the inertial source is such that its contribution to $\mathbf{P_V}$ and $\mathbf{P_{ST}}$ is not affected by the impedances of the scalae above 200 Hz.

Dallos (1970) suggested the impedances of the helicotrema and the cochlear partition form a parallel circuit, where at low frequencies the impedance of the helicotrema is smaller in magnitude, and at higher frequencies the parallel impedance is dominated by the less-impedant cochlear partition. A hypothetical impedance $\mathbf{Z_{heli}}$ modeling the helicotrema (not included in our model) was estimated by an inductor having an impedance magnitude equal to that of the cochlear partition at 150 Hz (Figure 4.9). $\mathbf{Z_{heli}}$ has a magnitude approximately 6 dB less than the total scalae impedance. This similarity suggests that the impedance parallel to that of the cochlear partition may be due to the fluid mass of the scalae and not of the helicotrema itself (Puria and Allen, 1991). The difference here between the magnitudes of the helicotrema and total scalae impedance may be due to simplification of the scalae geometry; an average cross-sectional area was used to estimate the scalae impedances.

B. The predicted effect of intracranial sources on the measured sound pressures

The cranial sound pressure source, $\mathbf{P_{cranial}}$, was estimated form measurements and $\mathbf{P_V}$ and $\mathbf{P_{ST}}$ produced by $\mathbf{P_{cranial}}$ were predicted for various conditions of the ear (Figures 4.11 - 4.16; supplemental Figures B.1 and B.2).

In the *BWx* condition (Figure 4.11), the $\mathbf{P_V}$ and $\mathbf{P_{ST}}$ produced by $\mathbf{P_{cranial}}$ are at least an order of magnitude less that the measured sound pressures below 2 kHz. The third-window component is predicted to contribute significantly to the total $|\mathbf{P_V}|$ and $|\mathbf{P_{ST}}|$ between 2 and 6 kHz. Note that the model circuit of Figure 4.5 in the *BWx* condition prohibits the third-window source from producing a volume velocity. With only the third-window source active, the system is constrained by an equal sound pressure at every node and a non-existent pressure difference ($|\mathbf{P_V}$-$\mathbf{P_{ST}}|$).

In the *ISJx* condition, $\mathbf{P_{cranial}}$ produced an estimated $\mathbf{P_V}$ and $\mathbf{P_{ST}}$ (Figure 4.14A and B) of at least an order of magnitude less than the measured value across all frequencies, with the exception of $\mathbf{P_V}$ at 700 Hz and 1.2 kHz, where the their magnitudes are similar (Figure 4.14A and B). $\mathbf{P_{cranial}}$ does not contribute the pressure differential across the cochlear partition (Figure 4.14C).

Figures 4.15A and B suggest in the normal ear, $\mathbf{P_{cranial}}$ does not contribute to the measured $\mathbf{P_V}$ and $\mathbf{P_{ST}}$, with the exception of $\mathbf{P_V}$ at 2.2 kHz, where the their magnitudes are similar. $\mathbf{P_{cranial}}$ does not contribute the measured pressure differential across the cochlear partition (Figure 4.15C).

C. Estimated vs. measured sound pressures

To estimate the compressional sources, we assumed that in the *BWx* condition the measured intracochlear sound pressures are produced by cochlear compression and third-window sound pressure transmission without any inertial components. If the inner ear structures and its BC sources are accurately modeled, and the assumption of compressional source dominance in the *BWx* condition holds true, the magnitude of the sound pressures resulting from the inertial sources should be less than the measured sound pressures. In Figure 4.16, the estimated sound pressures resulting from each component in the *BWx* condition are shown. With the inertial source active, the estimated total $|\mathbf{P_V}|$ and $|\mathbf{P_{ST}}|$ does not follow the magnitude of the pressures produced by the compressional sources as it does when the inertial source is inactive. The estimated total $|\mathbf{P_V}|$ is less than the measured pressures below 1.3 kHz, and is general greater than the measured pressures above this frequency, where the inertial source dominates (Figure 4.16A). The estimated total $|\mathbf{P_{ST}}|$ is also dominated by the inertial source at most frequencies above 1.3 kHz (Figure 4.16B). Moreover, the estimated pressure differential $|\mathbf{P_V}\text{-}\mathbf{P_{ST}}|$, exhibits a behavior similar to $|\mathbf{P_V}|$. The large estimates of $|\mathbf{P_V}|$ and $|\mathbf{P_{ST}}|$ produced by the inertial component suggest the choice of network topology, source types and placements, and/or the assumption that the inertial component is inactive in the *BWx* condition are/is incorrect (Figure 4.16C). Because of the broken hypothesis, our estimates of the compressional source must be inaccurate, and this will lead to inaccuracies in our estimate of the inertial sources.

Measured and estimated intracochlear sound pressures in *ISJx* condition are shown in Figure 4.14. Estimates of $\mathbf{P_V}$ magnitude are similar for the compressional and inertia sources up to 1 kHz, and the associated phases are a half cycle apart, with a resulting total magnitude that is approximately 30 dB less sound pressures generated by the sources separately (Figure 4.14A).

The inertial component dominates the $|\mathbf{P_V}|$ above 3 kHz. The estimated $|\mathbf{P_V}|$ due to these two sources are not equal but are of similar magnitude. The magnitude of the estimated total $\mathbf{P_V}$ follows that of the inertial source between 1.3 and 2.3 kHz and above 4 kHz, as does the pressure differential $|\mathbf{P_V}\text{-}\mathbf{P_{ST}}|$ (Figure 4.14C). $|\mathbf{P_{ST}}|$ produced by the compressional and inertial sources are similar between 400 Hz and 1.2 kHz; the half-cycle phase difference of these pressures results in a decreased estimated total $|\mathbf{P_{ST}}|$ (Figure 4.14B).

Estimated and measured sound pressures are shown for the normal condition in Figure 4.15. Pressure measurements of this condition were not used in characterizing the inner ear BC sources. The magnitudes of $\mathbf{P_V}$ due to the compressional and inertial sources are similar below 1.3 kHz (Figure 4.15A), as was the case in the *ISJx* condition (Figure 4.14A). The total estimated $|\mathbf{P_V}|$ is approximately 10 dB greater than the measured sound pressure below 400 Hz, is 10 to dB less between 400 and 800 Hz, and is approximately 10 to 35 dB greater than the measured sound pressure above 1.3 kHz. The estimated total $|\mathbf{P_{ST}}|$ is generally less than the measured sound pressure with the greatest deviation (35 dB) at between 300 and 500 Hz (Figure 4.15A). The magnitude of the estimated total pressure differential (Figure 4.15C) is dominated by $|\mathbf{P_V}|$.

Measured and estimated sound pressures in the *Stx* and *RWx* conditions are shown in Appendix C.

D. Estimation of the inertial source

According to Equation 4.8, the volume velocity of the closed loop circuit is constrained by the impedances $\mathbf{Z_5}$ and $\mathbf{Z_6}$ and the pressure difference across them, $\mathbf{P_V}\text{-}\mathbf{P_{ST}}$. The ground ($\mathbf{P_{ground}} = 0$) at the node between $\mathbf{Z_5}$ and $\mathbf{Z_6}$ places an additional constraint on the system (Figure 4.7), making it over-determined. Estimation of the inertial pressure source, as described by Equation 4.8, is independent of the pressure at this node, and estimation of $\mathbf{P_{ground}}$ based on this same

equation will produce a non-zero value. (Alternatively, the volume velocity of the circuit could be defined by the pressure difference $\mathbf{P_V}$-$\mathbf{P_{ground}}$ or $\mathbf{P_{ST}}$-$\mathbf{P_{ground}}$ across either $\mathbf{Z_5}$ or $\mathbf{Z_6}$, respectively. However, the system remains over-determined.)

With the inertial pressure source defined, $\mathbf{P_V}$ and $\mathbf{P_{ST}}$ are calculated, adhering to the ground constraint. As a result, in the *ISJx* condition, the estimated pressures will not equal those that were used to define the source. This is evident in Figures 4.14A and B, where the total estimated sound pressures do not match the measured data. However, the estimated total pressure difference $\mathbf{P_V}$-$\mathbf{P_{ST}}$ does equal the measured difference, as an absolute value of $\mathbf{P_{ground}}$ is not required in calculating this pressure difference.

Estimates of the inertial pressure source based on various the constraints are shown in supplemental Figure C.3 for reference. None of these estimates are necessarily correct. Furthermore, a measure of error associated with the different constraints cannot be made, as there is no ground-truth for which to compare. The source of error may reside in multiple measurements and impedance estimates, as well as the network topology.

E. Comparison to other models

Schick (1991) developed an electric model of the human cochlea and middle ear to investigate the inner-ear bone-conduction mechanisms. He looked at basilar membrane displacement as a function of position along the cochlea and frequency of stimulation. Relative displacement amplitudes were estimated as the measured potential across the basilar membrane, modeled as parallel capacitors coupled by inductors to account for fluid mass effects in the longitudinal direction. In his model, motion of the cochlear wall is localized, directly stimulating the basilar membrane at a similar position along the length of the cochlea. In our study, the

magnitude of cochlear drive is proportional to the pressure difference at the base of the cochlear partition, as it is our assumption that this pressure gradient generates the traveling wave and that pressure differences along the membrane are a function of its mechanical properties and active mechanisms of the hearing organ. A limitation of Schick's model (1991) is that relative contributions of the different components of bone conduction cannot be determined. His results suggest that the compressional component excites the basilar membrane with maximum amplitude at frequencies above 1 kHz, while the inertial component is most effective between 200 Hz and 2 kHz.

Stenfelt (2015) developed a lumped-element circuit model of the inner ear to investigate the relative importance of the compressional and inertial components of BC hearing in human. The magnitudes of these sources were dependent on the relative motion of the cochlear walls, estimated by phase differences in a longitudinal sound pressure wave—simulating the BC stimulus—transmitted across through the cochlea. This simplification ignores higher modes of distortion, does not account for variations in wave propagation, and does not consider compressibility of the cochlea due to pressure gradients across the cochlear boundary. Similar to our study, Stenfelt quantifies the contribution of the sources to BC hearing by the response of the basilar membrane at the base of the cochlea. The results of his study suggest that the inertial component is the dominating inner ear source of BC across all frequencies considered in the present study. As previously stated, our model does not assume specific mechanics of the sources. A direct comparison of the relative contributions cannot be made between the two studies, as the results of our model are likely inaccurate to some degree.

The finite element models of Bohnke and Arnold (2006) and Kim et al. (2011), and the circuit models of Schick (1991) and Stenfelt (Stenfelt, 2015) assume simple mechanics of the BC

sources. Because of the demonstrated inaccuracy of our estimates of compression and inertial sources a direct comparison of the relative contributions cannot be made between the two studies, as the results of our model are likely inaccurate to some degree.

Finally, while the model presented here is of the chinchilla ear, our proposed method of characterizing the inner ear components of BC hearing could be extended to research in humans.

F. Model limitations and weaknesses

1. Quality of window occlusion and pressure-sensor seal

Our model assumes the application of dental cement at the oval and round windows results in occlusions that may be modeled as an infinite impedance. This is likely a good approximation for oval window occlusion, when the stapes is fixed to the cochlear bone. It is possible, however, in the case of round window occlusion for air bubbles to be trapped between the cement and the round window membrane, causing a reduction in the impedance at high frequencies. To test the effect of a less-than-ideal occlusion, the modeled round window compliance was decreased over a range of magnitudes. As the compliance is decreased, the estimates of $\mathbf{P_V}$ and $\mathbf{P_{ST}}$ continue to change noticeably, until the compliance is reduced by a factor of 1e7. Therefore, an occlusion altering the compliance by a factor of less than this may produce a response not representative of the occluded condition. Similar issues may exist with compliance of Jeltrate® surrounding the sound pressure sensors.

2. Unknown complex system behavior

An understanding of the potentially complex mechanics associated with each of the inner ear BC sources is not necessary for its characterization, based on the method proposed here. However, this becomes a disadvantage; even if the sources are characterized quantitatively such

that the estimated responses match the measured data of each condition, full descriptions of the source mechanics are not likely attainable.

3. Non-linear cochlear mechanics

The current study does not consider active cochlear mechanics. It is not clear that these mechanics, in regard to BC hearing, are unaffected by changes in impedances, namely of the oval and round windows. If, for example, a source estimate includes measurable effects of active cochlear mechanics, these effects may change in a different condition of the ear, making the prior source estimate inaccurate under the different condition.

V. Conclusion

The inner-ear source of bone-conduction hearing is believed to comprise several mechanisms. At the present time, no one has yet clearly determined the dominating mechanism(s) of this source. Various methods have been used to investigate these mechanisms, including lumped-element circuit models and finite element models. These models are developed and solved under different assumptions and these assumptions are important for correctly modeling the behavior of the sources.

A method is proposed here that minimally assumes the mechanics of each inner ear BC source. The type of electric element used to model the different sources and their placement within the model are affected by our assumptions; however, our method involves measured data, namely BC-induced intracochlear sound pressure measurements, to characterize the sources. These measurements were made under varying conditions of the ear, and these conditions may be used to isolate the activity of these components.

Our results suggest sound-pressure transmission via third-window pathways does not play a significant role in bone-conduction hearing in chinchilla; the estimated sound-pressure differential across the cochlear partition due to this source, as modeled here, is an order of magnitude below the measured differential at most frequencies, in all conditions. The magnitude of this source is directly related to the BC-induced intracranial sound pressures. Manipulation of the auditory periphery is not required to isolate this source, therefore any inaccuracies in its estimation is limited to impedance estimates and assumptions of cochlear network topology.

Our estimates of the inertial and compressional sources are likely inaccurate, as estimated intracochlear sound pressures due to these sources can be larger than the measured sound pressures (Figure 4.14-4.16). Sources of error may include cochlear model network topology, based on assumptions of the nature of inner ear BC sources, impedance estimates, and degree of source isolation by manipulation of the auditory periphery. The theoretical framework described here for isolating these inner-ear bone-conduction sources requires further investigation.

CHAPTER 5. Conclusion

I. Air-conduction model

A lumped-element circuit model was developed for air-conduction hearing in chinchilla. This model, based on the classic Zwislocki model of air-conduction hearing in human, serves as the basis for a bone-conduction hearing model.

The unknown parameter values were determined by fitting various model outputs to mechanical and acoustic responses of the chinchilla middle ear and cochlea. The model was constrained where possible by directly relating parameter values to geometries of the middle ear (e.g., transformer ratios of the middle ear were determined by areas of the tympanic membrane and stapes footplate, and lengths of the malleus and incus). Other parameters were determined by an iterative process involving automated and manual optimization methods.

II. Bone-conduction model

Our chinchilla bone-conduction model was adapted from our model of air-conduction hearing. In the air-conduction model, most analyses can be performed with the introduction of an arbitrary volume velocity or pressure source. The bone-conduction model input is constrained by relative magnitudes of its sources, with each source magnitude and phase relative to a global system input, a skull velocity driven by a bone-conduction stimulator. The sources must be characterized accurately to understand how they work together.

III. External-ear source

The external-ear source of bone conduction is thought to be due to compression of the ear canal walls that perturbs the volume of air within the canal, generating a sound pressure. This BC-induced ear-canal sound-pressure was measured under various conditions of the middle ear

and ear canal. The EEBC was characterized by using the measured sound pressures and modeled impedances of the auditory periphery.

Isolation of the EEBC in its effect on the measured ear-canal sound pressures, by manipulations of the middle ear, allowed us to study its contribution to the ECSP in the normal ear. Our results suggest that in the normal condition, the BC-induced ECSP is dominated by the external-ear source.

Relative motion of the lower jaw with respect to the ear canal does not contribute to the measurable sound pressure within the canal, according to our data.

Compound action potentials—the summation of action potentials of the auditory nerve in response to sound—were measured in the live chinchilla. Comparison of these neural responses at threshold across different conditions of the ear were used to investigate the contribution of the external-ear bone-conduction source to BC hearing, while the ear canal is open and occluded. Our results suggest that the EEBC contributes to BC hearing in both conditions of the ear canal.

IV. Inner-ear source

The inner-ear source of bone-conduction hearing is believed to comprise several mechanisms. To our knowledge, no one has yet clearly determined the dominating mechanism(s) of this source. It is likely that the answer is frequency dependent. Various methods have been used to investigate these mechanisms, including lumped-element circuit models and finite element models. These models are developed and solved under different assumptions and these assumptions are important for correctly modeling the behavior of the sources.

A method is proposed here that minimally assumes the mechanics of each component. The type of electrical element used to model the different components and their placement within the

model are affected by our assumptions. Ourr method involves using measured data, namely BC-induced intracochlear sound pressure measurements, to characterize the sources. These measurements were made under various conditions of the ear, which may isolate the activity of these components.

The validity of our inner-ear BC source estimates is dependent upon the accuracy of our modeling of various conditions of the middle ear and assumptions of the nature of the sources. Moreover, the validity of our estimates of the inertial and compressional inner-ear BC sources is dependent upon the degree of source isolation achieved. As previously noted, the theoretical framework described here for isolating these inner-ear BC sources requires further investigation.

Appendix A

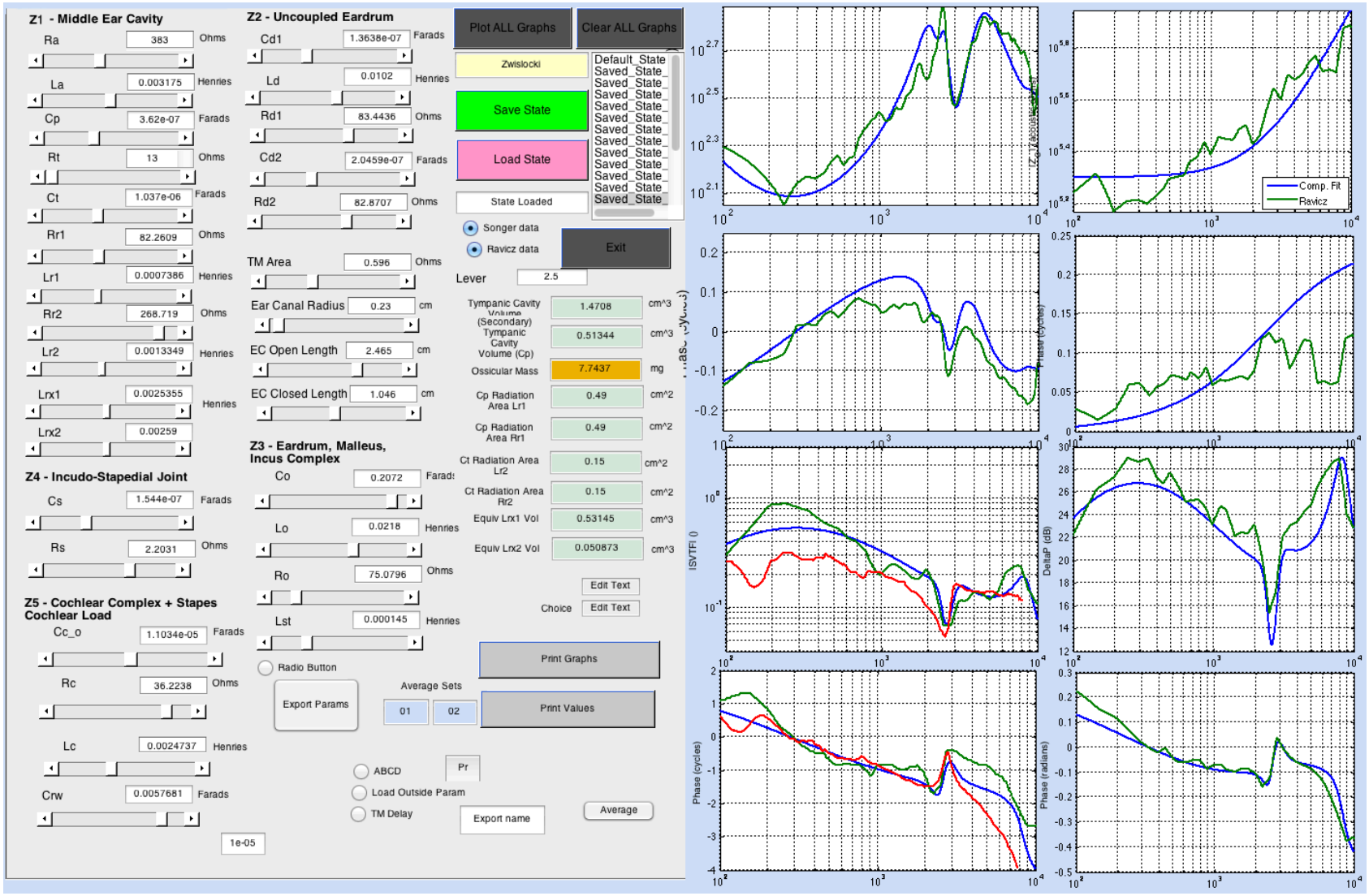

Figure A.1. Graphical user interface for manual optimization of an air-conduction hearing model for chinchilla.

Appendix B

A. Chinchilla auditory periphery

Figure B.1 shows a volume reconstruction (generated with Amira software) of the posterior (caudal) half of a complete chinchilla ear (external, middle, and inner ear) – sectioned along the ear-canal axis – from a series of microCT scans performed at the Center for Skeletal Research at Massachusetts General Hospital. The complete 3D reconstruction was used to quantify the geometry of the external ear, which was the basis of our ear-canal acoustic impedance estimates.

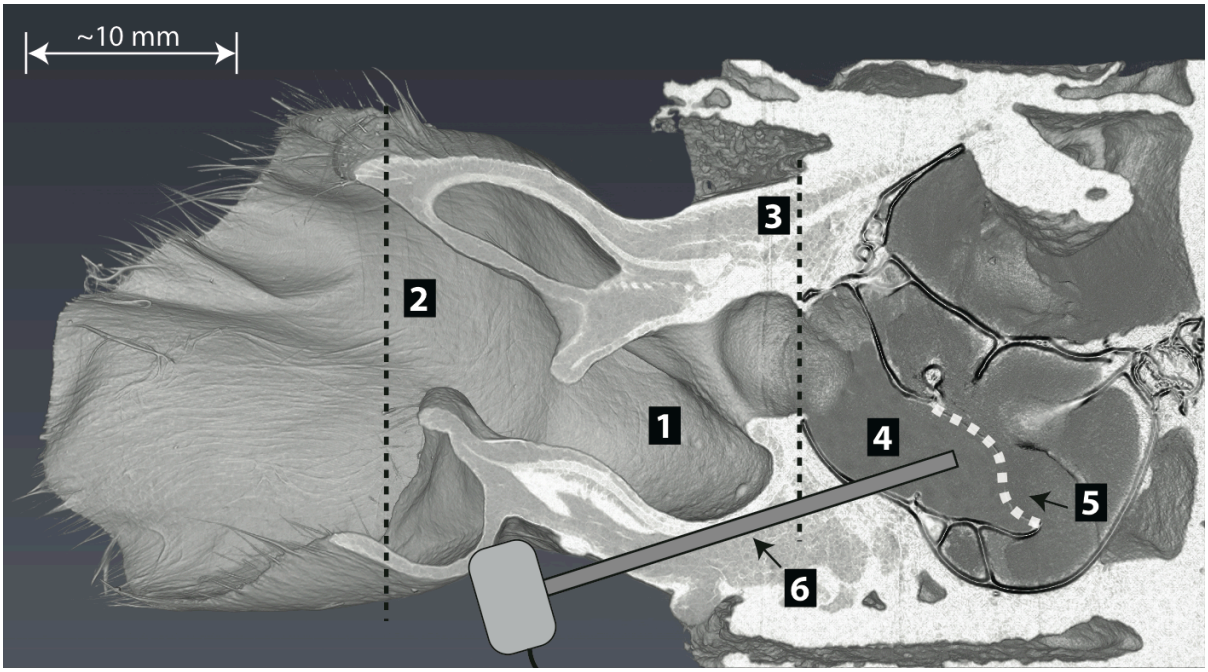

Figure B.1: Chinchilla auditory periphery – the posterior half of a volume rendered reconstruction of microCT scan data.
A single chinchilla ear (including external, middle, and inner ear) was scanned with 36 μm^3 voxel resolution. The effective cartilaginous ear canal (1) is bounded by two dashed lines: (2) the boundary between the pinna flange and the cartilaginous ear-canal tube, and (3) the entrance to the bony ear canal. The bony ear canal (4) is bounded by dashed line (3) and the tympanic membrane (white dashed line) (5). The location of the probe tube microphone (6) is schematized in the reconstruction.

B. External ear-canal model

The geometry of the chinchilla external ear canal (Figure B.2) was estimated from the complete 3D reconstruction. The ear canal was divided into segments and each segment was represented by a conical horn. The segments of the cartilaginous canal are of equal length and varied cross-sectional areas, and are arranged along a linear longitudinal axis. The bony canal segments are of varied length and cross-sectional area. The curved longitudinal axis of the bony canal was estimated by eye and the cross-sectional areas were arranged perpendicular to this axis. Distances between adjacent cross-sections were estimated by the distance between their intersections with the longitudinal axis.

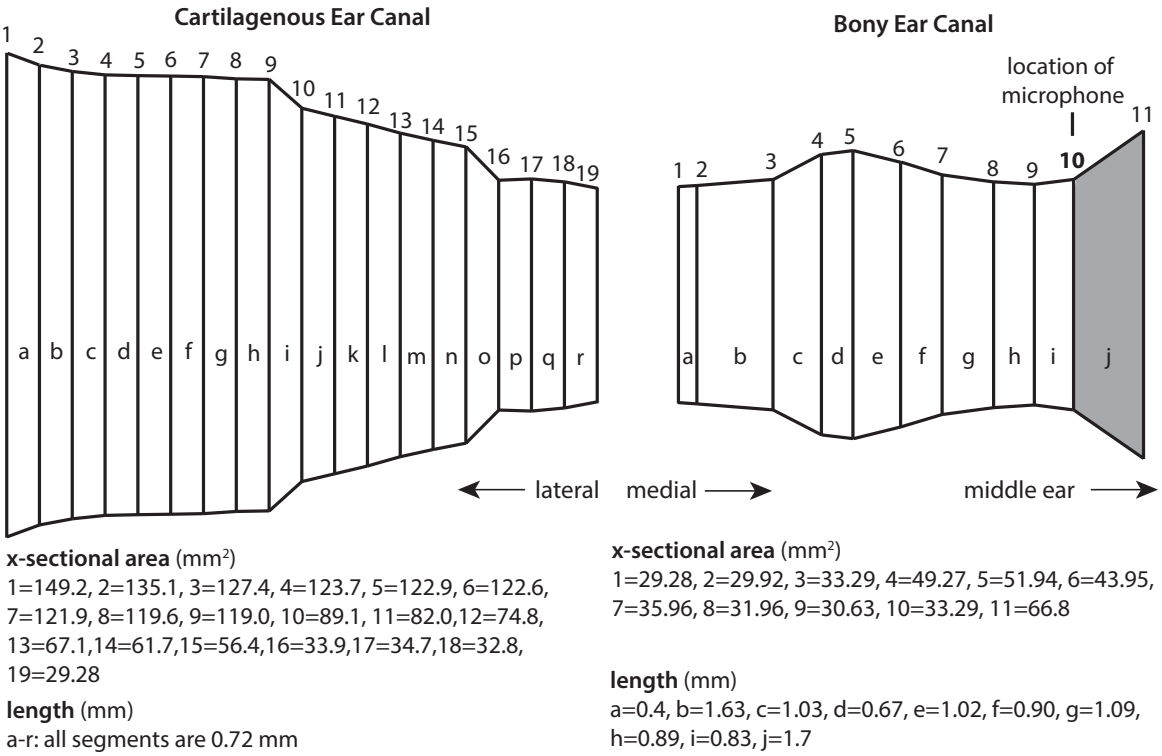

Figure B.2. External ear-canal model.
The cartilaginous portion of the ear canal is modeled by the concatenation of 18 horn segments of equal length and varied cross-sectional area. The bony portion of the ear canal is modeled by the concatenation of 10 horn segments of varied length and cross-section. In all segments, left is lateral and right is medial. The microphone that measured ECSP (ear-canal sound pressure) was located at the boundary between segment i and j of the bony canal.

The geometry of a conical horn (e.g. Figure B.3) is described by the following equations, where the subscript T corresponds to the narrow throat of the horn, and the subscript M corresponds to the wider mouth of the horn:

$$h_1 = (S_M - S_T/2) \tag{S1}$$

$$h_2 = S_M/2 \tag{S2}$$

$$\theta = \tan^{-1}(h_1/l) \tag{S3}$$

$$x_M = h_2/\tan\theta \tag{S4}$$

$$x_T = x_M - l \tag{S5}$$

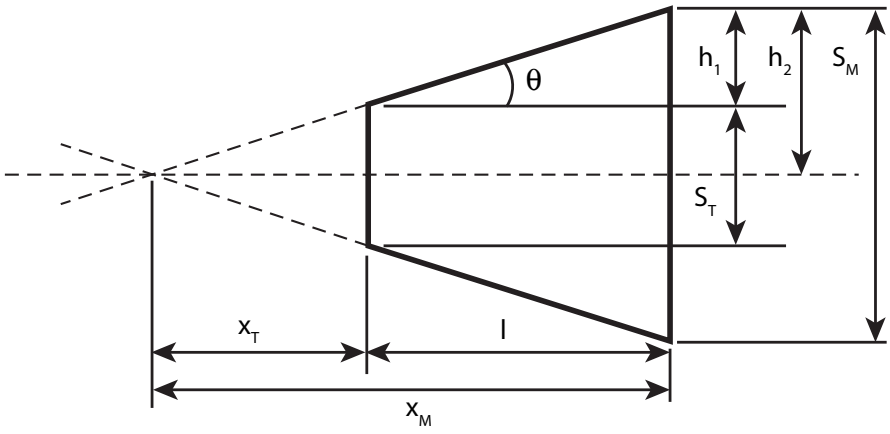

Figure B.3: Geometry of a finite conical horn (after Beranek and Mellow 2012).

C. Skull velocity and sound pressure responses to BC stimulation

The BC vibrators used in this had finite bandwidths that limited the bandwidth of our measurements (Figure B.4).

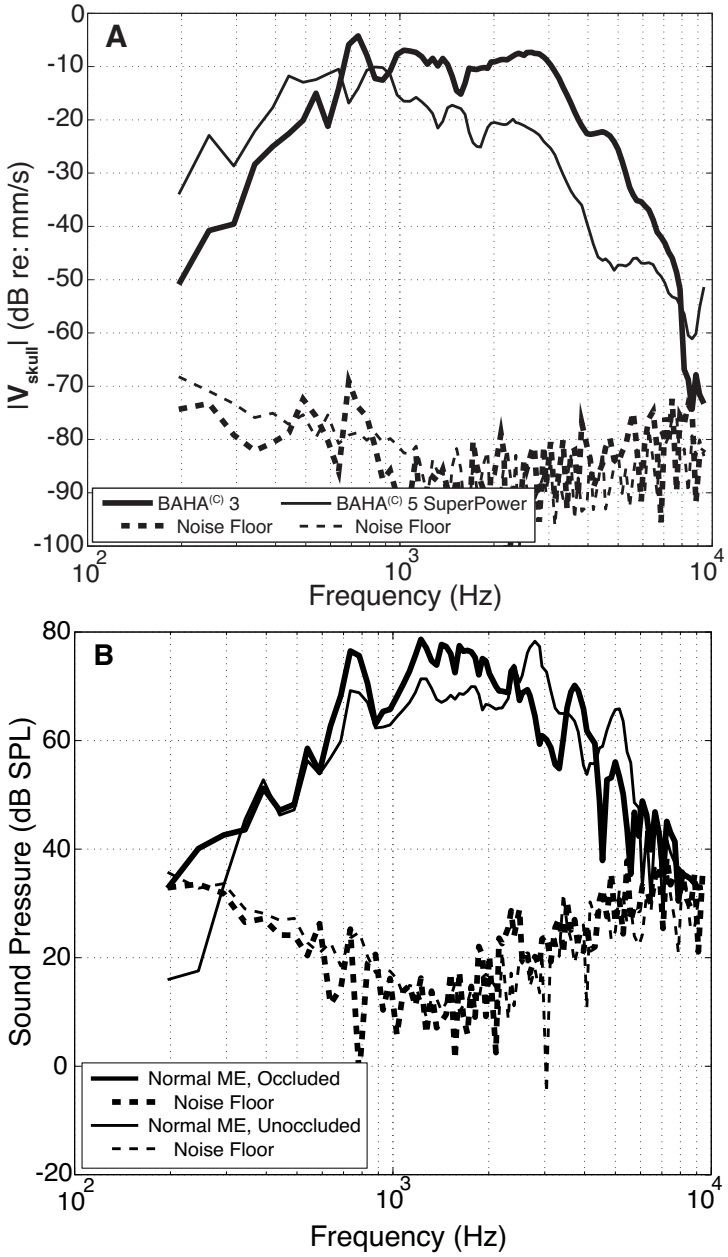

Figure B.4: BC-induced skull velocities and EC sound pressures.
(A) Examples of the skull velocity produced by the two BAHA stimulators used in this work (left-hand figure), and (B) the raw (un-normalized) ear-canal sound pressures elicited at the TM with the ear canal opened or occluded in one ear using the BAHA© 3. Both panels include estimates of the noise floor of the velocity and sound pressure measurements.`

D. Effect of BAHA-radiated sound on measured ECSP

Ear canal sound pressures were measured at the TM, and as a control at the entrance to the bony ear canal. The straight-line distance between the BAHA and these locations are approximately 2.5 cm and 3.5 cm, respectively. Figure B.5 illustrates sound pressure measurements made at these two locations with the BAHA attached to the chinchilla head divided by measurements made with the driven BAHA detached from the skull but placed along side the mounting post. Between 0.2 and 7 kHz, the sound pressures measured at the TM when the BAHA was attached to the skull were generally at least 20 dB larger than those measured without skull attachment.

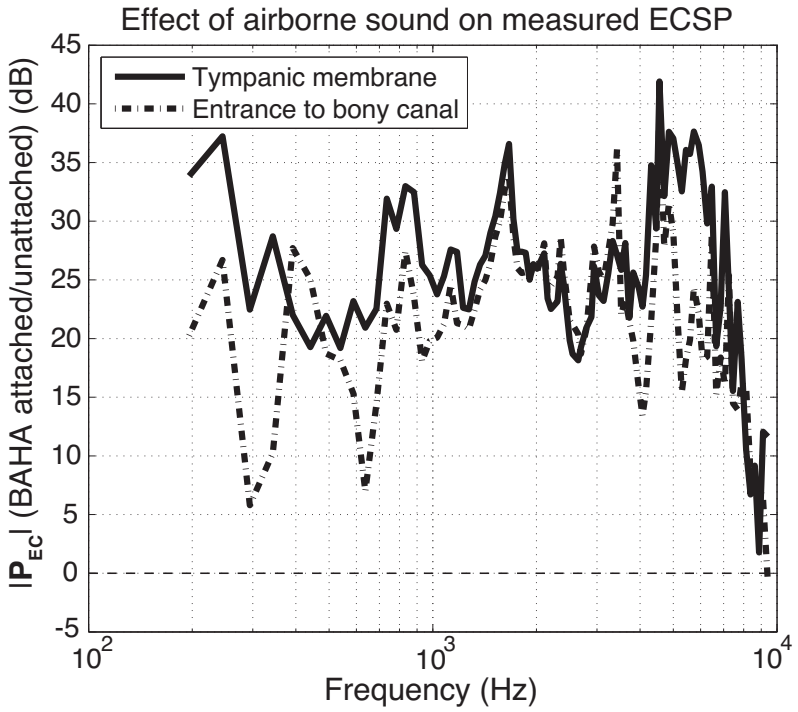

Figure B.5. Effect of airborne sound on measured ECSP.
We measured the contribution of airborne sound generated by the BAHA to the measured sound pressures when the ear canal was unoccluded and the middle-ear cavity was opened in a single chinchilla ear. Sound pressures measured at the TM and the entrance of the bony ear canal with

the BAHA mounted on the skull are divided by the sound pressures at the same locations when the BAHA is detached from the skull but placed next to the mounting post.

E. The occlusion Effect: comparison to human data (Stenfelt, 2003)

The effects of ear-canal occlusion on the sound pressures at the TM measured in the normal ear and the ear with the cartilaginous portion of the ear canal removed are shown in Figure B.6. Our data are compared to similar measurements by Stenfelt et al. made in humans (Stenfelt *et al.*, 2003).

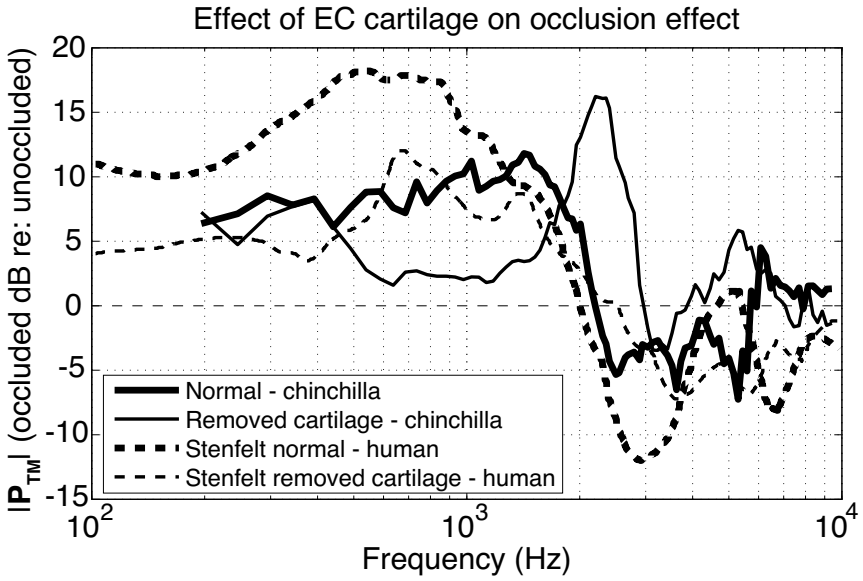

Figure B.6. Effect of ear canal occlusion on ECSP in chinchillas (this study) and humans (Stenfelt *et al.*, 2003).

Appendix C

A. Intracochlear sound pressures

Intracochlear sound pressures due to the compressional, inertia, and sound-pressure transmission sources were estimated in the fixed-stapes (*Stx*) and occluded round windows (*RWx*) cases. The sound pressures resulting from each source and their combined resulting pressures are shown in Figure B.1 along with the mean measured sound pressure, in the *Stx* condition. Sound pressures are shown in the *RWx* condition in Figure B.2.

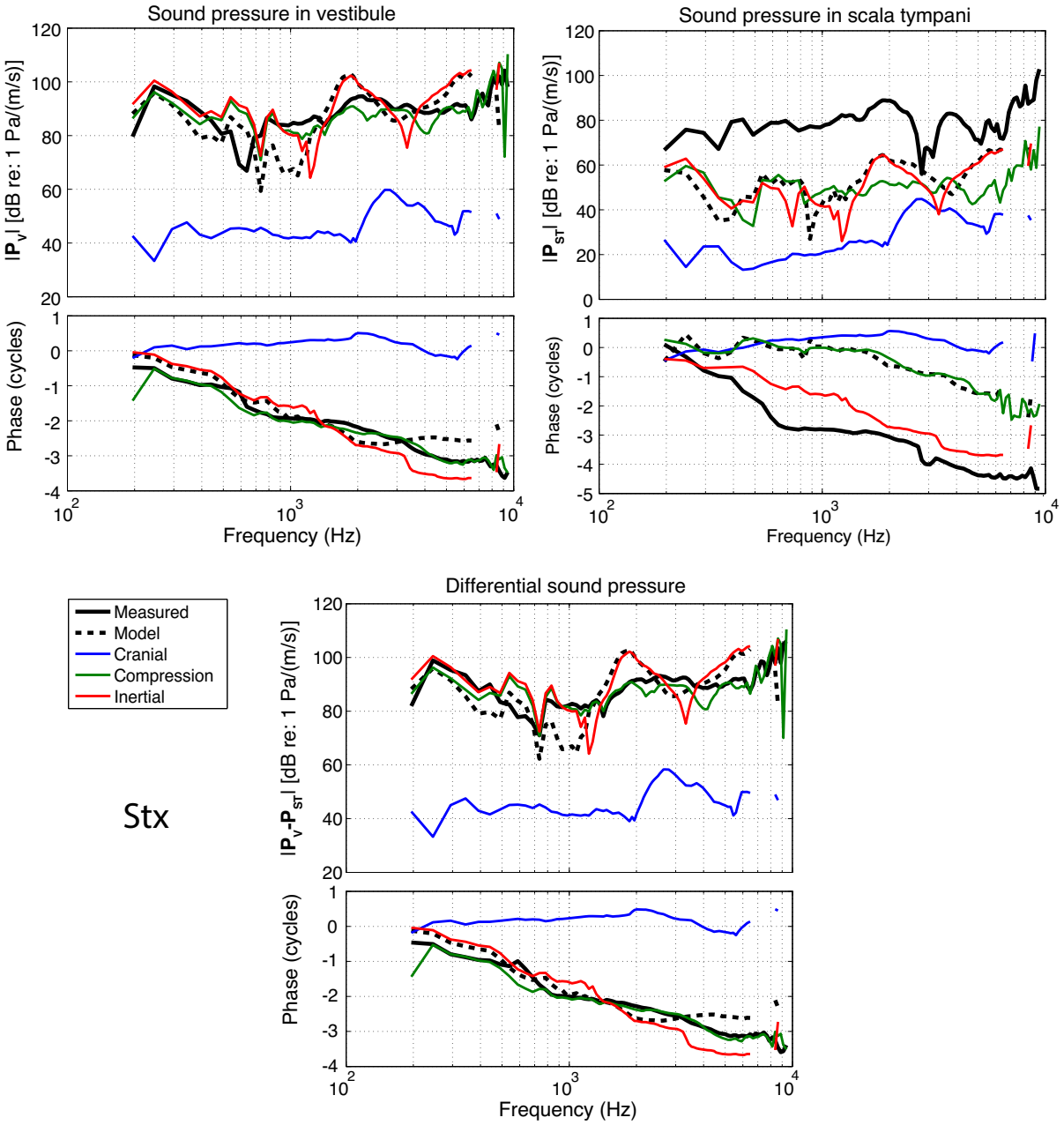

Figure C.1. Intracochlear sound pressures in *Stx* condition.
Intracochlear sound pressures were measured in the vestibule and scala tympani while the stapes was fixed (n = 8); estimated sound pressures due to each of the inner ear BC components, and their combined resulting pressures, are shown.

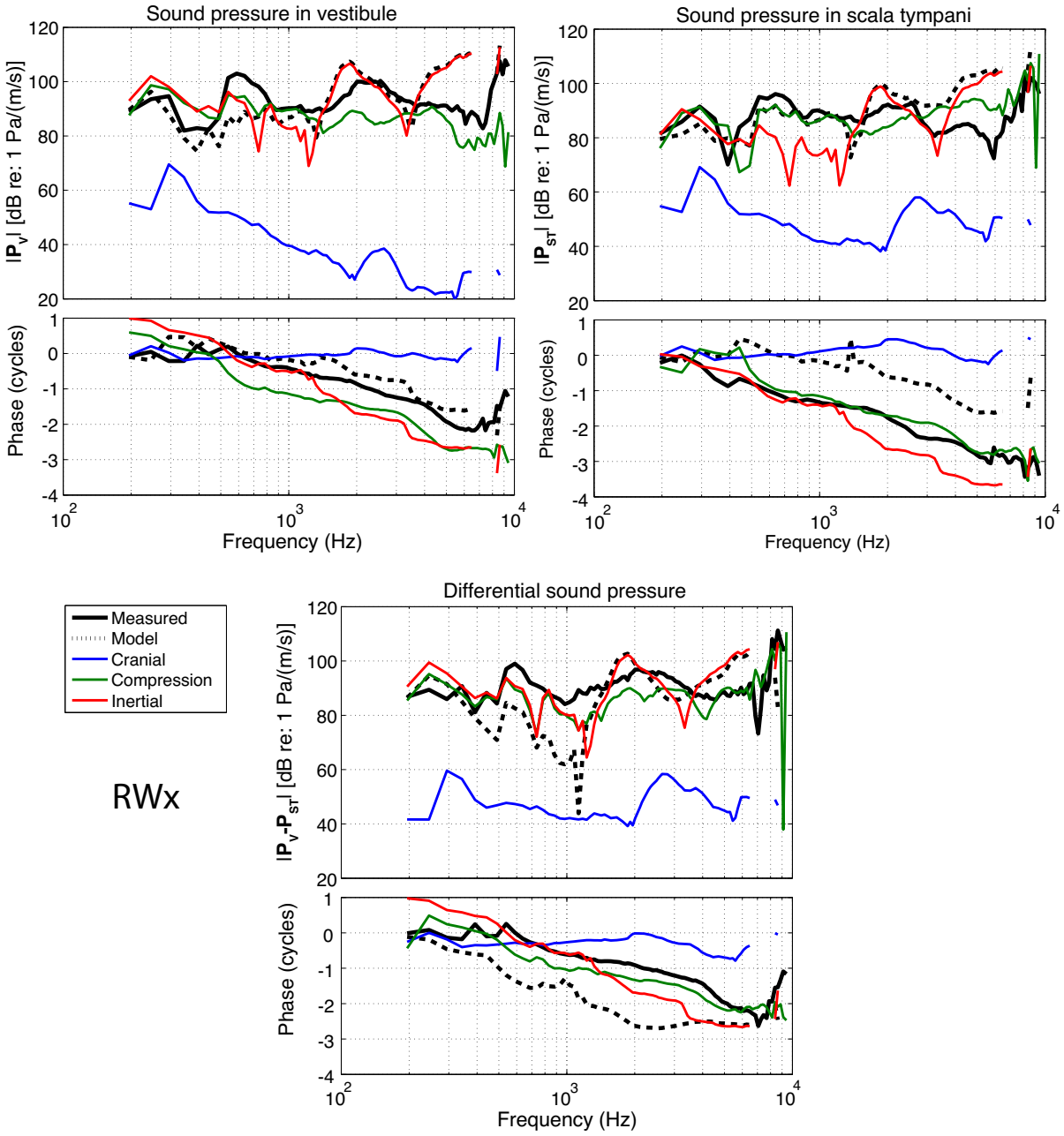

Figure C.2. Intracochlear sound pressures in *RWx* condition.
Intracochlear sound pressures were measured in the vestibule and scala tympani while the RW was occluded (n = 10); estimated sound pressures due to each of the inner ear BC components, and their combined resulting pressures, are shown.

C. Estimates of the inertial BC source under various constraints

Placement of a ground between impedances $\mathbf{Z_5}$ and $\mathbf{Z_6}$—necessary to estimate absolute pressures of $\mathbf{P_V}$ and $\mathbf{P_{ST}}$—result in an over-determined system. The inertial pressure source of Figure 4.7 is dependent on the volume velocity through circuit, which depends on two selected pressures constraining the system. Inertial source estimates are shown for the system constrained by 1) $\mathbf{P_V}$ and $\mathbf{P_{ST}}$, 2) $\mathbf{P_{ST}}$ and $\mathbf{P_{ground}}$, and 3) $\mathbf{P_V}$ and $\mathbf{P_{ground}}$. (Figure C.3)

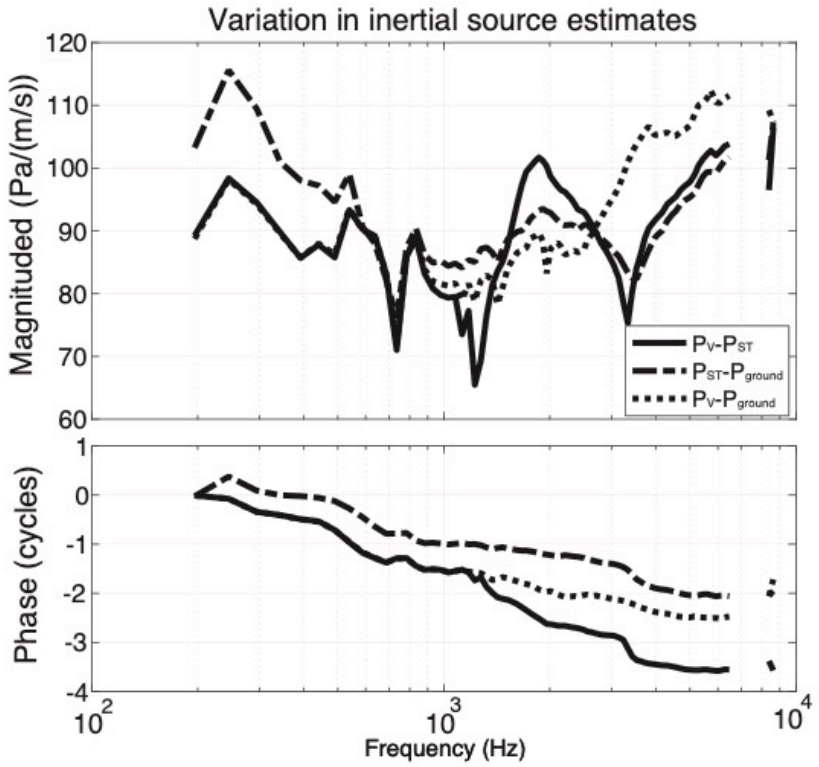

Figure C.3. Estimates of the inertial BC source under various system constraints.

References

Allen, G. W., and Fernandez, C. (**1960**). "The mechanism of bone conduction," Annals of Otology, Rhinology, and Laryngology **69**, 5-28.

Békésy, G. v. (**1932**). "Zur Theorie des Hörens bei der Schallaufnahme durch Knochenleitung," Ann Physík, 111-136.

Beranek, L. L. (**1993**). *Acoustics* (Acoustical Society of America, Cambridge).

Beranek, L. L., and Mellow, T. J. (**2012**). *Acoustics : sound fields and transducers*.

Berger, E. H., and Kerivan, J. E. (**1983**). "Influence of physiological noise and the occlusion effect on the measurement of real-ear attenuation at threshold," J Acoust Soc Am **74**, 81-94.

Bohnke, F., and Arnold, W. (**2006**). "Bone conduction in a three-dimensional model of the cochlea," ORL J Otorhinolaryngol Relat Spec **68**, 393-396.

Bowers, P., and Rosowski, J. J. (**2016**). "Optimization of Zwislocki's human middle-ear circuit model to fit modern data," Poster session presented at the Association for Research in Otolaryngology conference, San Diego, CA.

Bowers, P., and Rosowski, J. J. (**2019**). "A lumped-element model of the chinchilla middle ear," J Acoust Soc Am **145**, 1975-1992.

Brinkmann, W., Marres, E. H., and Tolk, J. (**1965**). "The Mechanism of Bone Conduction: An experimental study," Acta Otolaryngol **59**, 109-115.

Browning, G. C., and Granich, M. S. (**1978**). "Surgical anatomy of the temporal bone in the chinchilla," Ann Otol Rhinol Laryngol **87**, 875-882.

Chhan, D., Bowers, P., McKinnon, M. L., and Rosowski, J. J. (**2016a**). "Middle-ear and inner-ear contribution to bone bonduction in chinchilla: The development of Carhart's notch," Hear Res.

Chhan, D., Bowers, P., McKinnon, M. L., and Rosowski, J. J. (**2016b**). "Middle-ear and inner-ear contribution to bone conduction in chinchilla: The development of Carhart's notch," Hear Res **340**, 144-152.

Chhan, D., McKinnon, M. L., and Rosowski, J. J. (**2017**). "Identification of induced and naturally occurring conductive hearing loss in mice using bone conduction," Hear Res **346**, 45-54.

Chhan, D., Roosli, C., McKinnon, M. L., and Rosowski, J. J. (**2013**). "Evidence of inner ear contribution in bone conduction in chinchilla," Hear Res **301**, 66-71.

Dallos, P. (**1970**). "Low-frequency auditory characteristics: Species dependence," J Acoust Soc Am **48**, 489-499.

Dallos, P. (**1973**). *The Auditory Periphery Biophysics and Physiology* (Academic Press).

Dean, C. E. (**1930**). "Audition by bone conduction," J Acoust Soc Am **2**, 281-296.

Decraemer, W. F., Khanna, S. M., and Funnell, W. R. (**1994**). "A method for determining three-dimensional vibration in the ear," Hear Res **77**, 19-37.

Drescher, D. G., and Eldredge, D. H. (**1974**). "Species differences in cochlear fatigue related to acoustics of outer and middle ears of guinea pig and chinchilla," J Acoust Soc Am **56**, 929-934.

Edgerton, B. J., and Klodd, D. A. (**1976**). "Occlusion effect in bone conduction pure tone and speech audiometry," Journal of the American Audiology Society **2**, 151-158.

Eldredge, D. H., Miller, J. D., and Bohne, B. A. (**1981**). "A frequency-position map for the chinchilla cochlea," J Acoust Soc Am **69**, 1091-1095.

Fagelson, M., and Martin, F. N. (**1994**). "Sound pressure in the external auditory canal during bone-conduction testing," J Am Acad Audiol **5**, 379-383.

Frear, D., and Nakajima, H. (**2019**). "Hearing Loss at Massachusetts Eye and Ear Hospitals."

Frear, D. L., Guan, X., Stieger, C., Rosowski, J. J., and Nakajima, H. H. (**2018**). "Impedances of the inner and middle ear estimated from intracochlear sound pressures in normal human temporal bones," Hear Res **367**, 17-31.

Freeman, S., Sichel, J. Y., and Sohmer, H. (**2000**). "Bone conduction experiments in animals - evidence for a non-osseous mechanism," Hear Res **146**, 72-80.

Funnell, W. R., Khanna, S. M., and Decraemer, W. F. (**1992**). "On the degree of rigidity of the manubrium in a finite-element model of the cat eardrum," J Acoust Soc Am **91**, 2082-2090.

Gan, R. Z., Feng, B., and Sun, Q. (**2004**). "Three-dimensional finite element modeling of human ear for sound transmission," Ann Biomed Eng **32**, 847-859.

Guinan, J. J., Jr., and Peake, W. T. (**1967**). "Middle-ear characteristics of anesthetized cats," J Acoust Soc Am **41**, 1237-1261.

Hallpike, C. S. (**1929**). "Some Observations on Bone-conduction," Proc R Soc Med **22**, 1573-1576.

Hemila, S., Nummela, S., and Reuter, T. (**1995**). "What middle ear parameters tell about impedance matching and high frequency hearing," Hear Res **85**, 31-44.

Herzog, H. (**1926**). "Das Knochenleitungsproblem. Theoretische Erwägungen.," Z. Hals-, Nasen- u. Ohrenheilk **15**, 300-306.

Higashimachi, T., Shiratake, Y., Maeda, T., Sug, K., and Toriya, R. (**2013**). "Three-dimensional finite element analysis of the human middle ear and an application for clinics for tympanoplasty," WIT Transactions on Engineering Sciences **78**.

Homma, K., Shimizu, Y., Kim, N., Du, Y., and Puria, S. (**2010**). "Effects of ear-canal pressurization on middle-ear bone- and air-conduction responses," Hear Res **263**, 204-215.

Howell, P., and Williams, M. (**1989**). "Jaw movement and bone-conduction in normal listeners and a unilateral hemi-mandibulectomee," Scand Audiol **18**, 231-236.

Huber, A. M., Schwab, C., Linder, T., Stoeckli, S. J., Ferrazzini, M., Dillier, N., and Fisch, U. (**2001**). "Evaluation of eardrum laser doppler interferometry as a diagnostic tool," Laryngoscope **111**, 501-507.

Kanagawa, K., and Tokimoto, T. (**1982**). "Studies on CM and ABR by Bone Conduction in Guinea Pigs," Pract Otorhinolaryngol (Basel) **75**, 464-475.

Keefe, D. H. (**2015**). "Human middle-ear model with compound eardrum and airway branching in mastoid air cells," J Acoust Soc Am **137**, 2698-2725.

Killion, M. C. (**1988**). "The "hollow voice" occlusion effect," (Etymotic Research, Elk Grove).

Kim, N., Homma, K., and Puria, S. (**2011**). "Inertial bone conduction: symmetric and anti-symmetric components," J Assoc Res Otolaryngol **12**, 261-279.

Kim, N., Steele, C. R., and Puria, S. (**2014**). "The importance of the hook region of the cochlea for bone-conduction hearing," Biophys J **107**, 233-241.

Kirikae, I. (**1959**). "An experimental study on the fundamental mechanism of bone conduction," Acta Otolaryngol Suppl **145**, 1-111.

Koike, T., Wada, H., and Kobayashi, T. (**2002**). "Modeling of the human middle ear using the finite-element method," J Acoust Soc Am **111**, 1306-1317.

Kringlebotn, M. (**1988**). "Network model for the human middle ear," Scand Audiol **17**, 75-85.

Legouix, J. P. (**1959**). "[Experimental study of the mechanism of bone conduction in cases of transmission deafness]," Ann Otolaryngol **76**, 930-936.

Lemons, C., and Meaud, J. (**2016**). "Middle-ear function in the chinchilla: Circuit models and comparison with other mammalian species," J Acoust Soc Am **140**, 2735.

Littler, T. S., Knight, J. J., and Strange, P. H. (**1952**). "Hearing by bone conduction and the use of bone-conduction hearing aids," in *Royal Society of Medicine* (Manchester Royal Infirmary).

Lowy, K. (**1942**). "Cancellation of the Electrical Cochlear Response with Air- and Bone-Conducted
Sound," J. Acoust. Soc. Am. **13**, 156-158.

Lynch, T. J., 3rd, Nedzelnitsky, V., and Peake, W. T. (**1982**). "Input impedance of the cochlea in cat," J Acoust Soc Am **72**, 108-130.

Lynch, T. J., 3rd, Peake, W. T., and Rosowski, J. J. (**1994**). "Measurements of the acoustic input impedance of cat ears: 10 Hz to 20 kHz," J Acoust Soc Am **96**, 2184-2209.

Mach, E. (**1863**). "Zur Theorie des Gehörorgans," Sitzungsberichte der Acadamie der Wissenschaften **48**, 283-300.

Maison, S. F., Vetter, D. E., and Liberman, M. C. (**2007**). "A novel effect of cochlear efferents: in vivo response enhancement does not require alpha9 cholinergic receptors," J Neurophysiol **97**, 3269-3278.

Marres, E. H. (**1965**). "The mechanism of bone conduction," Pract Otorhinolaryngol (Basel) **27**, 304-305.

Molvaer, O. I., Vallersnes, F. M., and Kringlebotn, M. (**1978**). "The size of the middle ear and the mastoid air cell," Acta Otolaryngol **85**, 24-32.

Motallebzadeh, H., Maftoon, N., Pitaro, J., Funnell, W. R., and Daniel, S. J. (**2017a**). "Finite-Element Modelling of the Acoustic Input Admittance of the Newborn Ear Canal and Middle Ear," J Assoc Res Otolaryngol **18**, 25-48.

Motallebzadeh, H., Maftoon, N., Pitaro, J., Funnell, W. R. J., and Daniel, S. J. (**2017b**). "Fluid-Structure Finite-Element Modelling and Clinical Measurement of the Wideband Acoustic Input Admittance of the Newborn Ear Canal and Middle Ear," J Assoc Res Otolaryngol **18**, 671-686.

Nakajima, H. H., Dong, W., Olson, E. S., Merchant, S. N., Ravicz, M. E., and Rosowski, J. J. (**2009**). "Differential intracochlear sound pressure measurements in normal human temporal bones," J Assoc Res Otolaryngol **10**, 23-36.

Nakajima, H. H., Ravicz, M. E., Merchant, S. N., Peake, W. T., and Rosowski, J. J. (**2005**). "Experimental ossicular fixations and the middle ear's response to sound: evidence for a flexible ossicular chain," Hear Res **204**, 60-77.

Nedzelnitsky, V. (**1980**). "Sound pressures in the basal turn of the cat cochlea," J Acoust Soc Am **68**, 1676-1689.

Nelder, J. A., and Mead, R. (**1965**). "A simplex method for function minimization," The Computer Journal **8**, 308-313.

O'Connor, K. N., and Puria, S. (**2008**). "Middle-ear circuit model parameters based on a population of human ears," J Acoust Soc Am **123**, 197-211.

Olson, E. S. (**1999**). "Direct measurement of intra-cochlear pressure waves," Nature **402**, 526-529.

Olson, E. S. (**2001**). "Intracochlear pressure measurements related to cochlear tuning," J Acoust Soc Am **110**, 349-367.

Pohlmann, A. G. (**1930**). "Correlations between the acuity for hearing and bone-transmitted sounds in Rinne-negative and Rinne-positive cases.," Annals of Otology, Rhinology, and Laryngology **39**, 927-960.

Puria, S., and Allen, J. B. (**1991**). "A parametric study of cochlear input impedance," J Acoust Soc Am **89**, 287-309.

Puria, S., and Allen, J. B. (**1998**). "Measurements and model of the cat middle ear: evidence of tympanic membrane acoustic delay," J Acoust Soc Am **104**, 3463-3481.

Puria, S., and Steele, C. (**2010**). "Tympanic-membrane and malleus-incus-complex co-adaptations for high-frequency hearing in mammals," Hear Res **263**, 183-190.

Ranke, O. (**1953**). *Physiologie des Gehörs Mit 132 Abb.* (Springer, Göttingen Heidelberg).

Ravicz, M. E., and Rosowski, J. J. (**2012**). "Chinchilla middle-ear admittance and sound power: high-frequency estimates and effects of inner-ear modifications," J Acoust Soc Am **132**, 2437-2454.

Ravicz, M. E., and Rosowski, J. J. (**2013a**). "Inner-ear sound pressures near the base of the cochlea in chinchilla: further investigation," J Acoust Soc Am **133**, 2208-2223.

Ravicz, M. E., and Rosowski, J. J. (**2013b**). "Middle-ear velocity transfer function, cochlear input immittance, and middle-ear efficiency in chinchilla," J Acoust Soc Am **134**, 2852-2865.

Ravicz, M. E., Rosowski, J. J., and Voigt, H. F. (**1992**). "Sound-power collection by the auditory periphery of the Mongolian gerbil Meriones unguiculatus. I: Middle-ear input impedance," J Acoust Soc Am **92**, 157-177.

Retjö, A. (**1914**). "Beiträge zur Physiologie der Knochenleitung.," Verh. dtsch. Otol. Ges. **23**, 268-285.

Rosowski, J. J. (**1994**). "Outer and middle ear," in *Springer handbook of auditory research: comparative heraing: mammals*, edited by F. R. Popper AN (Spring-Verlag, New York), pp. 172-247.

Rosowski, J. J., Bowers, P., and Nakajima, H. H. (**2018**). "Limits on normal cochlear 'third' windows provided by previous investigations of additional sound paths into and out of the cat inner ear," Hear Res **360**, 3-13.

Rosowski, J. J., Carney, L. H., and Peake, W. T. (**1988**). "The radiation impedance of the external ear of cat: measurements and applications," J Acoust Soc Am **84**, 1695-1708.

Rosowski, J. J., Mehta, R. P., and Merchant, S. N. (**2003**). "Diagnostic utility of laser-Doppler vibrometry in conductive hearing loss with normal tympanic membrane," Otol Neurotol **24**, 165-175.

Rosowski, J. J., and Merchant, S. N. (**1995**). "Mechanical and acoustic analysis of middle ear reconstruction," Am J Otol **16**, 486-497.

Rosowski, J. J., Ravicz, M. E., and Songer, J. E. (**2006**). "Structures that contribute to middle-ear admittance in chinchilla," J Comp Physiol A Neuroethol Sens Neural Behav Physiol **192**, 1287-1311.

Ruggero, M. A., Rich, N. C., Robles, L., and Shivapuja, B. G. (**1990**). "Middle-ear response in the chinchilla and its relationship to mechanics at the base of the cochlea," J Acoust Soc Am **87**, 1612-1629.

Schick, F. (**1991**). "An eletrical model for simulation of bone and air conducted hearing," Acustica **74**, 134-142.

Schroeter, J., and Poesselt, C. (**1986**). "The use of acoustical test fixtures for the measurement of hearing protector attenuation. Part II: Modeling the external ear, simulating bone conduction, and comparing test fixture and real-ear data," J Acoust Soc Am **80**, 505-527.

Sim, J. H., Chatzimichalis, M., Lauxmann, M., Roosli, C., Eiber, A., and Huber, A. M. (**2010**). "Complex stapes motions in human ears," J Assoc Res Otolaryngol **11**, 329-341.

Sim, J. H., Puria, S., and Steele, C. (**2007**). "Calculation of inertial properties of the malleus-incus complex from micro-CT imaging," Mechanics of Materials and Structures **2**.

Songer, J. E., Brinsko, K. M., and Rosowski, J. J. (**2003**). "Superior Semicircular Canal Dehiscence and Bone Conduction in Chinchilla," in *Middle Ear Mechanics in Research and Otology* (Matsuyama, Ehime, Japan).

Songer, J. E., and Rosowski, J. J. (**2006**). "The effect of superior-canal opening on middle-ear input admittance and air-conducted stapes velocity in chinchilla," J Acoust Soc Am **120**, 258-269.

Songer, J. E., and Rosowski, J. J. (**2007a**). "A mechano-acoustic model of the effect of superior canal dehiscence on hearing in chinchilla," J Acoust Soc Am **122**, 943-951.

Songer, J. E., and Rosowski, J. J. (**2007b**). "Transmission matrix analysis of the chinchilla middle ear," J Acoust Soc Am **122**, 932-942.

Stenfelt, S. (**2007**). "Simultaneous cancellation of air and bone conduction tones at two frequencies: extension of the famous experiment by von Bekesy," Hear Res **225**, 105-116.

Stenfelt, S. (**2015**). "Inner ear contribution to bone conduction hearing in the human," Hear Res **329**, 41-51.

Stenfelt, S. (**2016**). "Model predictions for bone conduction perception in the human," Hear Res **340**, 135-143.

Stenfelt, S., and Goode, R. L. (**2005**). "Bone-conducted sound: physiological and clinical aspects," Otol Neurotol **26**, 1245-1261.

Stenfelt, S., and Reinfeldt, S. (**2007**). "A model of the occlusion effect with bone-conducted stimulation," Int J Audiol **46**, 595-608.

Stenfelt, S., Wild, T., Hato, N., and Goode, R. L. (**2003**). "Factors contributing to bone conduction: the outer ear," J Acoust Soc Am **113**, 902-913.

Sultan, F., and Braitenberg, V. (**1993**). "Shapes and sizes of different mammalian cerebella. A study in quantitative comparative neuroanatomy," J Hirnforsch **34**, 79-92.

Teas, D. C., and Nielsen, D. W. (**1975**). "Interaural attenuation versus frequency for guinea pig and chinchilla CM response," J Acoust Soc Am **58**, 1066-1072.

Tonndorf, J. (**1966**). "Bone conduction. Studies in experimental animals," Acta Otolaryngol, Suppl 213:211+.

Tonndorf, J. (**1972**). "Bone Conduction," in *Foundations of Modern Auditory Theory*, edited by J. V. Tobias (Academic Press, New York), pp. 197-237.

Tonndorf, J. (**1976**). "Bone Conduction," in *Auditory System. Handbook of Sensory Physiology* (Springer, Berlin), pp. 37-84.

Tonndorf, J., Campbell, R. A., Berstein, L., and Reneau, J. P. (**1961**). "Quantitative Evaluation of Inertial and Compressional Components of Bone Conduction in Cats," J Acoust Soc Am **33**, 1671.

von Bismarck, G. (**1967**). "The sound pressure transformation function from free field to the eardrum of chinchilla," (Massachusetts Institute of Technology, Cambridge, MA).

Voss, S. E., Rosowski, J. J., Merchant, S. N., and Peake, W. T. (**2001**). "Middle-ear function with tympanic-membrane perforations. II. A simple model," J Acoust Soc Am **110**, 1445-1452.

Vrettakos, P. A., Dear, S. P., and Saunders, J. C. (**1988**). "Middle ear structure in the chinchilla: a quantitative study," Am J Otolaryngol **9**, 58-67.

Wang, X., and Gan, R. Z. (**2016**). "3D finite element model of the chinchilla ear for characterizing middle ear functions," Biomech Model Mechanobiol **15**, 1263-1277.

Zwislocki, J. (**1962**). "Analysis of the middle-ear function. Part I: Input impedance," J Acoust Soc Am **34**, 1514-1523.